High fidelity simulations of Taylor bubbles in turbulent co-current flow

Traianos Karageorgiou

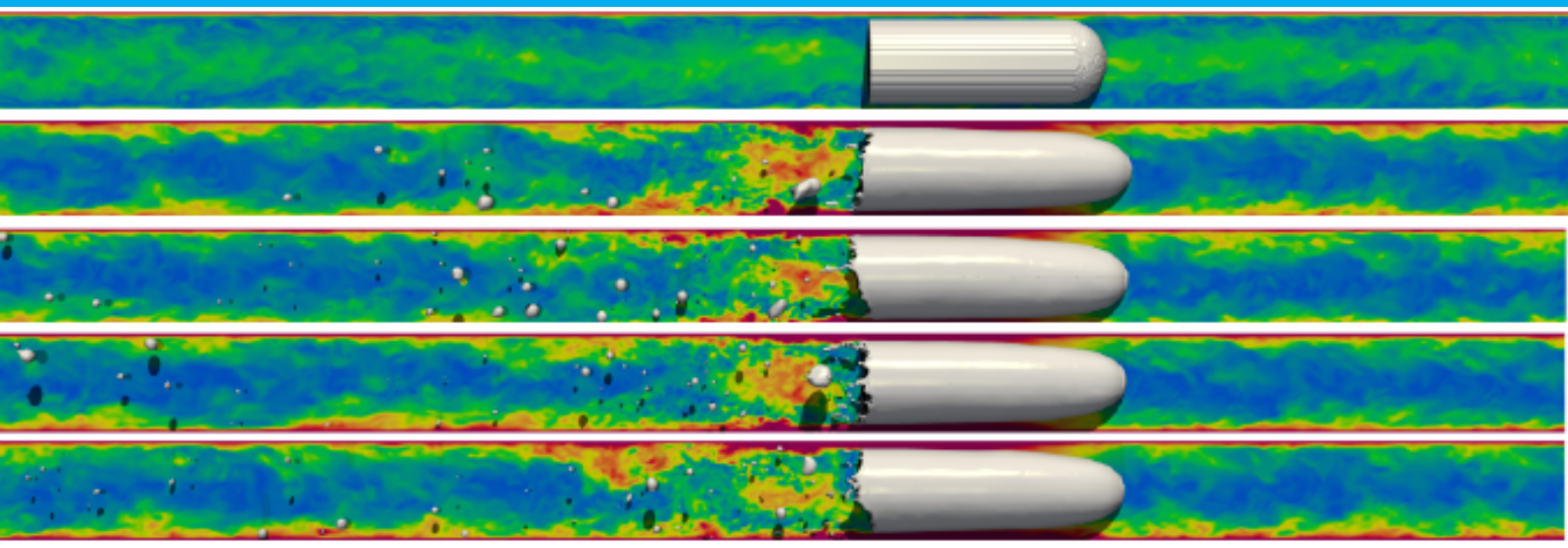

TU Delft

High fidelity simulations of Taylor bubbles in turbulent co-current flow

by

Traianos Karageorgiou

in partial fulfillment of the requirements for the degree of

Master of Science
in Applied Mathematics (COSSE)

at the Delft University of Technology,
to be defended publicly on Tuesday 11 August 2020 at 10.00.

Student number:	5157005	
Thesis committee:	Prof. dr. ir. K. Vuik,	TU Delft, supervisor
	As. Prof. dr. ir. D. Toshniwal,	TU Delft, supervisor
	Prof. dr. ir. A.W. Heemink	TU Delft

TU Delft

Abstract

The modeling and simulation of Taylor bubble flow using CFD can contribute significantly to the topic of nuclear reactor safety and in particular, in the emergency cooling of nuclear reactors during a loss of coolant accident, or in the U-tubes of a stream generator during a pipe rupture. To achieve an accurate representation of the gas-liquid interface for high values of Reynolds number, a general interfacial turbulence model should be developed which adapts to local conditions automatically. Direct Numerical Simulation (DNS) of relevant large interface two-phase turbulence has the potential to contribute to this, as it can produce more refined insight while being complementary to experimental data. The current graduation project illustrates a simulation approach towards DNS of turbulent co/counter-current Taylor bubble flow. It comprises a continuation of the novel simulation strategy indicated in [1, OpenFOAM] in which LES of co-current turbulent Taylor bubble flow was indicated and the authors concluded that LES mesh resolution is not sufficient to capture accurately the gas-liquid interface, velocity fluctuations, and bubble disintegration rate. To counter this, in the current work, a Basilisk code is developed which due to its adaptive local grid refinement and its accurate solution of advection equation, comprises a better choice than OpenFOAM for DNS in two-phase flows (via the settings of [2] for laminar bubble flow and [3] for turbulent co-current flow) since it captures sharper the interface and reduces the computational cost significantly. Except for OpenFOAM, Basilisk is also successfully validated against [4, ANSYS] for the laminar Taylor bubble flow. Last but not least, the work is further extended to the simulation of laminar and turbulent counter-current Taylor bubble flows in which the effect of the choice of the pipe diameter and the initial bubble length on the bubble's decay rate is analyzed for the experimental setting of [5]. Overall, despite the lack of fully DNS quality, this study extends the work of [1] and provides further insight into the performance of Basilisk in two-phase flows at a reasonable computational cost. The results and conclusions from the current study may contribute to the development of low-order turbulence models and the validation of more general two-phase modeling strategies.

Preface

This master thesis has been written as the graduation project for the Computer Simulations for Science and Engineering (COSSE) dual master program which allowed me to acquire both a Master of Science in Scientific Computing from TU Berlin and in Applied Mathematics from TU Delft.

The work was initially started 9 months ago with the literature study on Taylor bubble flow and was continued as part of an internship at the Computational Fluid Dynamics department of Nuclear Research and Consultancy Group (NRG). During these months, Basilisk software was used for implementing high-fidelity simulations of Taylor bubbles in turbulent co/counter-current flow. The developed Basilisk code was firstly validated for several test cases (laminar bubble flow, laminar Taylor bubble flow, turbulent co-current Taylor bubble flow) before carrying out simulations in laminar and turbulent counter-current Taylor bubble flow in which the influence of pipe diameter and bubble's length on bubble's decay rate was analyzed.

All this period, I had the continuous support of my supervisors at TU Delft, professor Kees Vuik and assistant professor Deepesh Toshniwal. I want to thank them both for supporting and guiding me throughout the project. Their excellent advice was worthy of the world-wide reputation of TU Delft.

The current work would have not been possible without the help of my supervisor/mentor at NRG E.M.A. Frederix. I would like to express my sincere gratitude to him because he inspired me and directed me all these months. It has been a great honor for me to have been worked alongside him. Moreover, I would like to thank my manager at NRG, Ed Komen who gave me the opportunity to work in such a challenging project and becoming a member of NRG's CFD department for six months.

Last but not least, I would also like to thank the coordinators of the program, in particular, professors Reinhard Nabben (TU Berlin), Kees Vuik (TU Delft) and Michael Hanke (KTH) for orientation and guidance throughout the program.

Traianos Karageorgiou
Delft, August 2020

Contents

1 Introduction

1.1. Introduction to Computational Fluid Dynamics

Since the 19$^{\text{th}}$-century significant efforts have been made in the field of fluid dynamics to understand the physical behavior, motion, and properties of fluids to translate them into mathematical expressions and governing laws.

The basic governing equations representing the flow of a viscous fluid are the Navier-Stokes equations which were derived from the application of Newton's second law of motion to fluid motion and are also called momentum equations. The Navier-stokes equations are extensions of the Euler Equations and include the effects of viscosity [6]. In the case of Newtonian fluid, the conservation form of Navier-Stokes momentum equations describe a balance between inertia, pressure, viscosity and external forces and is given in differential form by

$$\frac{\partial (\rho \mathbf{u})}{\partial t} + \nabla \cdot (\rho \mathbf{u} \otimes \mathbf{u}) = -\nabla p + \mu \nabla^2 \mathbf{u} + \frac{1}{3}\mu \nabla (\nabla \cdot \mathbf{u}) + \rho \mathbf{g}, \tag{1.1}$$

where ρ is the fluid density, u the velocity field of the fluid, t the time, p the pressure, μ the dynamic viscosity and g the gravitational acceleration when gravity is the external force [6]. In particular:

- $\frac{\partial(\rho \mathbf{u})}{\partial t} + \nabla \cdot (\rho \mathbf{u} \otimes \mathbf{u})$ indicates the momentum convection,
- $-\nabla p$ demonstrates the pressure,
- $\mu \nabla^2 \mathbf{u} + \frac{1}{3}\mu \nabla (\nabla \cdot \mathbf{u})$ displays the viscous forces,
- and the last term $\rho \mathbf{g}$ the external(i.e. gravitational) forces.

If we rewrite the Navier-stokes into dimensionless form, a very important dimensionless quantity will come from the viscous and convection terms, known as Reynolds number. The Reynolds number comprises the most important dimensionless number in fluid dynamics because it characterizes the flow and is defined as the ratio of inertial over viscous forces according to the formula

$$Re = \frac{\rho U L}{\mu} = \frac{U L}{\nu}, \tag{1.2}$$

where ν is the kinematic viscosity, L is the characteristic length, and U the upstream velocity. If $Re >> 1$, then inertia forces dominate while in case of $Re << 1$ friction forces (i.e. viscosity) dominate [7].

The Navier-Stokes equations are always solved together with the continuity equation which is known as conservation of mass as well as a particular set of boundary conditions. Together they form a boundary value problem [6]. The conservation of mass is described by the continuity equation and is given in differential form by

$$\frac{\partial \rho}{\partial t} + \nabla \cdot (\rho \mathbf{u}) = 0. \tag{1.3}$$

Navier-Stokes equations are usually too complex to be solved analytically, except for a few simple cases [6]. Therefore, a numerical approach is needed to be able to solve them. During a numerical approach, the first step is the spatial discretization of a domain, known as mesh generation. Depending on the problem, the Navier-Stokes equations can be solved either iteratively or directly.

The choice of spatial discretization method is very important for achieving accurate calculations. The typical discretization methods are finite difference, finite element, and finite volume methods. The common idea in all methods is to divide the geometrical domain into very small finite parts (i.e. mesh generation). There are three types of grids: structured grids, unstructured grids, and block-structured grids [7],[8].

The Navier-stokes equations are unsteady in their general form and they need to be discretized also in time. In general, the temporal discretization is done through integration over time on the discretized equation. Temporal discretization methods varies in numerical analysis from fully implicit to fully explicit methods depending on the number of the weighted average between current and future values. Implicit methods are computationally more expensive and sometimes they can be much harder to be implemented than explicit methods. However, implicit methods may achieve fast convergence rates and they are preferred when stability plays an important role e.g. at stiff problems [9], [7], [8].

Runge-Kutta methods are a family of both implicit and explicit iterative methods that are widely used in numerical analysis for the solution of Navier-Stokes equations. The solvers of Navier-stokes equations can be also divided to coupled solvers where velocity and pressure are solved simultaneously (e.g. backwards differencing schemes, Crank-Nicolson scheme) or segregated/splitting methods where the velocity and pressure are solved sequentially (e.g. SIMPLE, PISO).The selection of the appropriate temporal discretization methods depend on the computational cost and the required stability [8], [7].

High-speed computers have been used for the implementation of numerical solution to Navier-stokes equations. The accuracy is determined by the choice of the spatial and time discretization scheme, the stopping criterion selected by the user, or simply by the floating-point precision of the system used. The simulation results of a problem are compared with the results derived from experiments and possible errors are determined. This is an iterative process until the maximum accuracy is achieved. The whole process is illustrated in figure 1.1.

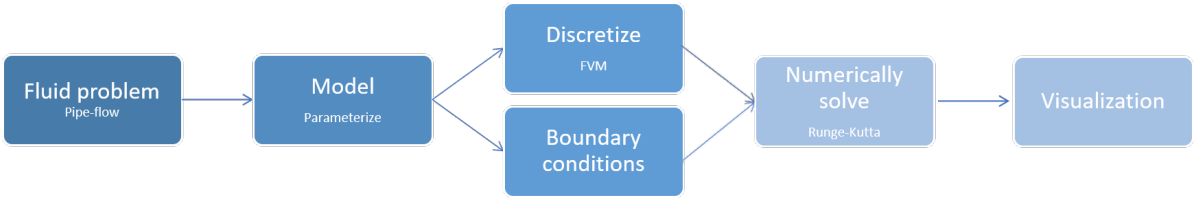

Figure 1.1: Flow chart of the CFD process in a fluid problem

This process is defined as Computational Fluid Dynamics, or CFD for short. This makes CFD a crossing point of three disciplines: Fluid dynamics, Mathematics, and Computer science, as it numerically solves complex partial differential equations to describe the behavior of fluids [10].

There are many high-performance CFD software packages. Their main division is between commercial and open-source software packages. Open-source means that the user is free to view and modify the underlying code of the software. Both open-source and commercial CFD software packages are used in a wide range of research and industrial areas. CFD is a great research, educational and industrial tool which covers the fields of aerospace, automotive engineering, chemical and mineral processing, biomedical science, civil and environmental engineering as well as power generation [10].

1.2. Multiphase Flows

A fluid flow can be characterized as:

- laminar or turbulent flow depending on the value of Reynolds number, and
- single-phase fluid flow or Multi-phase fluid flow depending on the number of phases that simultaneously exist.

Classic study of fluid dynamics is focused on the flow of a single homogeneous phase such as water, air or steam [11]. In cases and locations where the fluid flow consists of more than one state or component,

the relatively simple relationships used for analyzing single-phase flow are insufficient and the problem must be solved as multiphase flow [12].

Multiphase flow is defined as the simultaneous flow of materials with two or more different thermodynamic states or phases (e.g. steam-water flows)[11]. Multiphase flow takes also place when there are two or more materials with different physical properties but in the same phase or state (e.g. oil-water flows) [13]. Therefore, in the second definition the word "multi" is referred to the different components and not to the amount of "phases" even though this kind of flows is also called multiphase. Every phase of each material depicts a volume fraction of solid, liquid or gaseous matter with its properties such as velocity and temperature [11]. In cases where the temperature of one phase is different from the temperature of the other(s) state(s), then there is also multiphase heat transfer through their interfaces. Moreover, if the heat transfer takes place between different phases of the same material, then the heat transfer is also followed by mass transfer (solid-liquid, solid-vapor or liquid-vapor phase change) [14].

The analysis and solution of multi-phase fluid flow is usually very complex compared with conditions of single phase flow. The modeling of two-phase flow is still under development because there are many types of instabilities in multiphase flow.

The three main steps for the modelling of a multiphase flow problem consists the identification of the type of the multiphase flow, the specification of the physical process together with the phenomena may occur, and at the end the determination of the mathematical model [15].

First of all, it is essential to identify the characteristics of the flow and the important effects which will influence the choice of the appropriate model. This analysis requires the determination of the characteristics of the flow,the hydrodynamic effects as well as the transport phenomena. The characteristics of the flow consists the knowledge of the flow regime (e.g. bubbly flow,slug flow etc.), the grade of turbulence at the flow, the density and the viscosity of each phase, surface tension etc .Depending on the type of the flow, the hydrodynamic effects may include the change in interface,a particle-wall or particle-particle collision,a possible coalescence, turbulent flow etc. On the other hand, the transport phenomena may include heat transfer, mass transfer, change in composition or/ and heterogeneous reactions. Therefore the natural process specification may include the phenomena of separation, filtration, suspension, evaporation or reaction [16].

The specification of the flow regime between two or more immiscible fluids can be classified into types according to its behaviour. Three main types of the multiphase flow can be found in the literature [12], [14], [16]:

- Flow with separated phases: Different immiscible fluids in continuous phases which are separated by interface.
- Dispersed flow: Finite amount of components in dispersed phase (e.g. droplets, bubbles) which are spread within the volume of the other, continuous phase.
- Mixed Phases: Presence of both separated and dispersed phases.

Different examples of multiphase problems are classified with respect their phase type and are indicated at figure 1.2. Examples of flow regimes include discrete gaseous bubbles in a continuous liquid, discrete fluid droplets in a continuous gas/liquid , discrete solid particles in a continuous fluid (i.e. particle-laden), melting of binary solid, large bubbles in a continuous liquid (i.e. slug flow), continuous liquid along walls, gas in core (i.e. annular flow), immiscible fluids separated by a clearly-defined interface (i.e. stratified/free surface flows) [16].

The mathematical modelling of multiphase flows can be done with three ways:

- theoretically, through using governing equations and other mathematical formulas,
- experimentally, in fully- equipped laboratories, and
- using CFD packages by taking advantage of modern high-tech computers and their processors.

Due to the complexity of the flow in most engineering problems and the inability to apply Navier-Stokes equations for every phase and find the solution for every property at each single point of a multiphase flow, the predictions are based mainly on computational models and secondary on theoretical models. Testing experimentally can be very expensive for most of the problems and even impossible for others [12].

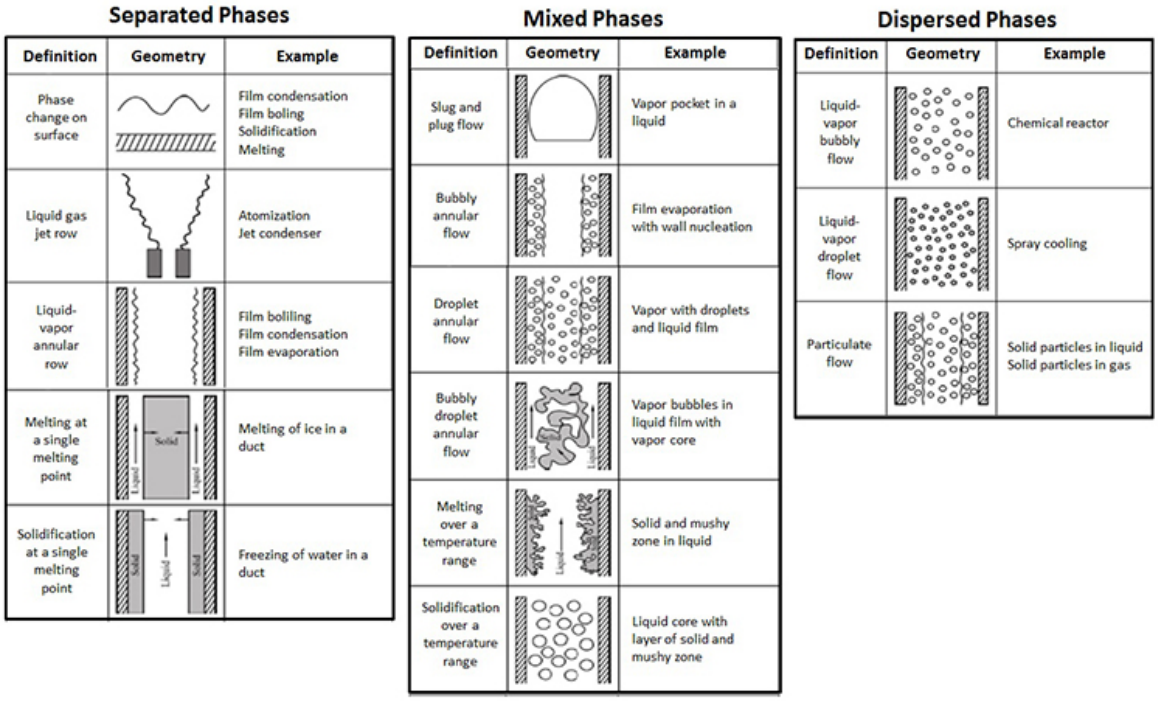

Figure 1.2: Multiphase flow regimes classified according to the type of phases as illustrated in [14].

In the case of multiphase flow with separated phases,the simplest approach for uncomplicated problems is to split the problem into different single-phase flows, apply the governing equations (Navier-stokes and mass conservation) to each of the phases and together with the relevant "jump conditions" at the interface, one can determine the solution [14].

However,the application of an interface analysis in multiphase flow problems with dispersed or mixed phases is impossible. At these cases, a control volume approach within the multiphase flow is usually followed with a space averaging of governing equations over all phases at the same time [14]. No matter which spatial discretization method is used, the volume fraction of each phase is given by the formula

$$\text{Volume of phase}_i = \frac{\text{Volume of the phase in the cell}_i}{\text{Total volume of the cell}}, \tag{1.4}$$

where $i \in [1, ..., n]$ indicates the referring phase in a n-phase flow.

Several mathematical models have been developed for the simulation of the multiphase flow depending on the physical process of the problem and the specification of the flow. The choice of the best model for each case is still a challenging decision. Generating both realistic and simpler models is the key factor for multiphase fluid flow simulations [12]. Two of the most popular mathematical modelling techniques for multiphase flows which are widely used in the literature are the Volume of Fluid(VoF) and the level set method (LS) [17], [1], [18]. Both of them belong under the umbrella of Eulerian front-capturing methods where the interface between the immiscible fluids is depicted as contact discontinuity on a fixed computational stationary mesh [17]. Except them, other commonly used mathematical approaches that can be found in the literature are [16]:

- Lagrangian Multiphase (LMP): Track individual point particles, particles do not interact e.g. in droplet flows.
- Discrete Element Method (DEM): Solve the trajectories of individual objects and their collisions, inside a continuous phase e.g. in particle flows.
- Eulerian Multiphase (EMO): Dispersed flow, particle flows, bubbly flows, boiling heat and mass transfers, interphase mass transfer.

- Eulerian/Lagrangian Dispersed Phase Model (DPM): Particle-wall interaction is always considered, particle-particle is usually not.
- Algebraic Slip Mixture Model (ASM): Neither particle-wall interaction nor particle-particle are considered.
- Eulerian-Eulerian Model (EEM): Particle-wall interaction is considered, particle-particle is usually not.
- Eulerian-Granular Model (EGM): Both particle-wall and particle-particle interactions are considered.
- Various empirical correlations.

Many real-world engineering problems rely on the numerical analysis of fluid flow, which typically consists of more than one phase. Multiphase regimes are taken place in automotive, oil and gas, power generation, paper, and pulp industry and even medicine. In particular, multiphase flow is important in many industrial processes such as fluidized bed in chemical reactors for emergency cooling, gas-liquid flows in evaporators and condensers in thermal power plants, bubbly flows in nuclear reactors, production of hydrocarbon in wells and their transportation in pipelines, pump cavitations, gas-particle flow in combustion reactors and fiber-suspension flows in paper and pulp industry [12], [13], [19], [1].

Last but not least, multiphase flow problems are also met in several natural phenomena. For instance, multiphase flow take place in sediment transport in river flow, withing clouds, at waves on the sea or between plasma and red blood cells in blood flow [12].

1.3. Taylor bubble flows

In pipe flow problems where both gas and liquid flow simultaneously, different multiphase flow regimes may arise (see figure 1.2) depending on the volumetric flow rates, the geometry (pipe diameter and length, wall roughness) and orientation of the pipe and several fluid properties (density, viscosity, surface tension) [20]. Among the resulting flow regimes, there is the case of slug flow where a disperse gas bubble is pushed along by a lighter and faster moving continuous fluid which contains gas bubbles [21]. Slug flow in a horizontal pipe is illustrated in figure 1.3.

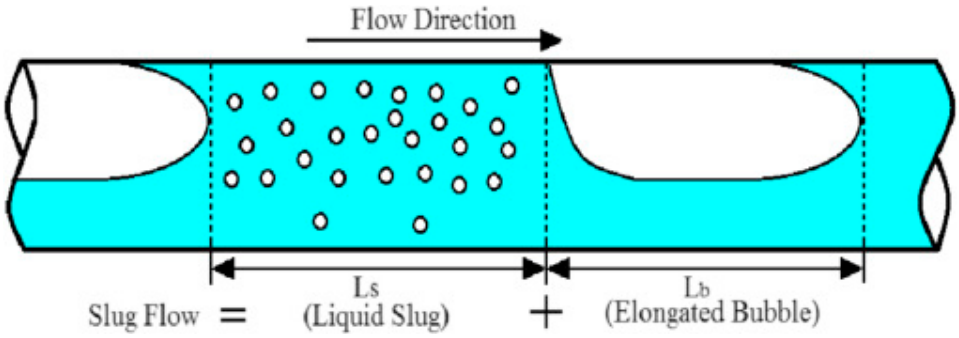

Figure 1.3: Flow regime of slug flow where gas bubbles push along a larger gas bubble in a liquid slug [22].

In the case of slug flow in a vertical pipe where gas is fed with different flow rates at the bottom of the pipe, the small gas bubbles follow a random distribution. The random movement of gas bubbles take place for any liquid velocity. The main difference is that the gravity acts along the pipe flow whereas in the horizontal pipe it was acting along it [17]. If the gas flow rate is further increased, the small bubbles are merging into a larger bubble, which is known as Taylor bubbles [20], [1].

Taylor bubbles are of bullet shape and occupying most of the pipe diameter and as the Taylor bubble's size is increasing, the thickness of the liquid film between the pipe wall and the bubble is becoming smaller. In real-world problems, Taylor bubble is often followed by other Taylor bubbles. The sequence of Taylor bubbles is separated by liquid slugs which consist of smaller dispersed bubbles[20]. Taylor bubble is moving along the pipe under the effect of gravitational, inertial, viscous and interfacial forces [1].

A very important parameter that influences the flow is the presence of the bubble wake behind the Taylor bubble. The possibility of the existence of the wake increases as the Taylor bubble is rising and the thin liquid film decreases. As it approaches the bottom of the pipe, the annular thin film moves downstream the Taylor bubble, within the area of liquid slug, and may create a wake. The possibility, the region and the order of magnitude the wake depends on the trailing edge of the Taylor bubble, the distance between two Taylor bubbles as well as on fluid properties(density, viscosity, surface tension, etc.), flow conditions (liquid and Taylor bubble velocity, temperature) and pipe geometry (wall roughness and pipe diameter and length) [20] .

Vertical gas-liquid slug flow with the creation of Taylor bubbles is met in many industrial processes such as in geothermal power plants, evaporation, and condensation in thermal power plants, oil extraction from wells, transportation of hydrocarbons through pipes and in the emergency core cooling of nuclear reactors [20], [1].

The first chapter included an introduction to Computational Fluid Dynamics and Multiphase Flows with a focus on Taylor bubble flows. Next, the literature review on Taylor bubble flows is indicated followed by the scientific gap and the preliminary research questions in which the current work replies to. Basilisk software is introduced in the third chapter while in the fourth, the developed code is tested against published studies in the limits of a laminar bubble flow, laminar Taylor bubble flow and turbulent co-current Taylor bubble flow. After the successful validation of Basilisk code for all these cases, the turbulent counter-current Taylor bubble flow is simulated and its results are presented in chapter five together with an extensive analysis in the effect of the choice of pipe diameter and initial bubble's length on loss of void. The current work comes to a conclusion in chapter six with an overall presentation of the results.

2

Literature review on Taylor bubble flow

The main target of the literature study is to illustrate the state-of-the-art numerical simulations and experimental results for the motion of the Taylor bubble within a pipe through background liquid flow and indicate the current scientific gap that can be explored through the master thesis work. The main target of the literature study is to illustrate the state-of-the-art numerical simulations and experimental results for the motion of the Taylor bubble within a pipe through background liquid flow and indicate the current scientific gap that can be explored through the master thesis work.

2.1. Numerical Modeling

The gas-liquid interface between Taylor bubble and the liquid within the pipe flow can be identified and controlled by using the appropriate numerical modeling method. The interface is non-stationary and its' form is changing in time. Therefore, a good numerical model provides the user the knowledge of gas-liquid interface's location and curvature at each time step. It is important to notice at this point that the choice of a numerical flow modeling technique is not a standalone flow solving algorithm. The governing equations describing the motion of the flow have to be solved separately like in all kinds of advection algorithms.

Significant efforts have been done for the numerical modeling of the Taylor bubble flow over the last decades. The different numerical techniques for multiphase flows can be characterized as either Eulerian front-capturing or front-tracking techniques. The main difference is that at Eulerian front-capturing techniques, the thin interface between gas-liquid on a fixed computational stationary mesh is interpreted as touch discontinuity and is implicitly specified by an indicator function while in the Eulerian front-tracking techniques, the interface is explicitly rebuilt.

Although there are some publications in which Eulerian front-tracking techniques are utilized for Taylor bubble flows ([23], [24], [25]) , the majority of the researchers are using front-capturing methods and therefore, this literature study focus only on the latter [26], [27], [18], [28]. The most famous among them which can be found in the literature are the Volume of Fluid (VoF) and the level set method (LS). Both modeling techniques have some important disadvantages and for this reason many researchers have recently tried to define dual interface techniques which combine VoF and LS methods in order to minimize the drawbacks and increase solver's efficiency [17], [29].

2.1.1. Level-set method

The level set method is widespread among researchers for the simulation of Taylor bubble flows [30], [31], [32], [33]. The LS method provides an easy and implicit idea for the construction of the gas-liquid interface in the domain and it was first introduced at [34].

According to [35], the LS method is defined as " a particular family of transportation models in which a distance function (named level-set function) is transported". This distance function ϕ is an Eulerian function and is computed with respect to an interface, i.e. the interface (which is a surface in three-dimensions) is defined to be at the zero level set of the distance function. The distance function is a scalar quantity which is positive at the one phase (e.g. gas) and negative at the other phase(e.g.

liquid) as shown in figure 2.1 obtained by [36]. The level set function ϕ is a signed scalar quantity which is advected by the moving fluid and can be applied to the transport equation [35], [32]:

$$\frac{\partial \phi}{\partial t} + \mathbf{u} \cdot \nabla \phi = 0, \tag{2.1}$$

where u is the fluid velocity. The numerical solution of the level-set equation can be done with e.g. Finite-difference methods or upwind methods.

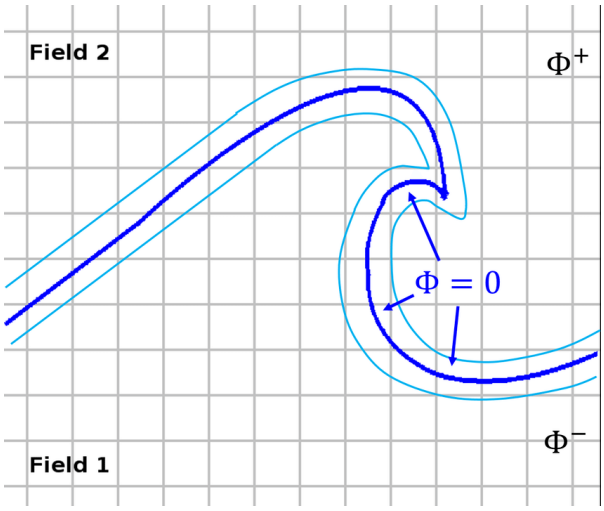

Figure 2.1: Schematic view of a Level-Set method on a moving interface, in green two isocontours of the Level-Set function Φ+ and Φ− are represented on each side of the interface as shown in [36].

Another important characteristic of the level-set function is that it should be an Eulerian function which means that the $||\nabla\phi|| = 1$. In Taylor bubble flows, the level set function ϕ may lose this property after some steps because of dissipation. As a consequence, it is necessary a re-initialization process should be applied every few iterations so that the Eulerian property is satisfied.

Unlike VoF method, any discontinuities near the interface at the values of the properties between gas and liquid would lead to stability issues. Therefore, at LS method it is essential to define a Heaviside kernel function $H(\phi)$ which usually is defined as:

$$\begin{cases} H(\phi) = 1 & \text{if} \quad \phi \geq 0, \\ H(\phi) = 0 & \text{if} \quad \phi < 0 \end{cases} \tag{2.2}$$

With the help of the smooth Heaviside kernel function, the material properties such as density and viscosity can be defined:

$$\rho(\phi) = H(\phi)\rho_g + (1 - H(\phi))\rho_l \tag{2.3}$$

$$\mu(\phi) = H(\phi)\mu_g + (1 - H(\phi))\mu_l, \tag{2.4}$$

where $\rho(\phi)$ represents the density with respect the distance from the interface, ρ_g the gas density, ρ_l the liquid density, μ the viscosity with respect the distance from the interface, μ_l the liquid viscosity and μ_g the gas viscosity.

Therefore, no matter how complex the multiphase flow is, the level set method can model easily the interface with the help of the smooth distance function even for sharp changes on fluid material properties. In some cases, due to the big differences of the velocity field, the distance function may show some deformations which lead to inaccurate results for the distance function in the areas far away from the interface. In order to fix this problem, some researchers tried to improve the accuracy by defining a correction function for re-distancing the level set contours [32]. Figure 2.2 indicates the results of the simulation of a rising bubble in a liquid domain using a conservative LS method [31]. This method decreases the problem of mass conservation of the standard level-set methods which was introduced by

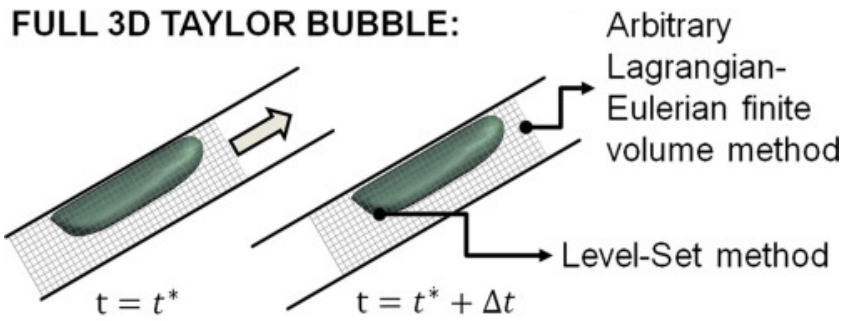

Figure 2.2: Simulation of a rising bubble which was implemented in [31] using conservative LS method as verified at [37].

Balcázar at [37]. The idea of conservative LS method is the basis for the coupled/dual interfaces and it will be analyzed further later.

All in all, the LS method is relatively straightforward to be applied, computationally cheap and integrate smoothly complex topology changes. Therefore, it is easy to compute the mixture viscosity, density and surface tension. Moreover, the LS method shows good stability properties even for high gradients. However, the numerical implementation of interface advection with LS method is unable to preserve the volume of liquid and gas over time and therefore, although the individual phase volumes may change over time, with the LS method they will remain constant due to the fact that conservation of ϕ does not imply conservation of mass [31].

2.1.2. Volume of Fluid method

Although the first publication of the VoF method was done four decades ago [18], the method still remains popular due to its' reliability and effectiveness and comprises the basis for the modeling of multiphase flows and in particular, of Taylor bubble flows. The VoF method, opposed to the LS method conserves the volume of the phases with time since the change of topology is implicit in the algorithm but it cannot give the specific position and curvature of the interface within a volume cell. As a consequence, the model needs more computations so that the user can identify the location of the interface and therefore, which leads to important CPU times. Therefore, VoF approach has in general more computational cost than LS method.

There are numerous publications simulating a Taylor bubble flow by using VoF method for the flow modeling [26], [27], [38], [39]. Many correction algorithms have been proposed for the improvement of efficiency and accuracy of the VoF method but the main idea is the same in all the cases.

After the mesh generation and the division of the domain into mesh cells, the idea of VoF method involves the definition of the volume fraction α. The volume fraction is a scalar function α which represents the quantity of gas (or liquid) in an individual computational mesh cell. It can be computed by

$$a_{i,j,k}h^3 = \int\int\int_{(i,j,k)} \chi(x,y,z)dxdydz, \tag{2.5}$$

where h is the mesh size and χ is the characteristic function of gas (or liquid) within the cell.

There are three different cases for the values of α in a single cell:

- α=1 , i.e. the cell consists only gas.
- α=0 ,i.e. the cell consists only liquid.
- 0< α <1, i.e. the thin gas-liquid interface passes through this cell. In this case, α is a discontinuous function and its' value jumps from 0 to 1 at some point within the cell. At the sudden increase of α from 0 to 1, the user can identify the direction perpendicular to the gas-liquid interface by using several approaches (Parker and Yong's method, finite difference method, Least-squares method etc.). In the three-dimensional case, the interface is represented by a plane while in two-dimensional case, it is just a line. However, the exact location and the curvature of the interface cannot be defined accurately and therefore, more local grid refinement has to be done which means more computational cost.

The volume fraction is applied in all cells for all time steps. The density and the viscosity of the fluid at each space point are not constant and their values are computed with the help of the volume fraction. When α=0, the density and viscosity at this space point (and at a specific time step) are given by the liquid's density and viscosity whereas when α=1, are given by the density and viscosity of the gas. In the case where the interface is passing through a cell, the density and viscosity are computed by linear interpolation:

$$\rho = \alpha\rho_g + (1-\alpha)\rho_l \tag{2.6}$$

$$\mu = \alpha\mu_g + (1-\alpha)\mu_l, \tag{2.7}$$

where ρ represents the mixture density, ρ_g the gas density, ρ_l the liquid density, μ the mixture viscosity, μ_l the liquid viscosity and μ_g the gas viscosity [1].

The transport equation (or convection-diffusion equation) is a generalization of continuity equation and describes how a scalar quantity is transported in space [40]. Therefore, it can be applied to the volume fraction α after having an approximation for the interface. In the case of volume fraction, the transport equation should be solved without diffusion in order to eliminate smearing of the free-surface. Therefore the flux of α between mesh cells can be found by

$$\partial_t\alpha + \mathbf{u}\cdot\nabla\alpha = 0, \tag{2.8}$$

where $\mathbf{u}$ represents the mixture velocity which varies from cell to cell. The mixture velocity applied also to mass conservation (equation 1.3) the Navier-Stokes equations (equation 1.1) which now take the forms:

$$\frac{\partial\rho}{\partial t} + \nabla\cdot(\rho\mathbf{u}) = 0, \tag{2.9}$$

$$\partial_t(\rho\mathbf{u}) + \nabla\cdot(\rho\mathbf{u}\mathbf{u}) = -\nabla p + \rho\mathbf{g} + \nabla\cdot(2\mu D) + \sigma k\mathbf{n}\delta(n), \tag{2.10}$$

where μ and ρ are computed for each cell according to equations 2.6, 2.7, D illustrates the deformation tensor, σ surface tension, k the surface curvature, n the surface normal component, and interfacial Dirac delta function $\delta(n)$ .The last term in the right-hand side of Navier-Stokes equations represents the capillary term and is defined as the extra force applied onto the fluid because of the surface tension between gas and liquid and is non-zero only at the cells where $0 < \alpha < 1$, i.e. cells in which the gas-liquid interface is passing through. For incompressible flows the mass conservation equation 2.9 converts into $\nabla\cdot\mathbf{u} = 0$ [1].

The system of equations described before (equations 2.6 - 2.10) consists of seven equations for a three-dimensional Taylor bubble flow (since equations 2.10 gives one equation for each velocity component) with seven unknowns (ρ, μ, α, p, u_x, u_y, u_z) for each cell. In particular, a VoF algorithm solves the problem of updating in time the volume fraction α given the fixed mesh, the velocity field, the pressure distribution and the volume fraction α at the previous time step for all cells.

This means that the interface is rebuilt in each time step and the VoF method does not track the interface explicitly. The problem which occurs during the reconstruction of the interface in each time step, is that its' location and curvature should be approximated by knowing only the volume fraction of the cells from which the interface is passing (where $0 < \alpha < 1$) and their neighboring cells.

Several methods for the reconstruction of the interface exist, depending on the required accuracy and the computational cost and time. Among these, there are models with first-order accuracy where the reconstruction of the gas-liquid interface is done from a sequence of segments lined up with the grid cells. Most of the examples of first-order accuracy models are improvements on either the simple line interface calculation (SLIC) or the SOLA-VoF algorithm [41], [18], [42].

More accurate VoF techniques try to fit the interface through piecewise linear segments. One of the most widespread approach is the Piecewise Linear Interface Calculate (PLIC) [43]. The distinguishing feature of algorithms like PLIC is that they rebuilt the gas-liquid interface as a discontinuous (with asymptotically small discontinuities) and not as a continuous chain of segments as illustrated in 2.3. PLIC algorithm consists of a reconstruction and a propagation step. No matter how big is the curvature of the approximation of the interface, PLIC algorithm gives robust solutions and the discontinuities of interface's location may vary from $O(h^2)$ to $O(h^1)$ [42], [44], [45].

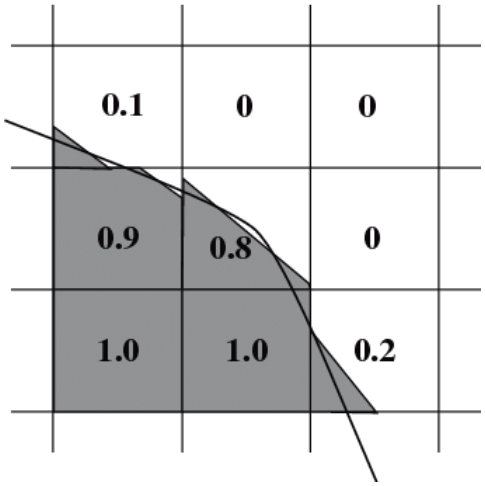

Figure 2.3: The basic principle of the VoF piecewise linear interface calculation (PLIC) method: the interface is reconstructed by linear unconnected segments in each cell [45].

Moreover, there are also publications with high-order discretization schemes for the advective transport equation of multiphase flows which can also apply to Taylor bubble flows [46], [47]. All in all, the effectiveness and the accuracy of VoF method depends heavily on the choice of the discretization scheme used for the advection of the volume fraction.

2.1.3. Dual-interface methods

The bigger disadvantage of the LS method for the numerical modeling of interface advection in Taylor bubble flows is the lack of the conservation of volume of liquid and gas phase in time while, on the other hand, the VoF method requires many computations and local refinements to identify the location of the thin interface between the two phases. Those problems can be solved by using a coupled method that applies both LS and VoF such that the combined modeling technique eliminates the drawbacks of each method and at the same time keep their advantages. In particular, with a combined method the user can have both track and control of the interface location with low computational cost.

There can be found many several coupled/ dual-interface methods in the literature. The slightly differences between the coupled methods are mentioned on the way of the interaction between LS and VoF method. The final choice for the combined solver for the interface simulation of the Taylor bubble flow depends on the user and at the problem's requirements for efficiency, accuracy and computational time. Some examples of dual-interface methods are the coupled volume-of-fluid and level set method (VOSET) [48], the adaptive coupled level-set/volume-of-fluid (ACLSVoF) method [49], the novel coupled method for unstructured meshes [50], the Mass-Conserving Level Set method (MCLS) method in Cartesian coordinates [51] and its' improvement in cylindrical coordinates [17]. At this literature study, an detailed analysis of the MCLS method in cylindrical coordinates is presented which has been used in the past for the modelling of Taylor bubble flows. The small differences between the methods can become comprehensible by studying the relevant literature.

The distinguishing feature of the Mass-Conserving Level Set method is that it achieves mass conservation by calculating the VoF value at each cell through the level-set function and its gradient. This feature can be applied both on a uniform Cartesian grid or a cylindrical grid and one of its' applications comprises the Taylor bubble flow. The MCLS method has been validated for indicating good levels of robustness and accuracy in comparison with the rest coupled methods [51], [17]. Moreover, the algorithm in cylindrical coordinates tried to eliminate all instabilities and possible singularities that may occur in the multiphase flow field, accomplish competent accuracy (minimum second order) and at the same time to be computationally cheap. The reason is that the algorithm is designed such that it can apply to turbulent flows where irregular fluctuations in time as well as in space, small as well as large three-dimensional eddies (vortices) coexist. To achieve this, the domain is limited to a straight, inclined, cylindrical pipe [17].

The MCLS algorithm is illustrated at figure 2.4. For clarity, the explanation of the algorithm will be done by keeping the same notation with the literature:

- The level-set or distance function of the center of each cell to the interface is given by $\phi_{i,k}^{(n)}$ at time step n.
- The volume fraction or volume value of the center of each cell at VoF is given by $\psi_{i,k}^{(n)}$ at time step n.

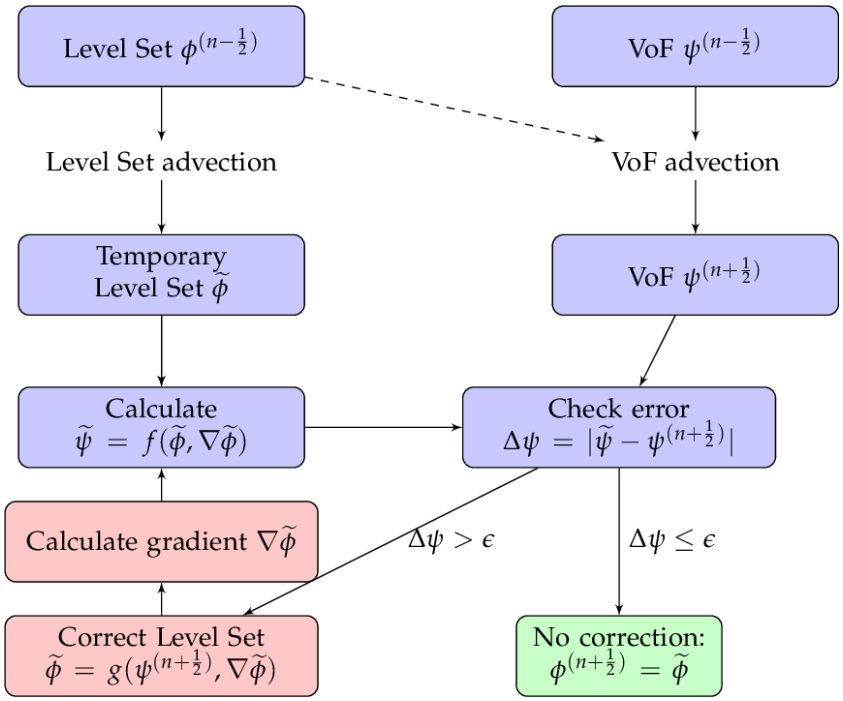

Figure 2.4: MCLS algorithm with Level-Set function ϕ, VoF function ψ: The left-hand side branch corresponds to pure Level-Set advection. The right-hand side branch represents the VoF advection [17].

The idea of the method is that we can fix the lack of the mass conservation LS method by applying some corrections to the Level-set function $\phi_{i,k}^{(n)}$ which are derived from volume fraction $\psi_{i,k}^{(n)}$ of VoF method for every cell and every time step. This is done with the following steps (2.4):

- Firstly, the LS function $\phi_{i,k}^{(n-\frac{1}{2})}$ and the VoF function $\psi_{i,k}^{(n-\frac{1}{2})}$ are advected together with the velocity field at the time step $n-\frac{1}{2}$.
- Then, by solving numerically the advection equation for LS, a first prediction of the level set $\tilde{\phi}_{i,k}^{(n+\frac{1}{2})}$ for each cell at the next time step is approximated. Simultaneously, the VoF fraction $\psi_{i,k}^{(n+\frac{1}{2})}$ is computed through its' advection algorithm for which it is known that the mass conservation property holds.
- Next, the computed accurate value of volume fraction $\psi_{i,k}^{(n+\frac{1}{2})}$ is compared at each mesh cell with an approximate value of volume fraction $\tilde{\psi}_{i,k}^{(n+\frac{1}{2})}$ obtained as the result of a non-linear function f which takes as arguments the approximate values $\tilde{\phi}_{i,k}^{(n+\frac{1}{2})}$ and $\nabla\tilde{\phi}_{i,k}^{(n+\frac{1}{2})}$ and maps them to the volume fraction of VoF. The comparison checks for each cell if the discrepancy between the approximated value and the accurate value of volume fraction of VoF method is smaller than a user-defined value ϵ. The choice of ϵ is important for the accuracy and the computational cost of the method.
- Depending on the result of the comparison, the initial approximation of $\tilde{\phi}_{i,k}^{(n+\frac{1}{2})}$ for every cell may (if discrepancy is bigger than ϵ) or may not be corrected (if discrepancy is smaller than ϵ).

- If a correction is need, the algorithm continues by computing a new approximated value $\tilde{\phi}_{i,k}^{(n+\frac{1}{2})}$ of level set function. This is done by calculating the inverse function of f, namely g, which takes as arguments the computed accurate value of volume fraction $\psi_{i,k}^{(n+\frac{1}{2})}$ and the $\nabla\tilde{\phi}_{i,k}^{(n+\frac{1}{2})}$ from the initial guess.

- After calculating the new approximated value of level-set function $\tilde{\phi}_{i,k}^{(n+\frac{1}{2})}$, its' gradient is computed and a new approximation of $\tilde{\psi}_{i,k}^{(n+\frac{1}{2})}$ is obtained.

- The comparison check continues iteratively until the required tolerance is achieved for all cells. Then we can proceed with the next time step.

2.2. Software used for the Simulation of Taylor bubble flow

There is a big variety of open source and commercial software packages that are widely used in research and industry for the simulation of the Taylor bubble flow. Since there is no analytical solution to the Navier-Stokes equations for the Taylor bubble flow problem, the error of a simulation can be hard to quantify. This is the reason why an experiment is often chosen to confirm the findings of the simulations and the validation of theoretical models. Therefore, for the verification of the accuracy of CFD software in Taylor bubble flows, we intended to find articles where the results from simulation were also followed by experiments under the same physical flow conditions, e.g. same Reynolds number [10]. In cases where the simulation results are not followed by an experiment (due to cost or complexity of the flow), the researchers compare their findings with previous publications which simulated exactly the same problem under identical conditions but with different software or flow modeling method. Moreover, there are a few cases of papers with a code comparison for Taylor bubble flow simulations. Since each software package uses its own parameters and variables for describing the same problem, a mapping between the software's parameters was needed.

During the current literature study, an important parameter is the version of the software package that was used in the bibliography because the target was to capture the latest versions of each software. Therefore, the search was limited to the results from the last decade so that the most recent documents are gathered.

2.2.1. Commercial software packages

VoF method has been known for several decades, has gone through a continuous process of improvement and is used by several commercially available software programs the last decades for simulation of rising bubble flow problems [52]. On the other hand, other numerical methods for multiphase flow modeling such as Level-set method, dual-interface methods, front-tracking methods, etc. have either recently or not yet been developed in the most popular packages [52]. Therefore, the only way to perform these methods is through user-defined functions such as in the recent numerical studies implemented in ANSYS Fluent [53], [54], [55], [56].

ANSYS Fluent is the most widespread CFD software package used for simulations of multiphase flows and in particular, for the motion of a rising bubble in a liquid. In ANSYS Fluent, there are both Eulerian-Eulerian two-fluid models and Lagrangian discrete phase models. For Taylor bubble flow, three different Euler-Euler multiphase flow modeling methods are available: the VoF, the mixture, and the Eulerian-Eulerian model [52], [57]. Front-tracking methods for flow modeling are not yet available on ANSYS Fluent and they can still be performed only via user-defined functions such as in [56].

The VoF model is the easiest and most popular method to be implemented in ANSYS Fluent, nevertheless, there are some limitations in the model's implementation and especially in the early versions [52]. For example, in Release 12.0 the restrictions in the use of VoF modeling contain that the simulation can be implemented only by the pressure-based solver, stream-wise periodic flow cannot be used and second-order implicit time-discretization scheme is not possible [58].

Despite those restrictions, predictions from numerical simulations are found to be accurate even for early versions. For instance, the simulation of a Taylor bubble flow in both stagnant and flowing liquid is implemented in Fluent (Release 5.4.8) using VoF method in [27] and the findings are found to be in good agreement with experimental results obtained from literature [59].

However, in the early versions, the LS method is not available and therefore, a coupled LS and VoF method could be performed only via the tool of user-defined functions. For example, the coupled LS-VoF (CLSVoF) method for modeling of gas-liquid interface in bubbly flow as presented in [54]. The authors eliminated the drawbacks of both individual methods and achieved a CLSVoF method by using the available VoF method in ANSYS Fluent (version 6.3.26) and performing LS method via user-defined functions.

The latest versions of ANSYS Fluent show a significant improvement in the accuracy of the numerical simulations of Taylor bubble flow. For example, the VoF methodology of ANSYS Fluent (Release 12.0.1) is performed in the numerical survey about the rising of Taylor bubbles through a stagnant Newtonian liquid [4]. The results obtained for the velocity and the frontal radius of the nose of the Taylor bubble are favorably compared with a published collection of data from experimental measurements [60].

The next release (14.0) of ANSYS Fluent is the first version which had available the CLSVoF method so that the deficiencies of the LS method and the VoF method are overcome. The efficiency of CLSVoF method is illustrated in a numerical study for the bubble formation in a square microchannel with a converging shape mixing junction with background liquid flow [53]. The comparison between VoF and CLSVoF model of ANSYS Fluent indicated that with CLSVoF model a more accurate interface can be achieved especially at the rupture stage of the bubble and the bubbles obtained, were more consistent with the experimental outcome.

A finite-volume-based CFD solver ANSYS Fluent of Release 14.0 is also performed in the numerical simulation for the dynamics of bubble formation from two submerged orifices in an immiscible Newtonian liquid [61]. The dynamic effects of the quiescent and the co-flowing liquid ambiance on the bubble evolution and detachment processes were compared with experiments from literature [62].

Release 15.0 is applied for the simulation of rising Taylor bubbles in [24], [55]. In [24], VoF method is applied in the flow field and the values obtained are matching favorably with published experimental and other modeling findings [63] while in [55], a numerical study for the bubble dynamic behavior utilizing the coupled Level Set and Volume of Fluid (CLSVoF) method is illustrated. The authors in the latter study used also the tool of user-defined functions but only for the mass and energy transfer and not for the CLSVoF as in [54].

ANSYS Fluent 16.0 was used for performing a detailed numerical study focused on the mass transfer phenomenon from Taylor bubbles of pure oxygen to co-current liquid initially absent of solute is presented in [39]. The authors implemented a VoF method for capturing the interface accurately.

Another well-known commercial CFD software package is the STAR-CCM+ software. STAR-CCM+ offers a wide choice in modeling multiphase flows and is implemented in many researches flows such as in [64]. In this publication, the aim was to indicate the accuracy of numerical simulations using STAR-CCM+ (version 10.06.010) with VoF modeling in slug flow conditions and in particular, in Taylor bubble flow. STAR-CCM+ has been validated in several studies for Taylor bubble flow and can give accurate predictions. For example, in [64], the divergence of the prediction from experimental results is less than 2%.

Last but not least, NEPTUNE CFD, which is based on a finite volume approach, is a multiphase-flows solver which can be used for Taylor bubble flows like in [36]. NEPTUNE CFD is powered by Code Saturne HPC capabilities and can be embedded in the SALOME platform.

2.2.2. Open source software packages

Open-source means that the user is free to view and modify the underlying code of the software. This approach is beneficial to researchers in at least two ways; First, they can freely release their data and experiments so that anyone can replicate the study just by downloading and installing the software; Secondly, the original code is open to be read and so anyone can check the validity of either the mathematics or other technique's used in the publication. This can not always be done with commercial software packages, as not everyone has access to them because of their cost and the code, is often treated as secret so no one can read it.

OpenFOAM is an open-source CFD software package and comprises a collection of C++ libraries. OpenFOAM and its' libraries are widely used for simulation of multiphase flows and in particular, Taylor bubble flows [65]. Until the last decade, OpenFOAM and most open-source CFD software packages were not yet released [66], and therefore, the majority of the CFD simulations in multiphase flows were done with commercial software packages. OpenFoam has a standard two-phase incompressible flow solver for VoF method, namely InterFOAM, which solves the two-phase equations of flow on collocated

grids using finite volume discretization [1], [38].

A numerical prediction for the motion of Taylor bubbles rising in a liquid using OpenFOAM is presented in many studies. For example, OpenFOAM version 2.3 and its' multiphase solver InterFOAM is used in [38] while a modified version of the standard InterFOAM VoF solver (OpenFOAM 4.0) for unstructured grids is applied in [1]. The two main differences of the latter study from standard InterFOAM version are the lack of the dissipative term in the incomplete flux and the two-stage Diagonally Implicit Runge-Kutta (DIRK) for the time integration scheme. In both studies, the results are compared favorably with the other numerical and experimental results [67], [68], [69], [70], [4], [3].

Another efficient open-source code for Taylor bubble flows is the Parallel Hierarchic Adaptive Stabilized Transient Analysis (PHASTA). PHASTA software comprises a direct numerical simulation (DNS) flow solver which can model compressible or incompressible, laminar or turbulent, steady or unsteady flows in 3D, using unstructured grids. PHASTA adopts the LS and not the VoF method for the modeling of the interface of the two-phase bubble flow. PHASTA may give from second to fifth order of accuracy and is based on a stabilized formulation of Finite Element Method (FEM) and have been confirmed many times in the past for various configurations of bubble flows [71], [72]. For example, in [32], a three-dimensional numerical analysis of the dynamics of large deformable bubbles in pipes of different geometries and orientations was implemented using PHASTA. PHASTA is also used in a novel algorithm which has been recently published in order to prevent or delay bubble coalescence while simulating multiple bubble behavior using LS approach at large scale [30].

A parallel c++/ MPI code, called TermoFluids is designed for direct numerical simulation and large eddy simulation of turbulent flows and it is used in many studies. For example, a numerical study of Taylor bubbles rising in a stagnant liquid using a coupled conservative LS-moving mesh method is tested in [31]. TermoFluids was also used in the research for the simulation of single and multiple bubbles with the conservative LS method which is performed in [37]. The same authors use also TermoFluids in another two researches for multiphase flows; a coupled VoF/LS method for simulating incompressible two-phase flows on unstructured meshes and a finite-volume/level-set method for simulating two-phase flows on unstructured grids [50], [33].

Moreover, a novel numerical two-phase flow algorithm in cylindrical coordinates was implemented in FORTRAN 90 in [17]. The case of Taylor bubble flow in is tested and the accuracy of the code is compared with the results from other studies which used different software [23].

2.2.3. Comparison between CFD software

Regarding code comparison, some empirical parameters and model details have to be changed to obtain comparable agreement between different codes which simulate the same problem. Therefore, it is necessary to perform a mapping between the various software parameters to apply a comparison.

For example, a comparison of commercial software packages ANSYS Fluent and Transport phenomena Analysis Tool (TransAT) have been implemented for the simulation of bubbly flow case in [73]. VoF modeling is adopted in Fluent while LS model is selected in TransAT which is developed by ASCOMP GmbH [74]. The results indicate a recirculating flow for bubbles by TransAT while negligible recirculation was observed in the solution with Fluent. In general, the TransAT captured the instabilities and therefore, it predicted with better accuracy the slug flow in comparison with the experimental findings. The computation times between the two methods are similar.

A code comparison has been also implemented for dispersed bubble flow. For example, a code comparison between OpenFOAM (version 2.2.x) and ANSYS CFX for monodisperse bubbly flow was executed and their predictions are compared with results from experiments [75]. Another study for CFD simulations of a bubble column with and without internals compare results between OpenFOAM and ANSYS Fluent [76]. In both examples, comparable results obtained with both commercial and open-source codes (deviations around 3-4%) for different configurations of multiphase bubble flows in [76] although some differences in the procedure remained [75]. For example, for the implementation of the turbulent wall functions in [75], cell-centered discretization is used in OpenFOAM while a vertex-based scheme is preferred in ANSYS-CFX. In general, although the experimental data are satisfactorily reproduced by the numerical simulations implemented in OpenFOAM, some deviations from experimental results have been identified.

Similar efforts for the comparison between open-source and commercial software packages and their matching with the experimental results have been also done for flows in micro-scale pipes (with a diameter of less than 1mm). An interesting research paper in this field was the numerical as well as the

experimental examination of the dynamic behavior of isolated confined air bubbles in laminar fully-developed flows within circular channels of very small diameters [77]. The experimental results derived from the micro-particle velocimetry technique were compared with the outcome of the computational fluid dynamic simulations performed both in ANSYS Fluent v.14.5 and ESI OpenFOAM v.2.1.1. The paper concludes that numerical results coming from both ANSYS Fluent and OpenFOAM agreed well with the experimental results in the majority of cases (errors always smaller than 10%) and the discrepancies occurred between experimental and numerical bubble velocity and liquid film thickness are within the error bands of the experimental measurements. Only in cases of large capillary numbers, the results of the dynamics of the liquid film for air-water flows were slightly better using ANSYS Fluent in comparison with OpenFOAM because OpenFOAM resulted in narrower bubbles which led to errors in the surface tension forces. In the extreme case of significantly small capillary numbers, even the experimental results led to absolute errors up to 30% while in normal cases the error coming from experiments is assumed negligible or it is identified and subtracted [77].

2.3. Previous simulations in Taylor bubble flows

A large amount of studies is published every year in the dynamics of Taylor bubbles rising within vertical pipes which also contain viscous liquid. The reason is that the formation of Taylor bubble flow is met in many industrial applications such as in geothermal power plants, steam boilers, and heat exchangers in thermal power plants, oil extraction from wells, transportation of hydrocarbons through pipes, blood flows and in the emergency core cooling of nuclear reactors [25], [20], [1].

The shape of the Taylor bubble may be different even for the same application. In general, Taylor bubble is always bullet-shaped with a rounded leading edge, a cylindrical main part and either a more rounded or more flattened trailing edge. The width of the Taylor bubble usually conceives almost all cross-section of the pipe and therefore, a very thin film of liquid exists between the bubble and the pipe walls [1]. As this thin film decreases, a wake is created in the region behind the Taylor bubble. The wake region depends on the trailing edge of the Taylor bubble, fluid properties, flow conditions, and pipe geometry [20].

Taylor bubbles usually appear in sequences, i.e. behind a Taylor bubble another Taylor bubble is flowing with similar shape and velocity. The so-called liquid slugs which consist of smaller dispersed bubbles are present between two Taylor bubbles [20]. The distance between two Taylor bubbles also affects the wake region.

The behavior and motion of the Taylor bubble are affected by a group of non-dimensional numbers. The most important non-dimensional numbers for the Taylor bubble flow are the Eötvös (Eo) or Bond (Bo) number, the Morton (Mo) number and the Froude (Fr) number and are defined as:

- $Eo = \frac{\rho_l g D^2}{\sigma}$,
- $Mo = \frac{g \mu_l^4}{\rho_l \sigma^3}$,
- $Fr = \frac{U_t}{\sqrt{gD}}$,

where ρ_l is the liquid density, μ_l the liquid viscosity, g the gravitational acceleration, D the pipe diameter, σ the surface tension and U_t the terminal velocity of the bubble. In particular, Eo represents the ratio of gravitational forces to surface tension and together with Mo number characterizes the shape of the bubble moving in a surrounding fluid while Fr is the ratio of the flow inertia to the external field (i.e. gravity). The Eo and Mo consists of the input parameters of a simulation while Fr is a number that comes from the outcome of the prediction [17].

However, to be able to sufficiently describe the Taylor bubble flow and derive the non-dimensional governing equations, it is necessary to define another few non-dimensional numbers: the Reynolds (Re) number (defined already in its general form in 1.3), the Archimedes (Ar) number, the Weber (We) as well as the density and viscosity ratio. These numbers are defined as:

- $Re = \frac{\rho_l U_l D}{\mu_l} = \frac{U_l D}{\nu_l}$,
- $Ar = \frac{\Delta \rho g L^3}{\rho_l \nu_l^2}$,

- $We = \frac{\rho_l U_t^2 D}{\sigma}$
- $\lambda = \frac{\mu_l}{\mu_g}$,
- $\eta = \frac{\rho_l}{\rho_g}$,

where $\Delta\rho = \rho_l - \rho_g$ is the density difference and ν_l the kinematic viscosity of the liquid. The Re depicts the ratio of inertia to viscous forces, the Ar the ratio of gravitational forces to viscous forces while Weber number represents the fluid's inertia compared to its surface tension.

The problem becomes more complex as the liquid flow is increasing from (initially) stagnant to laminar and then to turbulent flow [25]. In this chapter, predictions of numerical simulations in Taylor bubble flow which was found in the literature are presented together with their achieved accuracy compared to experimental findings or results from other publications. Taylor bubble flow problems are very complex problems due to the aperiodic and unsteady behavior both in space and time and therefore, there are some restrictions at studies coming only from experimental work without using any simulation [20], [69].

All numerical simulations of rising Taylor bubbles in pipes through liquid background flow are taking into consideration some assumptions in order to reduce the complexity, and therefore the computational cost, of the problem. For example, the majority of numerical simulations of Taylor bubbles flow in cylindrical pipes with laminar or (initially) stagnant liquid background flow are simplified into two dimensions since there is no flow in the circumferential direction. Moreover, the flow is assumed axisymmetric along pipe axis in many studies, and therefore, its motion is governed by a two-dimensional momentum equation in the half pipe domain. Last but not least, in simulations of stagnant liquids with high viscosity, the predictions lead to steady behavior and shape of Taylor bubbles and therefore, there is no need for long (in time) simulations.

As a consequence, the complexity of the dynamics of the Taylor bubble depends on the background liquid flow. Therefore, the current research is divided into three main subsections depending on the background liquid flow within the vertical tube. In particular, the studies are divided into the type of background liquid flow: (initially) stagnant, laminar or turbulent. In most of the literature, the analysis is done on co-current Taylor bubble flow, which means that the Taylor bubble flows in the same direction as the buoyancy force. For example, a schematic sketch of a (half) Taylor bubble rising within a tube filled in with co-current liquid is illustrated in figure 2.5 as presented in [25].

2.3.1. Stagnant liquid

Firstly, studies from simulations of Taylor bubble flows in initially stagnant liquid are illustrated. Although initially the liquid is quiescent, the rule is that as the Taylor bubble is moving up, the liquid ahead of the bubble is starting to accelerate downwards until it reaches a maximum (usually steady) terminal velocity.

The pioneer research on rising Taylor bubbles was carried out in [78] and [79]. Since there was neither simulation tools nor experimental findings, it was only theoretically found that the rising velocity of a Taylor bubble in an inviscid flow was $U_o = \alpha\sqrt{gD}$ where α is a coefficient with value between 0.33 and 0.35. The results of the above studies have been validated experimentally later in [80], [81].

A stabilized finite element method with LS modeling of the interface for the three-dimensional computation of incompressible bubble flowing within an (initially) quiescent liquid is illustrated in [72]. The results from the three dimensional analysis indicate that the capability of the method to manage the bubble coalescence and breakup.

Numerical simulations for three different cases of laminar Taylor bubble flow in an initially stagnant liquid have been implemented in [1], amongst others. The three cases which were tested are convex tail without wake, concave tail without wake, and concave tail with wake. A Moving Frame of Reference (MFR) is attached to the Taylor bubble and non-periodic inlet and outlet boundary conditions are used. The predictions coming from the modified InterFOAM compare favorably with the experimental results from [69], [70] and the numerical models of [4]. The small deviations are justified by some unsteady behavior near the tail of the Taylor bubble. The bubble is predicted to have an (almost) steady value before the first second.

A numerical study of Taylor bubbles rising in an initially stagnant liquid is illustrated in [31]. The governing equations have been discretized on a collocated unstructured grid arrangement with a central

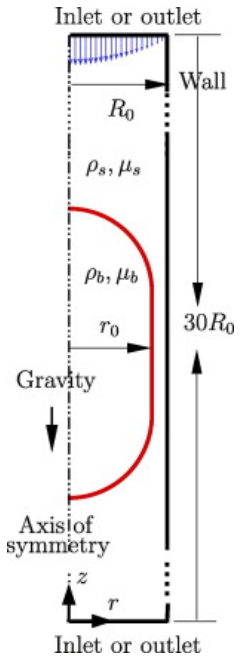

Figure 2.5: Schematic sketch of a (half) Taylor bubble rising in a cylindrical tube filled with co-current liquid as shown in [25]. The co-current liquid can flow upwards or downwards. The Taylor bubble flow within a pipe is an-axis symmetric problem and it is usual to do the half sketch.

difference scheme of the Finite Volume Method (FVM), according to [33] in which rising gas bubbles are simulated in quiescent liquid on unstructured grids. Both studies used TermoFluids for their simulations. The results of the former study show very small deviations from experimental findings [28] and other numerical studies [82], and therefore, the numerical prediction is characterized as accurate.

A conservative level-set (CLS) method has been used to study the buoyancy-driven motion of single and multiple bubbles on a one-directional periodic domain through an initially stagnant liquid in [37]. The equations of CLS have been discretized on a collocated unstructured mesh with a Finite Volume Method and a central difference (CD) scheme is used to discretize the convective term. The simulations were implemented in Termofluids and the predictions are found to be in good agreement with experimental and numerical results from the literature such as in [83] and [84].

Rising Taylor bubbles through initially stagnant liquid is also performed in the simulation in [54]. In this study, a three dimensional Cartesian level set method was coupled with the volume of fluid method within ANSYS Fluent version 6.3.26 which uses a staggered grid. The level set was discretized with a fifth-order weighted essentially non-oscillatory (WENO) scheme for spatial derivatives and a first-order Euler explicit method for temporal discretization. The method was implemented on both serial and parallel solvers. In the end, the authors compared the CLSVoF method with the original VoF and conclude that CLSVoF acquires better accuracy. In particular, the deviation from experiments was less than 16% using CLSVoF whereas with VoF the maximum relative error was 19%.

A three-dimensional simulation has been also applied for Taylor bubble turbulent flow in initially stagnant liquid in [64]. The experiment published in [85] is used as a reference for all calculations. LES calculations implemented with STAR-CCM+ give less than 2% error for a well-refined mesh. The dependency of the results from mesh size and Courant number were assessed in this work.

A complete dimensionless analysis of single Taylor bubble rising through a vertical stagnant Newtonian liquid problem is carried out in [24]. The FVM is used to discretize the governing equations. Using VoF method in ANSYS Fluent, good approximations are found for Taylor bubble's shape and velocity, flow in the liquid film region and flow in the wake region with respect to the experiments [69] and other theoretical models [60].

Stationary liquid is also used in the numerical simulation of Taylor bubbles rising in a vertical tube at [26]. A Finite Difference Method is used for the discretization of NS and VoF for capturing the gas-liquid interface. The simulation was executed with ANSYS Fluent and was matching well with the experimental findings in the literature [86].

Last but not least, similar simulations have been carried out in [38] where Taylor bubbles with turbulent wake and their coalescence have been investigated. An OpenFOAM solver using VoF modeling and FDM discretization gave accurate predictions for void fraction, mean Taylor bubble velocity and turbulent fluctuations. The results were compared favorably with experimental findings [67].

2.3.2. Laminar liquid flow

In several studies, simulation of Taylor bubble flow are performed both in initially stagnant and laminar flowing liquids are illustrated and therefore, it is difficult to categorize them. Although the rule in a flow with initially stagnant liquid is that the bubble reaches a steady state and constant shape, this does not happen always when there is also co/counter-current liquid flow.

Examples of laminar Taylor bubble flow are indicated in [27] and in [50] where a novel coupled method for unstructured meshes is presented. The distance between the front nose of the Taylor bubble and the accelerated liquid is smaller for slower bubbles. The same time at region at the rear of the bubble, a wake may appear which depends on the inverse viscosity dimensionless number N_f. The results of the simulation in [27], which was performed with Ansys Fluent using the VoF method, agree fairly well with experimental and numerical results from the literature. In particular, the shape and velocity of the slug, the velocity distribution and the distribution of local wall shear stress illustrate a great matching with [86].

Numerical predictions for Taylor bubble flow in both co-current and counter-current flow with laminar background liquid flow are presented in [25]. The front tracking method for interface capturing together with the finite difference method for Navier-Stokes equations are used for the dynamic analysis. The Crank Nicholson method is applied for the time integration. The results show that when the co-current flows in the same direction with the buoyancy (i.e. upward flow), the bubble is elongated and the flow separation at the elongated tail is easier. On the contrary, when the co-current flows on a rising Taylor bubble in the direction opposite to the buoyancy force (i.e. downward flow), the bubble becomes fatter and shorter, the tail's shape is more rounded for large Ar numbers and therefore, the flow separation is more difficult.

A new dual-interface capturing method for axisymmetric flows is presented and it is tested for the laminar Taylor bubble case in [17], amongst others. The spatial discretization of the Navier-Stokes equations is implemented by using a second-order accurate finite difference approach as presented in [87]. The momentum equations are linearized with Newton linearization, and the discretization in time is done with an Implicit Midpoint time integration method. The Poisson equation for the pressure is solved by implementing the Conjugate Gradient (CG) method. The simulation is implemented in FORTRAN for two low-viscosity cases and three moderate-viscosity cases and the results are compared with the numerical results of [23] as well as the experiments of [86] and [28]. The deviation of the output Fr number is found to be around 1% in comparison with the numerical simulations of [23]. In general, for all cases, the shape, and the terminal velocity are in agreement with the numerical and experimental findings from literature except for one case of large Reynolds numbers where the bubble breaks up after some time.

A numerical analysis of the dynamics of large deformable bubbles in pipes of different geometries and orientations for laminar liquid flow was investigated in [32]. The reference for the formulation of the three-dimensional set up of the bubbly flow is the experimental conditions used in the literature [88]. Due to negligible movement in the circumferential direction, the problem is described by the governing equations in two dimensions. The results derived from numerical predictions are found to accurately matching with those from both experiments and theoretical models for all configurations.

Simulation of rising Taylor bubbles for varying inlet liquid velocities but always within the laminar range is executed in [39]. For achieving constant solute concentration at the bubble surface, the flow domain is solved by coupling the VoF method with a geometric reconstruction scheme which uses PLIC method as applied in [43]. The simultaneous solution of the flow field, bubble shape, and mass transfer in a domain with stationary walls was predicted accurately. However, the results obtained by ANSYS Fluent for the mass transfer coefficient data from soluble bubbles showed a remarkable divergence in comparison with the existing theoretical models [89], [63]. The reason for this difference can be explained by implementing the relevant experiments.

Two different codes, Transat and ANSYS Fluent, were compared each other for the accuracy of their predictions for the case of rising bubbles in laminar co-current liquid flow, amongst others [73]. The codes use different spatial and space discretization schemes as well as interface tracking methods. The

simulation in Transat was executed with LS interface capturing method, 3rd order Quadratic Upstream Interpolation for Convective Kinematics (QUICK) for spatial discretization and 3rd order Runge-Kutta for time discretization. On the other hand, ANSYS Fluent uses a VoF method, 3rd order Monotonic Upwind Scheme for Conservation Laws (MUSCL) and 1st order Euler correspondingly. Computational times, complexity, accuracy, consistency, recirculation, and stability are checked for both codes and the results are compared with their deviation from experiments found in the literature [90].

2.3.3. Turbulent liquid flow

A Large Eddie Simulation (LES) of turbulent co-current Taylor bubble flow is illustrated in [1]. According to the knowledge of the author, this is the only publication that can be found in the literature which presents a fully three-dimensional simulation that can reproduce the motion of an individual Taylor bubble in a turbulent co-current background liquid flow. In this study, after the validation of the predictions of laminar Taylor bubble flow, a simulation is performed for a turbulent co-current Taylor bubble flow. For the discretization in space, a mixed scheme is used in order to verify stability and at the same time minimize the artificial numerical dissipation. In particular, at the free surface, a Van Leer flux-limiter is used which stabilizes the free surface and suppresses artificial bubble formation together with a second-order central difference scheme in the rest domain. Moreover, a second-order accurate diagonally implicit Runge-Kutta scheme is used for the temporal discretization. The accuracy of the numerical simulation is compared with the findings of [3] for the Taylor bubble in a turbulent co-current liquid flow. The prediction model agrees with the published data from the literature except for an underestimation of the velocity fluctuations close to the Taylor bubble due to the laminarization of the flow in the wake region and the great bubble decay at the bubble's tail.

2.4. Discussion on literature review

The literature study provided in the current chapter comprises the theoretical background necessary for understanding the problem of Taylor bubble flow and provides most of the up-to-date relevant research that has been published. The motivation for this work comprises both the wide variety of engineering systems in which the Taylor bubble flow is encountered as well as the scientific gap that was found. The three main interface modeling methods have been explained in detail and the capabilities and restrictions of each software that has been used in similar studies are indicated. After analytical research, the lack of realistic and accurate data in the laminar, transitional, and turbulent co/counter-current flow has been identified and the current master thesis tries to fill a part of this scientific gap.

In particular, the literature study prospects on performing a high fidelity simulation of Taylor bubbles in co/counter-current turbulent flow. The project is performed in cooperation with the research and innovation unit of NRG using Basilisk software. Corresponding research questions, goals as well as the strategic approach that is followed are stated in this chapter prospecting on the remaining part of the master thesis.

2.4.1. Scientific gap

Numerical simulations of Taylor bubble flows are complex and unsteady problems. Most of the studies found in the literature and presented in chapter 4 try to decrease the complexity and computational cost. For example, this is done by using coarser meshes or performing simulations in a laminar flow which usually leads to two-dimensional problems.

Table 2.1 summarizes the main sources that are found in the literature for the numerical simulation of Taylor bubble flows. The first column indicates the source, the second the interface tracking method, the third the used computational method, the fourth the software package used for the simulation and the last one depicts the type of background liquid flow. It can be observed that almost all studies implement simulations of Taylor bubbles in stagnant or laminar liquid background flow while only [1] simulates Taylor bubbles in co-current turbulent liquid flow.

According to the research of [20], despite the number of studies performed, there is a lack of realistic accurate data in the case of not only turbulent but also transient or even laminar liquid co/counter-current flow. The reason is that important assumptions and different constraints that are used in order to reduce the degrees of freedom, like symmetry, type of flow, flow parameters, or choice of a coarse grid, may affect the consistency of the results. In simulations of stagnant liquids with high viscosity, the predictions lead to steady behavior of Taylor bubbles. However, as Re increases, this two-phase

Table 2.1: This table displays the interface modeling techniques, the discretization method, the software and the type of background liquid flow used for each numerical simulation of Taylor bubble flow found in the literature.

Author-source	interface modeling	discretization method	software	liquid flow type
Oud, [17]	MCLS	FDM	FORTRAN	laminar
Frederix, [1]	VoF	FVM	OpenFOAM	turbulent/ stagnant
Montoya, [64]	VoF	FVM	STAR-CCM+	stagnant
Taha, [27]	VoF	FVM	ANSYS Fluent	stagnant/ laminar
Massoud, [24]	VoF	FVM	ANSYS Fluent	stagnant
Quan, [25]	FT	FDM	not mentioned	laminar
Bugg, [26]	VoF	FDM	ANSYS Fluent	stagnant
Talley, [30]	LS	FEM	PHASTA	stagnant
Gutiérrez, [31]	CLS	FVM	TermoFluids	stagnant
Behafarid, [32]	LS	FEM	PHASTA	laminar
Balcázar, [33]	LS	FVM	TermoFluids	stagnant
Sussman,[34]	LS	FDM	not mentioned	stagnant
Mimouni, [36]	LS	FVM	NEPTUNE CFD	laminar/stagnant
Balcázar, [37]	CLS	FVM	TermoFluids	stagnant
Shaban, [38]	VoF	FDM	OpenFOAM	stagnant
Silva, [39]	VoF	FEM	ANSYS Fluent	laminar
Balcázar, [50]	CLSVoF	FVM	TermoFluids	stagnant
Dang, [53]	CLSVoF / VoF	FVM	ANSYS Fluent	laminar
Nichita, [54]	CLSVoF	FVM	ANSYS Fluent	stagnant
Igaadi, [55]	CLSVoF	FDM	ANSYS Fluent	stagnant
Hua, [56]	FT	FVM	ANSYS Fluent	stagnant
Araújo, [4]	VoF	FVM	ANSYS Fluent	stagnant
Prasad, [61]	VoF	FVM	ANSYS Fluent	stagnant
Nagrath, [72]	LS	FEM	not mentioned	stagnant
Carlson, [73]	LS / VoF	QUICK/MUSCL	TransAT/ANSYS Fluent	laminar

flow problem becomes unsteady. Even in simulations of laminar Taylor bubble flow, the flow can be semi-turbulent at the wake region behind the bubble and therefore, if its motion is governed by a two-dimensional momentum equation, the results will be less accurate [64], [27]. The same opinion is illustrated by the authors in [32]. In this study, it is also mentioned that the predictions of numerical simulations must not only be compared against specific experimental results but also to be carefully checked for their physical consistency and restrictions.

In many engineering problems of rising Taylor bubbles, the liquid background flow is turbulent and unsteady vortices of different sizes are created which interact with each other and increase the complexity of the problem due to their chaotic behavior. Therefore, an accurate prediction requires a fully three-dimensional analysis and enough computer resources. For example, in the design and operation of a nuclear facility, it is important to understand the behavior of Taylor bubble flow in all flow regimes and all types of liquid background flow, including turbulent. The scientific gap of the simulations of Taylor bubbles in co/counter-current turbulent flow is a challenging topic and comprises the ambitious target of the current master thesis which has been carried out in collaboration with NRG.

2.4.2. Preliminary research questions

Each of the different multiphase flow regimes can be a thesis project in itself, therefore during the current master thesis work the main focus is on the way to successfully tackle high fidelity simulations of Taylor bubbles in co/counter-current turbulent flow, using the Basilisk software. To achieve reliable predictions, the following approach is followed and analyzed in the next chapters:

- Learning Basilisk. Basilisk is an open-source flow solver that employs the Volume of Fluid approach for the modeling of two-phase flow [91]. One of the main features of Basilisk is the fact that it can perform dynamically local grid refinement so it has the potential to capture accurately the gas-liquid interface.

- Identification and development of several simple test cases, for example in the dam break problem or in a rising bubble in a liquid column, to be simulated with Basilisk and to be post-processed.
- Validation of the Basilisk solver in the setting of single-phase turbulent pipe flow based on [92].
- Simulation of laminar Taylor bubble flow rising in stagnant liquid based on [4].
- Simulation of co/counter-current laminar Taylor bubble flow and validation against the experiments of [3] and [5].
- Development of a high-fidelity simulation of the Taylor bubble in co/counter-current turbulent flow and comparison against experimental findings of [3] and NRGs OpenFOAM Large Eddy Simulation (LES) results of [1] for co-current and against experiments of [5] for counter-current flow.

In the numerical analysis of Taylor bubbles in co/counter-current turbulent flow using Basilisk, some critical issues have to be taken into account and several corresponding sub-questions to be answered:

- By default the domain on which the equations are solved in Basilisk is a square box (or cube in 3D). How can the cylindrical domain and the embedded boundaries of the pipe flow problem be constructed? How can we simulate a fixed wall?
- The problem is transient due to strong shear stresses, which leads to a continuous and progressive reduction in the Taylor bubble's size (i.e. at the tail). What averaging strategy and what mesh size will be used?
- The small bubbles which are expected to break-up from the Taylor bubble may either merge again with the Taylor bubble or may be transported downstream of the flow. Is this bubble break-up physical and how can it be verified that our results will be realistic after the break-up?
- Preliminary simulations of Taylor bubble flow showed that the use of a linear interpolation scheme for the face-interpolated velocity leads to a very unstable free surface, producing significant artificial break-up. What can be done to avoid the instabilities of the free surface?
- Due to wall friction, the liquid flow loses kinetic energy and it is driven by a constant and spatially uniform pressure gradient. Therefore, even for high Reynolds number, laminarization of the liquid flow can be observed due to the thin liquid film between the Taylor bubble and the wall [93]. How can we keep the liquid flow turbulent?

Taking the above into consideration, we come up to the main research question:
What simulation strategy can be developed in Basilisk to accurately reproduce the motion of an individual Taylor bubble in turbulent co/counter-current background liquid flow?

3

Model and methods

3.1. Why Basilisk?

The main difficulty in the simulation of Taylor bubble flows is to capture accurately the changes in the shape of the gas-liquid interface. To achieve this, Basilisk software has been used. Basilisk is open-source software for the solution of partial differential equations describing fluid flow on adaptive Cartesian meshes and is designed to replace Gerris [94], [91].

The big advantage of Basilisk is the capability of local refinement of cells adaptively in time that allows capturing certain features in the flow with high precision while leaving other regions relatively unrefined. Such an approach may be proven to be very useful for multi-scale problems such as two-phase flow where the interface can be captured sharply in high resolution. Therefore, in the case of Taylor bubble flow, it can be used with very high mesh resolution near the bubble's interface and the wall while elsewhere the grid is allowed to be much coarser which leads to significantly less CPU time. In each time step, the mesh is adapted based on a user-defined tolerance which is defined as the maximum accepted discretization error for each scalar field (e.g. void fraction or/and velocity components). The built-in adaptive function checks each scalar field for the discretization error in each time step and refines the grid if the error exceeds at least one of the given tolerance values of each field. The underlying data structure is allowed only in a quadtree/octree approach and allows fast solution procedures since in these types of grids the resolution can vary within the spatial domain.

The base of quadtree (in two-dimensions) or octree (in three-dimensions) grids in Basilisk is the multi-resolution grid structure, called multigrid. Starting from the domain which is initially considered as a single cell, the idea of multi-resolution grid forms when one or more levels of refinement are added. The extra capability of tree-based grids is that they allow higher resolution along time only in the areas in which the user desires. The concept of the octree is based on parents' and children's cells. Higher levels are called the children of the cell located at one lower level which is called parent cell. Each children cell having half mesh size of the parent cell in each direction or vice versa, each parent cell is divided into 2 cells in each direction. Therefore, the idea is the 2-fold refinement of cells in each spatial direction. Based on this idea, the user can choose to refine dynamically some cells up to a specific level while leaving other cells unchanged. This idea is illustrated with an example in figures 3.1, 3.2 in [95].

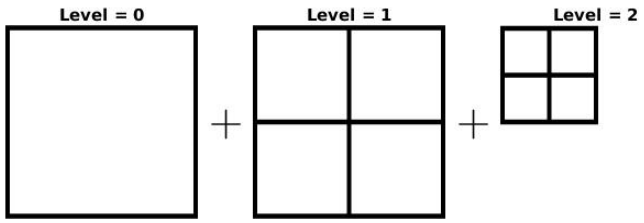

Figure 3.1: The cells within a simple Tree grid as illustrated in [95].

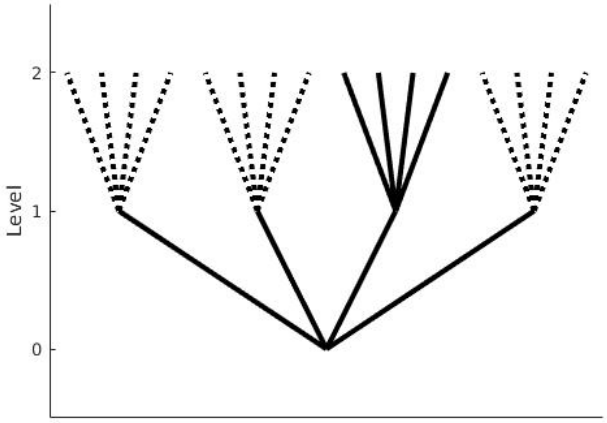

Figure 3.2: Conceptual view of the tree grid from the example above as shown in [95].

3.2. Numerical modeling of multiphase flows in Basilisk

Basilisk is a flow solver that employs a conservative, non-diffusive, geometric VoF scheme for the modeling of two-phase flows as illustrated in [96], [97]. The treatment of the interface is implemented with a piecewise continuous interface representation. In each iteration, reconstruction of the interface is performed by computing the outward normal vector n and slope a. An approximation of the interface normal using the Mixed-Youngs-Centered scheme [98]. The computation of the void fraction is performed by checking the sign of the component of velocity normal to the interface u_n in each face of grid cells and the index of the corresponding upwind cell as indicated in figure 3.3, [99]. Moreover, it is necessary to ensure the convergence condition by Courant Friedrichs Lewy by checking the CFL number in each time step.

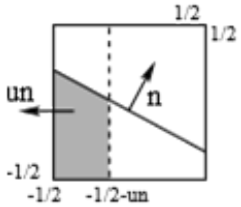

Figure 3.3: Volume fraction flux [100].

The governing equations that standard Basilisk solver uses for two-phase flows are already presented in 2.6-2.10. However, some modifications to the standard Basilisk N.S. solver have been made to improve its efficiency. The main differences that apply to all test cases are the following:

- First of all, when using the quadtree (or octree) approach all domains in Basilisk are by default square-shaped (or cube-shaped in three-dimensions) and this is often not desirable like in pipe flow simulations. Although there are built-in functions to overcome this problem in single-phase flows, they are not compatible with multi-phase flows with Message Passing Interface (MPI). Therefore, the construction of a non-square domain and its embedded boundary conditions has to be constructed manually in Basilisk for the simulation of a multi-phase flow like Taylor bubble flow when using multiple processors. The smoother damping of the velocity near the inside walls is achieved with an extra damping term that is added to to the right-hand side of the N.S. equations of 2.10 only for cells satisfying the embedded condition and only in the desired directions. The extra damping term h is computed using the direct volume penalization method as illustrated in [101], and has the following form:

$$\mathbf{h} = -\frac{H(\mathbf{x}) \cdot \mathbf{u}}{\tau} \tag{3.1}$$

, where $\tau << \Delta t$ the time scale of velocity damping and $H(\mathbf{x})$ a masking function which is unity for cells inside the solid wall and zero outside. The implicit damping in the desired direction is achieved by introducing an anisotropic damping parameter vector field which allows to damping only in one direction. For example, in case that it is desired to mimic a slip wall the velocity should be damped only in one direction. The effect of this modification will become visible in section 4.2.2 where it is compared against the standard Basilisk N.S. solver for which only explicit damping of velocity near the wall can be applied with post-processing.

- The momentum equation is solved by selecting the appropriate Runge-Kutta (RK) scheme from the Butcher tableau following a more general PISO algorithm (Pressure-Implicit with Splitting of Operators) which solves two iterations in implicit RK stages and one iteration for the explicit as illustrated in [102] while the standard Basilisk solver is using a two-point approach with upwinding as presented in [103].

- To define the dynamic viscosity at the interface, a harmonic mixing has been used instead of using the averaging procedure described by 2.7:

$$\mu = \frac{1}{\frac{f}{\mu_l} + \frac{(1-f)}{\mu_g}} \tag{3.2}$$

- Another amendment within the N.S. solver regards fact the full discretization of the diffusion term. This means that the second part of the deformation tensor $\mathbf{D} = \frac{1}{2}[\nabla\mathbf{u} + (\nabla\mathbf{u})^T]$ is not assumed to be zero, even though the velocity field should be divergence-free.

All in all, the developed Basilisk code is not the same for each test case. Except for the amendments to the standard Basilisk solver that already mentioned, all Basilisk codes differ each other in several other parameters (e.g. selection of the spatial and temporal discretization schemes). The crucial changes that have been made in the developed code of each validation case are mentioned and justified in the relevant section separately.

4

Validation of Basilisk code

As mentioned in the previous chapters, the current study is heading for the implementation of a Direct Numerical Simulation (DNS) strategy which can accurately reproduce the motion of an individual Taylor bubble in a turbulent co/counter-current background liquid flow using a code developed in Basilisk. Before beeing able to go towards a fully DNS approach, the Basilisk code is firstly validated for several cases. In the beginning, Basilisk code is tested in the setting of a circular bubble rising in a liquid rectangular column against the simulation data published by three independent research groups as presented in [2]. The same simulation setup is also implemented in OpenFOAM and the results are compared with Basilisk in terms of computational cost and code's efficiency. Next, simulations in the limits of laminar Taylor bubble flow in an initially stagnant liquid are performed in Basilisk and the predictions are compared with [4, ANSYS] and [1, figure 4, OpenFOAM] for different combinations of Eötvös and Morton numbers both in two and three directions. As a third step, the code is validated in the turbulent co-current Taylor bubble flow against the results of [1, figure 4, OpenFOAM] using the experimental setting of [3]. All these validation cases demonstrate that the developed Basilisk code produces results that are consistent with the published simulation data that was found in the literature. The effects of the amendments to the standard Basilisk N.S. solver that were already described in chapter 3 are visible in the following sections together with the extra modifications that are applied in each validation case separately.

4.1. Laminar bubble flow

The first case which is performed in Basilisk regards the simulation of a two-dimensional bubble which is released in a rectangular box and raises under the influence of buoyancy while undergoing shape deformation. To determine if Basilisk solves the posed problem correctly, the predictions are compared with the numerical results in two different configurations produced by three independent research groups as illustrated in [2]. Each research group implemented a separate computational study and utilized only one processor per simulation. The benchmark data is provided in ASCII text files and is available in [104].

Since there are no exact solutions available for this problem, the authors in [2] compare the results from the three institutes both quantitatively and visually. The necessity for quantitative comparisons for the validation of the mathematical modeling comes from the fact that different codes with identical problem formulations do not often produce identical results, such as in figure 4.1 which illustrates the resulting shape of the bubble for the second configuration after three simulation seconds using different software. It can be easily observed that all codes give different final shapes and therefore, due to the absence of an analytical solution, it is hard to judge which code is closer to reality. Thus, the visualization of the shape of the bubble may illustrate an indicator but cannot be considered as the only criterion for drawing conclusions.

For the reasons mentioned above, three different benchmark quantities are defined in [2] which describe both direct and indirect topological parameters: center of mass, mean rise velocity and circularity. In the current study, only the first two benchmark quantities are measured in Basilisk.

In particular, the position of center of mass of the bubble is given for each coordinate from the

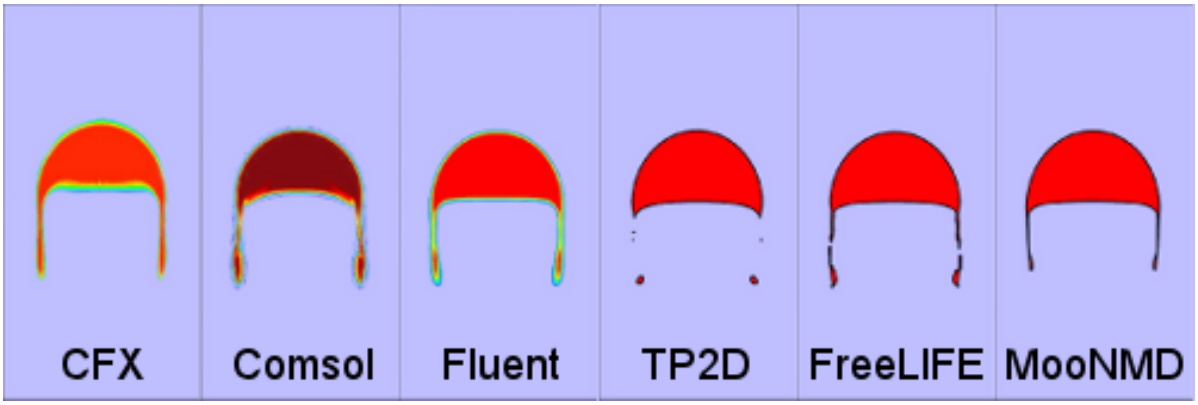

Figure 4.1: Numerical simulations of a two-dimensional rising bubble for six different codes with identical problem formulations as shown in [2]. The simulations regard case 2 of the table 4.1.

formula:

$$\mathbf{x_c} = (x_c, y_c) = \frac{\int_{\Omega_2} \mathbf{x} dx}{\int_{\Omega_2} 1 dx}, \tag{4.1}$$

where Ω_2 illustrates the area of the bubble in two-dimensions.

The mean rise velocity is measured as the moving velocity of the center of the bubble in each time step and is defined as:

$$\mathbf{u_c} = \frac{\int_{\Omega_2} \mathbf{u} dx}{\int_{\Omega_2} 1 dx} \tag{4.2}$$

The first configuration has small density and viscosity ratios whereas the second case has big density and viscosity ratios. The choice of physical properties and important dimensionless numbers for the two cases are taken identical to those from [2] and are indicated in table 4.1. Except density and viscosity ratios, Eötvös (Eo) number as defined in 2.3 and therefore, surface tension as well are the quantities that are changing from first to second configuration. On the contrary, the Reynolds number remains constant at laminar level in both cases.

Table 4.1: Physical parameters and important dimensionless numbers identical to [2].

Test case	ρ_1	ρ_2	μ_1	μ_2	g	σ	Re	Eo	ρ_1/ρ_2	μ_1/μ_2
1	1000	100	10	1	0.98	24.5	35	10	10	10
2	1000	1	10	0.1	0.98	1.96	35	125	1000	100

The governing equations for this two-phase problem are the Navier-Stokes equations together with mass conservation for incompressible flows (equations 2.9, 2.10). Surface tension effects are also taken into account at the interface between the liquid and the gas so it is necessary to use an accurate modeling method for interface tracking. Basilisk uses the VoF method for mathematical modeling as described in 2.1.2. The initial and boundary conditions are identical for both configurations and are taken from [2] and can be seen in figure 4.2. In particular, the initial bubble shape is a circle of diameter 0.5 meter and the center of the circle is initially placed at point [0.5 x 0.5] of a rectangular domain [1 x 2] square meters. The no-slip boundary condition is set at the top and the bottom of the boundaries and the free-slip boundary condition at vertical walls. All the above forms the boundary value problem in each configuration.

The initial refinement area for both cases in Basilisk has been chosen to be performed in a circle with radius one and a half- times the radius of the initially circular bubble which has diameter half. The initial refinement is executed up to the finest refinement level (i.e. maximum) so that the initial bubble shape is accurate.

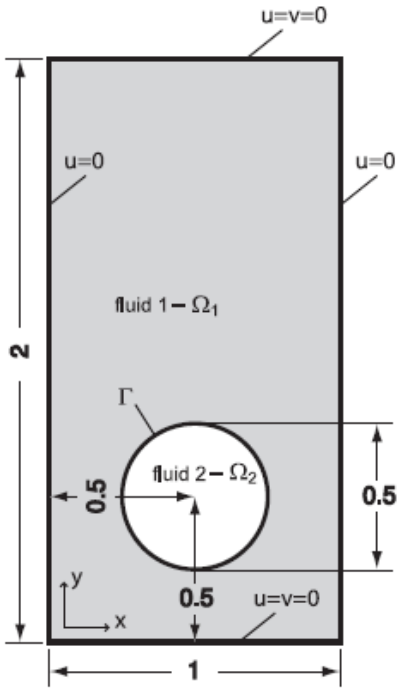

Figure 4.2: Initial position of the bubble and boundary conditions for both cases as illustrated in [2].

In the first place, the efficiency of the Basilisk code is compared against the results of [2] for the two configurations both qualitatively and quantitatively. In particular, the reference value of each benchmark quantity is considered as the average between the most accurate solutions (those coming from the most refined grids) of each research group. The qualitative comparison regards the shape of the bubble after three simulation seconds. Secondly, the two test cases are also simulated in OpenFOAM with identical setup with Basilisk and the two software are compared each other in terms of computational time needed for achieving a certain accuracy.

4.1.1. First test case

The first configuration simulates a rising bubble with small density and viscosity ratios for three seconds. Both density and viscosity of the liquid are ten times greater than those of gas. Eo number is also 10 because the surface tension is higher in this case.

The total number of simulations that are implemented in Basilisk for the first configuration is six. Three different pairs of minimum and maximum refinement level have been selected and each of them is combined with two different values of accepted velocity and void fraction tolerance. All possible combinations are compared with the average of the solutions coming from the most refined grids ($\frac{1}{h} = 320$) of each of the three research groups in [2]. The simulation results are checked both visually (i.e. identical shape in each snapshot) and quantitatively by checking the benchmark quantities of interest. The bubble is only moving on the vertical direction so the only the vertical component of position and velocity (direction opposite to gravity) varies in each time step. The deviations of the benchmark quantities from the reference solutions can be found in tables 4.12, 4.13 where l_1, l_2 and l_∞ error norms are calculated for each simulation which are defined as:

$$l_1: \quad ||e||_1 = \frac{\sum_{i=1} |q_{i,ref} - q_i|}{\sum_{i=1} |q_{i,ref}|} \tag{4.3}$$

$$l_2: \quad ||e||_2 = \left(\frac{\sum_{i=1} |q_{i,ref} - q_i|^2}{\sum_{i=1} |q_{i,ref}|^2} \right)^{\frac{1}{2}} \tag{4.4}$$

$$l_\infty: \quad ||e||_\infty = \frac{\max_i |q_{i,ref} - q_i|}{\max_i |q_{i,ref}|} \tag{4.5}$$

Regarding the final shape after three seconds, the bubble ends up with an ellipsoidal regime which is in agreement not only with the three numerical results in [2] but also with the experiments implemented in [105]. The shape agreement is tested separately for each simulation. No break up appears since the interfacial force is high due to strong surface tension.

The first simulation is performed for minimum refinement level 5 and maximum refinement level 7. Although the position of the center of the bubble is captured pretty well, an overestimation of the velocity of the centre of the bubble is observed as well as a significant difference in the final shape at $t = 3$. Two possible possibilities are analyzed for minimizing the deviation from the reference solution: Increasing the minimum or/and the maximum level of refinement or/and increasing the velocity and void fraction tolerance which is defined as the maximum accepted discretization error for each scalar field respectively.

The latter proposal is simulated firstly where there is an increase of one level of magnitude in the tolerance values of both velocity-components and gas fraction (from 0.01 to 0.001). The minimum and maximum refinement level was kept constant. The plots of the benchmark quantities are indicated in figures 4.3a, 4.3b. Surprisingly, the simulation with a higher tolerance value seems to be slightly closer to the reference solution for all error norms. Although the difference between the two simulations can be considered negligible (same values up to third decimal), an explanation for that is that our reference solution came from an average of the best solutions among numerical results and not from an analytical solution. On the other hand, concerning velocity, the convergence is better for the simulation with a smaller tolerance. Moreover, the final shape of the bubble is also more accurate with smaller tolerance as shown in figures 4.4a, 4.4b.

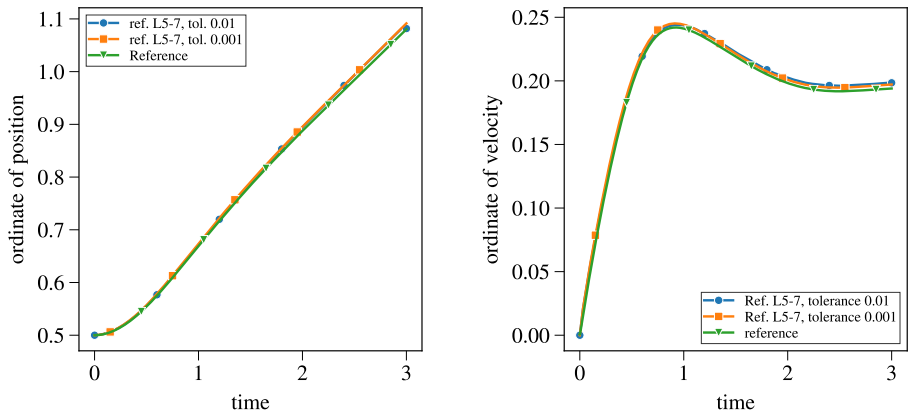

(a) (b)

Figure 4.3: Case 1: ordinate of position (4.3a) and velocity (4.3b) of the centre of the bubble for minimum and maximum levels of refinement 5 and 7 and different tolerances.

An alternative for the previous proposal is to increase the maximum level of refinement from 7 to 12. However, in this case, and for tolerance values 0.01, it has been observed from the visualization of the output of the simulation that the maximum level of refinement is never achieved and the higher level of refinement is 9 (figure 4.11). Two simulations are executed for the same values of minimum and maximum levels and different tolerance (0.01 and 0.001 respectively) are executed as before. The results for the evolution of the bubble's position and velocity are illustrated in figures 4.5a, 4.5b while the final shape and position of the bubble are indicated at 4.6a, 4.6b.

The last pair of simulations for the first configuration is implemented for maximum level of refinement 9 while the minimum refinement level is increased from 5 to 7 to get even better convergence even for tolerance 0.01 (for both velocity components and gas fraction). Indeed, the predictions seem more accurate than the previous simulations both visually (i.e. identical final shape 4.8a, 4.8b) and quantitatively by checking the benchmark quantities (figures 4.7a, 4.7b). This pair of simulations is more accurate and has less computational cost than the previous pair (level 5-12)

Comparison of the bubble's position among the three different choices of levels of refinement and their convergence to the reference solution is indicated in figures 4.9a, 4.9b. Similarly, the convergence

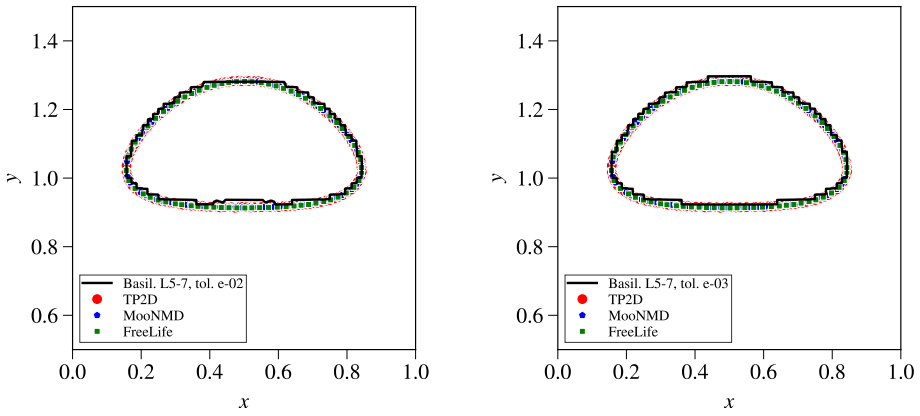

(a) (b)

Figure 4.4: Case 1: Final shape (at $t = 3$) for minimum and maximum levels of refinement 5 and 7 and tolerance 0.01 (4.4a) and 0.001 (4.4b) correspondingly.

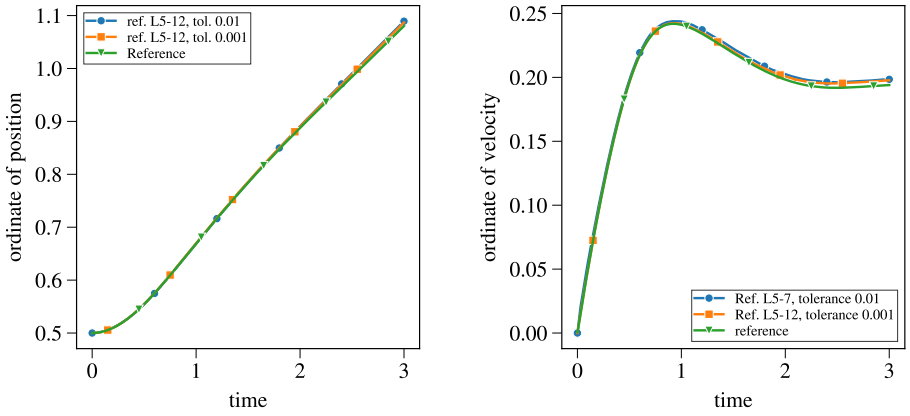

(a) (b)

Figure 4.5: Case 1: Ordinate of position (4.5a) and velocity (4.5b) of the centre of the bubble for minimum and maximum levels of refinement 5 and 12 correspondigly and different tolerances.

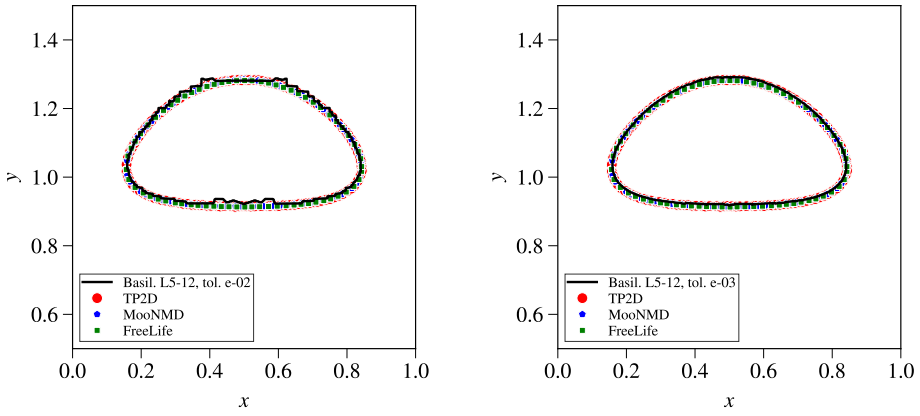

(a) (b)

Figure 4.6: Case 1: Final shape (at $t = 3$) for minimum and maximum levels of refinement 5 and 12 and tolerance 0.01 (4.6a) and 0.001 (4.6b) correspondingly.

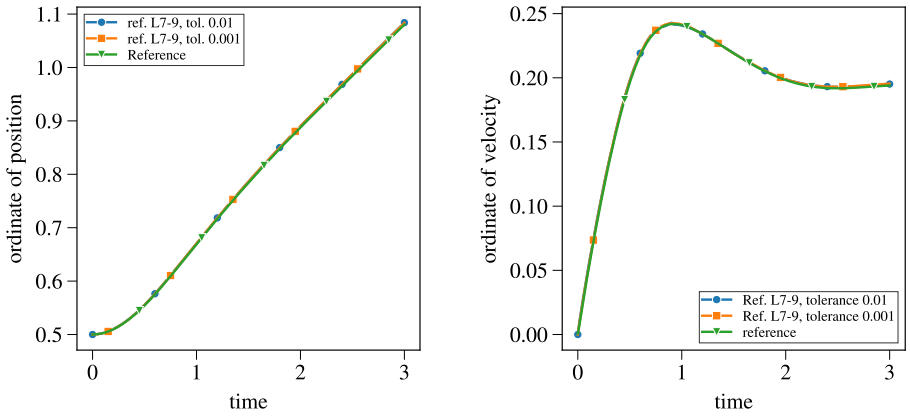

(a) (b)

Figure 4.7: Case 1: Ordinate of position (4.7a) and velocity (4.7b) of the centre of the bubble for minimum and maximum levels of refinement 7 and 9 correspondigly and different tolerances.

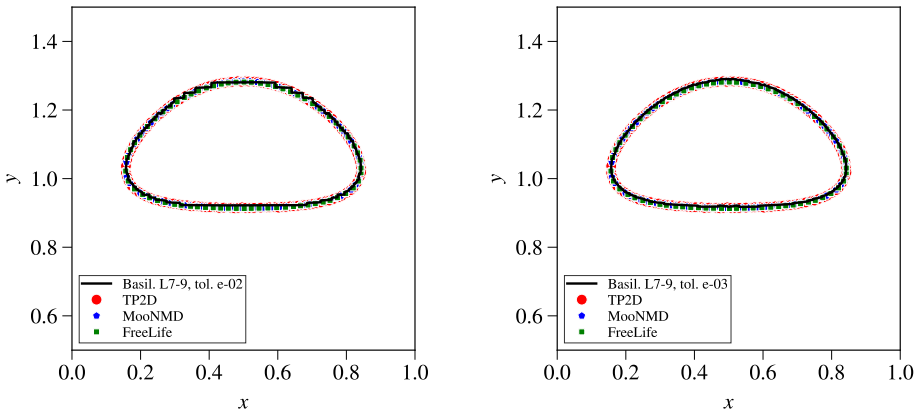

(a) (b)

Figure 4.8: Case 1: Final shape (at $t = 3$) for minimum and maximum levels of refinement 7 and 9 and tolerance 0.01 (4.8a) and 0.001 (4.8b) correspondingly.

to the reference solution of bubble velocity for all simulations is illustrated in 4.10a, 4.10b.

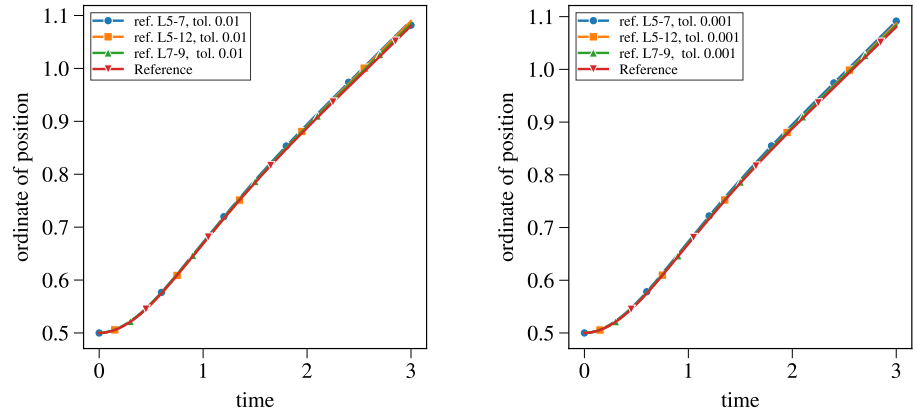

(a) (b)

Figure 4.9: Test Case 1: Ordinate of position of the centre of the bubble over time for three different pairs of minimum and maximum level of refinement and the reference solution for tolerance of velocity and void fraction 0.01 (4.9a) and 0.001 (4.9b) correspondingly.

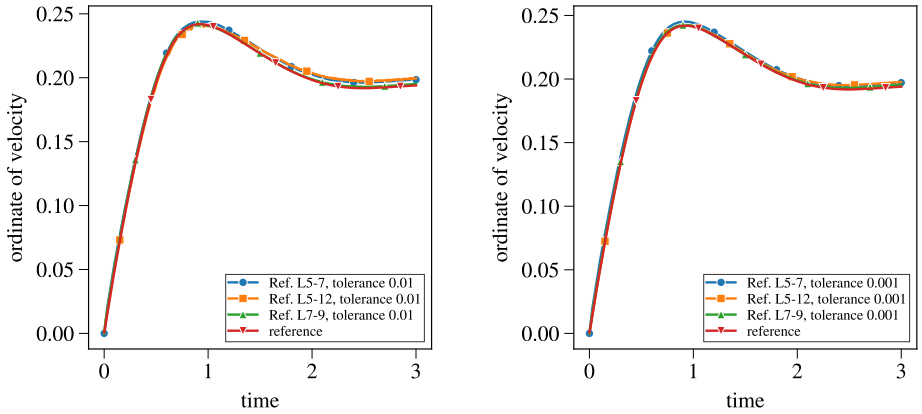

(a) (b)

Figure 4.10: Case 1: Ordinate of velocity of the centre of the bubble over time for three different pairs of minimum and maximum level of refinement and the reference solution for tolerance of velocity and void fraction 0.01 (4.10a) and 0.001 (4.10b) correspondingly.

Figure 4.11 illustrates the refinement levels in all cells of the domain at the final time and for all simulations. This is an important indicator which shows the cells in which the values of void fraction and velocity exceeds the tolerance value in the final time step. It is easily observed that maximum refinement should be at least 9 in combination with low tolerance.

Overall, the error norms of the benchmark quantities can be seen in 4.12. The maximum velocity, the real-time it occured during each simulation, the final ordinate of the position of the center of the bubble as well as the CPU time and the number of iterations are shown in 4.13. Basilisk shows very good quantitative (position and velocity of the center of bubble) and qualitative (shape) matching for the first configuration with the numerical results produced by the three research groups. Due to the capability of dynamically local grid refinement, much less numerical effort is required to attain a certain accuracy. The best option for the levels of refinement seems to be 7 for the minimum and 9 for the maximum.

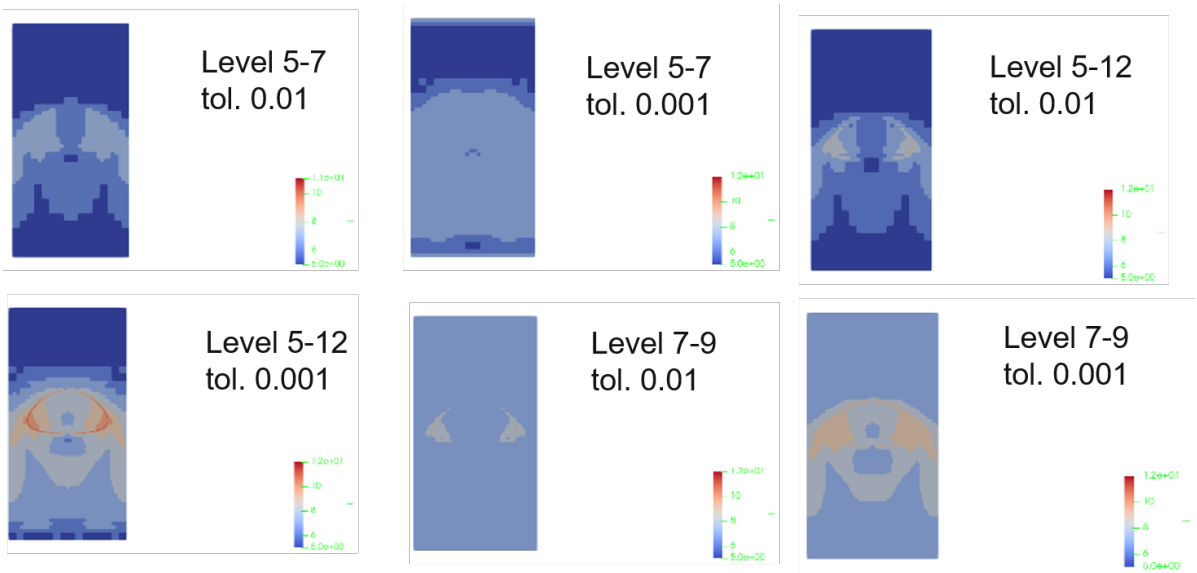

Figure 4.11: Case 1: Levels of refinement of each cell of the domain at the final position (t=3) in all six simulations in Basilisk. The levels vary from 5 (dark blue) up to 12 (dark red).

Error Norms	Ref.L5-7, tol=0.01	Ref.L5-7, tol=0.001	Ref.L5-12, tol=0.01	Ref.L5-12, tol=0.001	Ref.L7-9, tol=0.01	Ref.L7-9, tol=0.001
$\|\|e\|\|_1$ pos.	0.006309	0.007865	0.003259	0.002754	0.002757	0.002667
$\|\|e\|\|_1$ veloc.	0.018286	0.017541	0.018286	0.008224	0.00476	0.004549
$\|\|e\|\|_2$ pos.	0.007352	0.008549	0.004843	0.003624	0.002997	0.002971
$\|\|e\|\|_2$ veloc.	0.018499	0.018206	0.018499	0.010303	0.005956	0.005136
$\|\|e\|\|_\infty$ pos.	0.010261	0.010348	0.008458	0.00613	0.003867	0.003989
$\|\|e\|\|_\infty$ vel.	0.023957	0.028173	0.023957	0.015409	0.012094	0.006885

Figure 4.12: Case 1: Error norms of ordinate of position and velocity of centre of bubble for six simulations which are compared against the reference solution.

	Ref.L5-7, tol=0.01	Ref.L5-7, tol=0.001	Ref.L5-12, tol=0.01	Ref.L5-12, tol=0.001	Ref.L7-9, tol=0.01	Ref.L7-9, tol=0.001	Reference 1/h = 320
$V_{c,max}$	0.243957	0.24520	0.241965	0.242421	0.24295	0.242528	0.2419 ± 0.002
$t_{Vc=Vc,max}$	0.95	0.9	0.91610	0.92448	0.90702	0.90974	0.92 ± 0.02
$y_{c,(t=3)}$	1.09185	1.09153	1.089406	1.086926	1.08390	1.08354	1.081 ± 0.003
CPU	11.9	12.2	614.7	109632	528.9	1941	TP2D=126373 FreeLIFE= 108846 MooNMD = 180819
time steps	610	610	11452	104049	3895	4629	TP2D=15360 FreeLIFE= 960 MooNMD= 6000

Figure 4.13: Case 1: Comparison of benchmark quantities and computational time against reference solution.

4.1.2. Second test case

The second configuration is more challenging and simulates a rising bubble with bigger density and viscosity ratios for three time units. The density of the liquid is a thousand times greater than the density of gas while the viscosity ratio is a hundred. Eo number is 125 because the surface tension is lower in this case. The final regime of the bubble is expected to be between the skirted and dimpled ellipsoidal-cap with a possible break up phenomenon due to the weak surface tension and the flow properties.

Similarly with the first case, three pairs of simulations with different minimum and maximum levels of refinements are chosen. Each pair has one simulation with one order of magnitude less tolerance for both void fraction and velocity. Again, the same benchmark quantities have been selected for the quantitative comparison. All simulations are compared with the average of the solutions coming from the most fine grids ($\frac{1}{h} = 640$) of each of the three research groups in [2]. However, the results of the three research groups agree very well for the computed benchmark quantities only up to $t = 1.75 - 2.0s$. After this time, although all codes predict a similar shape for the main bulk of the bubble, there is no agreement concerning the thin filamentary regions. Therefore, there is no reference solution for the last time unit of this simulation.

In the first place, two simulations with minimum 5 and maximum of 7 levels of refinement are implemented for tolerance 0.01 and 0.001. However, the velocity plot shows some non-physical fluctuations which are not present in the reference solution. The final shape is also not captured well. The results are shown in figures 4.14a, 4.14b for the ordinate of position and velocity of the center of the bubble and in 4.15a, 4.15b for the final shape. The simulation with tolerance 0.001 captures better the final shape at the nose of the bubble. There is no break-up phenomenon like the reference solution 3 (MoonNMD code) and the results from the commercial codes CFX and Fluent indicated in figure 4.1.

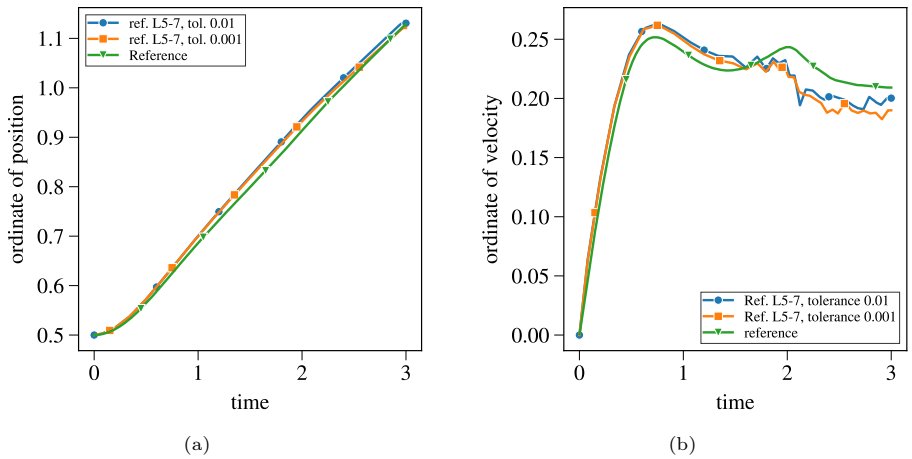

Figure 4.14: Case 2: Ordinate of position (4.14a) and velocity (4.14b) of the centre of the bubble for minimum and maximum levels of refinement 5 and 7 correspondigly and different tolerances.

Next, the maximum level of refinement is only increased to 11 while the minimum remains at 5. Again, the two simulations are executed with the tolerances of both velocity and void fraction 0.01 and 0.001 respectively. The position and velocity plots for the two simulations are illustrated in figures 4.16a, 4.16b while the final shape at figures 4.17a, 4.17b. The results indicated that even with the increased maximum level of velocity, the final shape and position are not captured accurately.

Therefore, a decision for increasing the minimum level of refinement up to 6 was made and at the same time, the maximum level was set to 10 to keep CPU time low. The figures of ordinate of position and velocity of the bubble are indicated in 4.18a, 4.18b, and the final shape at 4.19a, 4.19b. All benchmark quantities seem to be accurately captured and with less computational costs for the second pair of simulations. Even for this choice of levels, no break-up is observed at the trailing edges of the bubble but only a reduction in the thickness at the long trailing filaments. Possible explanations for this are the way that the treatment of the interface in the advection equation is performed and the calculation of interface mean curvature k which involves the second partial derivative of height functions

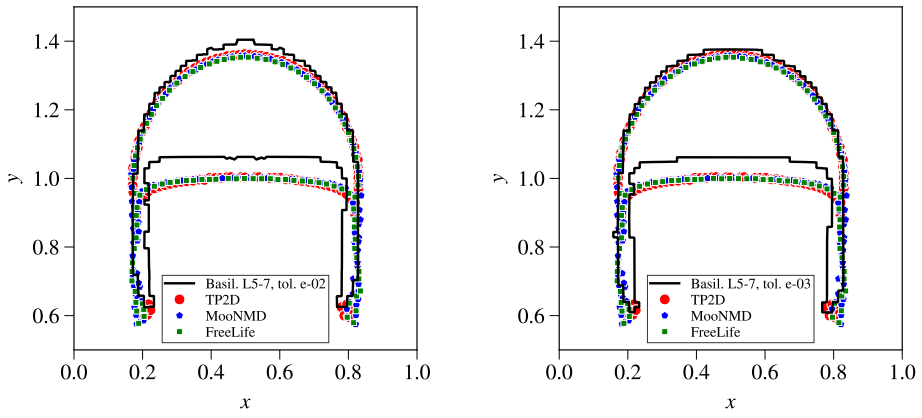

(a) (b)

Figure 4.15: Case 2: Final shape (at $t = 3$) for minimum and maximum levels of refinement 5 and 7 and tolerance 0.01 (4.15a) and 0.001 (4.15b) correspondingly.

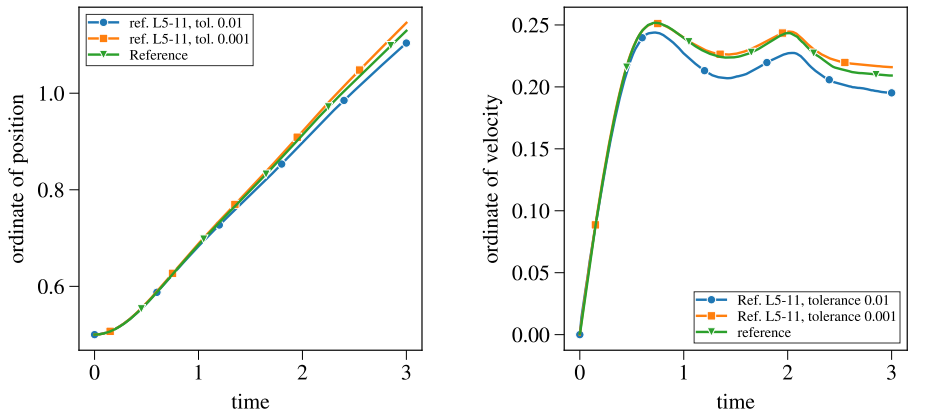

(a) (b)

Figure 4.16: Case 2: Ordinate of position (4.16a) and velocity (4.16b) of the centre of the bubble for minimum and maximum levels of refinement 5 and 11 correspondigly and different tolerances.

(distance between cell-center and interface) [106], [107].

The refinement levels for all Basilisk simulations at the final snapshot (t=3) are indicated in figure 4.20. It is obvious that for this configuration simulations with minimum level of refinement 5 do not capture the problem accurately. Similarly, in simulations where the maximum refinement level is only 7, the mesh is refined up to this level almost everywhere around the bubble.

The comparison of all Basilisk simulations is illustrated in figures 4.21a,4.21b for position and 4.22a, 4.22b velocity. Moreover, the error norms of the ordinate of position and velocity of the center of the bubble are shown in 4.23 while in 4.24, the values of the two local maximum velocities (and the time they occur), the final position and the CPU time for the simulation are indicated. It can be easily observed that the choice of refinement level 6-10 with tolerance 0.001 comprises the best option.

The best option in Basilisk (levels 6-10, tolerance 0.001) match all benchmark quantities and predicts similar bubble shape with the reference solutions. However, all codes do not match each other in the thin filamentary regions after $t = 1.75s$ as was already observed in figure 4.1. Although two research groups (TP2D and FreeLIFE) capture a break up at the tail, they do not agree in its timing while the third research group (MoonNMD code) does not show a break-up within $3s$ similar to what is predicted in Basilisk. A possible explanation is the way of the treatment of interface in advection equation. Figures 4.25a-4.25h indicate the evolution of the interface along time in Basilisk and TP2D code from [2].

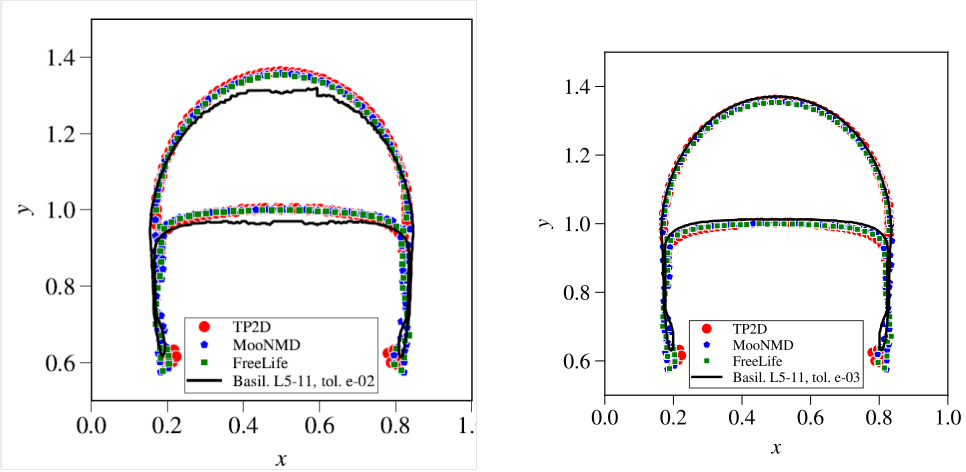

(a) (b)

Figure 4.17: Case 2: Final shape (at $t = 3$) for minimum and maximum levels of refinement 5 and 11 and tolerance 0.01 (4.17a) and 0.001 (4.17b) correspondingly.

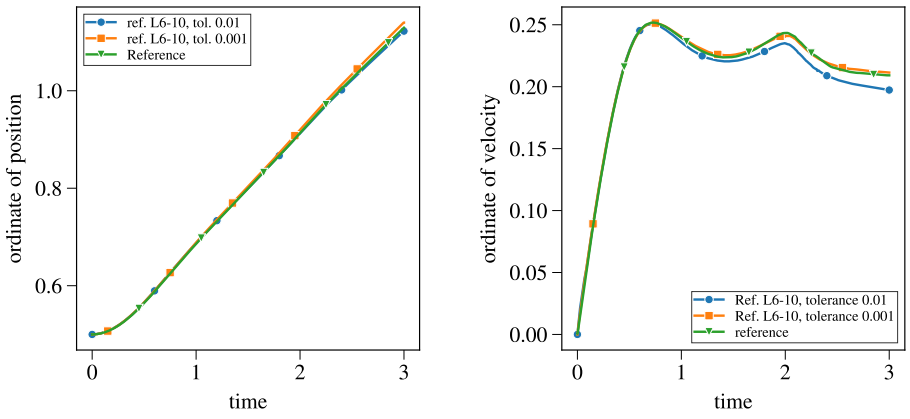

(a) (b)

Figure 4.18: Case 2: Ordinate of position (4.18a) and velocity (4.18b) of the centre of the bubble for minimum and maximum levels of refinement 6 and 10 correspondigly and different tolerances.

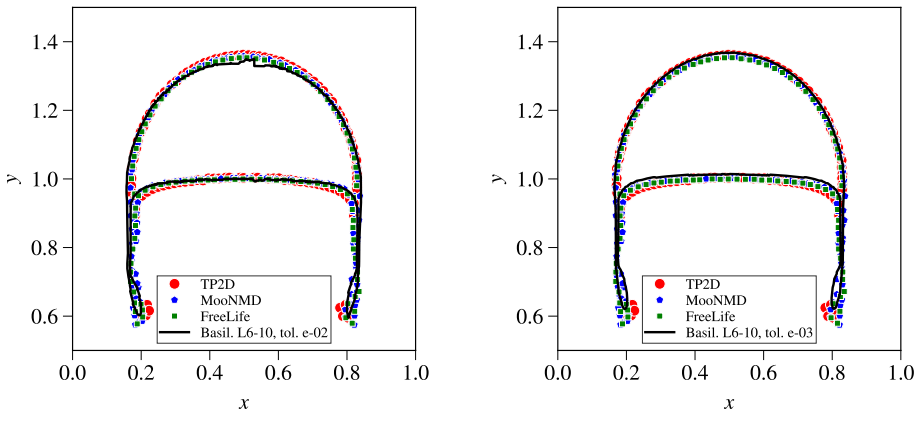

(a) (b)

Figure 4.19: Case 2: Final shape (at $t = 3$) for minimum and maximum levels of refinement 6 and 10 and tolerance 0.01 (4.19a) and 0.001 (4.19b) correspondingly.

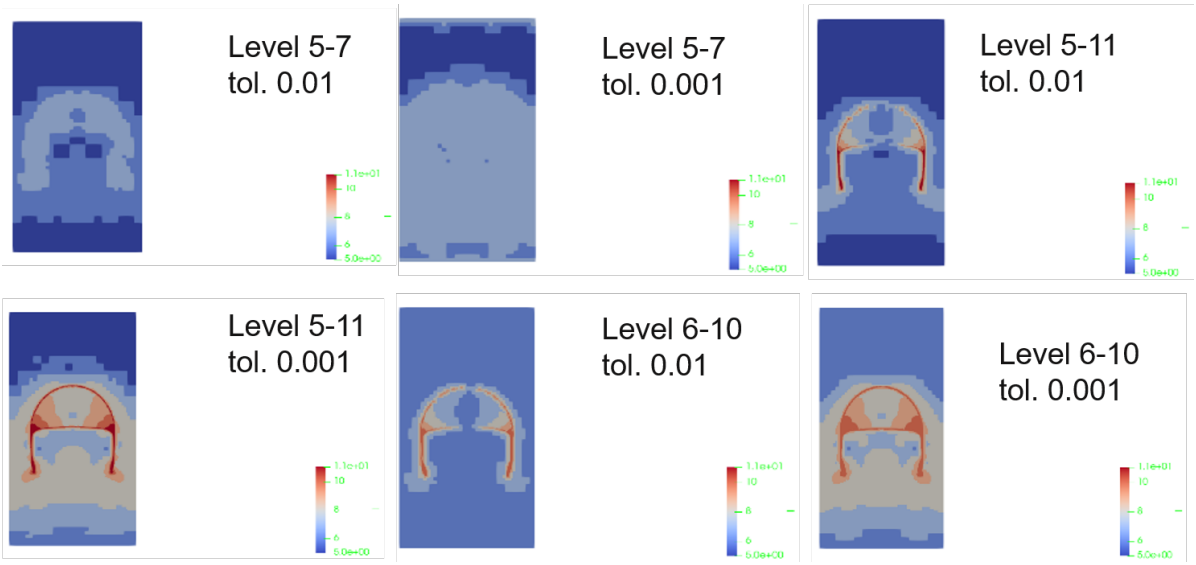

Figure 4.20: Case 2: Levels of refinement of each cell of the domain at the final position (t=3) and for all six simulations in Basilisk. The levels vary from 5 (dark blue) up to 11 (dark red).

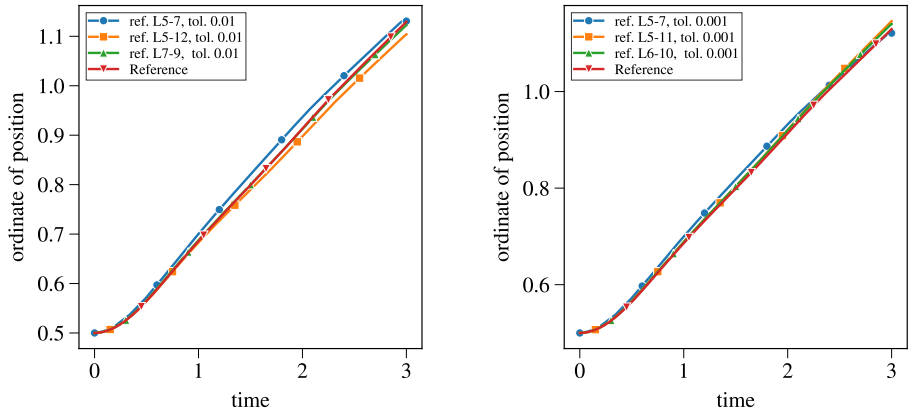

(a) (b)

Figure 4.21: Test Case 2: Ordinate of position of the centre of the bubble over time for three different pairs of minimum and maximum level of refinement and the reference solution for tolerance of velocity and void fraction 0.01 (4.21a) and 0.001 (4.21b) correspondingly.

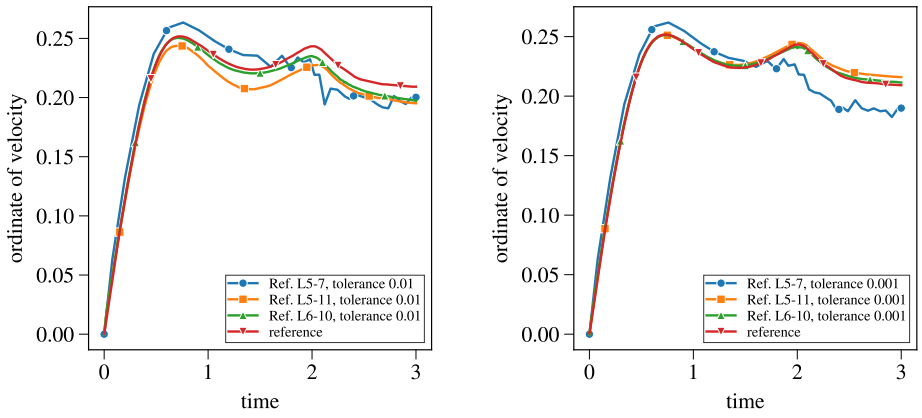

(a) (b)

Figure 4.22: Case 2: Ordinate of velocity of the centre of the bubble over time for three different pairs of minimum and maximum level of refinement and the reference solution for tolerance of velocity and void fraction 0.01 (4.22a) and 0.001 (4.22b) correspondingly.

Error Norms	Ref.L5-7, tol=0.01	Ref.L5-7, tol=0.001	Ref.L5-11, tol=0.01	Ref.L5-11, tol=0.001	Ref.L6-10, tol=0.01	Ref.L6-10, tol=0.001
$\|\|e\|\|_1$ pos.	0.01828	0.01408	0.01254	0.00798	0.00216	0.00606
$\|\|e\|\|_1$ veloc.	0.06371	0.06940	0.05307	0.0125462	0.02515	0.00624
$\|\|e\|\|_2$ pos.	0.0195	0.0158	0.01592	0.011728	0.00282	0.00708
$\|\|e\|\|_2$ - veloc.	0.0688	0.07786	0.05625	0.0164	0.02970	0.00701
$\|\|e\|\|_\infty$ pos.	0.02153	0.01814	0.02249	0.04179	0.00615	0.01006
$\|\|e\|\|_\infty$ vel.	0.17268	0.13055	0.0668	0.03424	0.04732	0.01153

Figure 4.23: Case 2: Error norms of ordinate of position and velocity of centre of bubble for six simulations which are compared against the reference solution.

	Ref.L5-7, tol=0.01	Ref.L5-7, tol=0.001	Ref.L5-11, tol=0.01	Ref.L5-11, tol=0.001	Ref.L6-10 tol=0.01	Ref.L6-10 tol=0.001	Reference 1/h = 640
$V_{c,max1}$	0.263576	0.26198	0.24390	0.25127	0.250511	0.251388	0.25 ± 0.01
$t_{Vc=max1}$	0.75714	0.75714	0.72307	0.72378	0.70775	0.736434	t =0.73 ±0.02
$V_{c,max2}$	0.23392	0.23115	0.2275	0.2447	0.2352	0.24157	0.242 ±0.03
$t_{Vc=max2}$	1.86193	1.86923	2.050	2.0223	1.9945	1.98449	t =2.0 ± 0.12
$y_{c,(t=3)}$	1.13069	1.121	1.1039	1.14557	1.1223	1.13985	1.13 ± 0.01
CPU	29.1	67.4	47489.7	279218	10807	48888.5	Not mentioned
time steps	348	356	10528	10951	3892	3945	Not mentioned

Figure 4.24: Case 2: Comparison of benchmark quantities and computational time against reference solution.

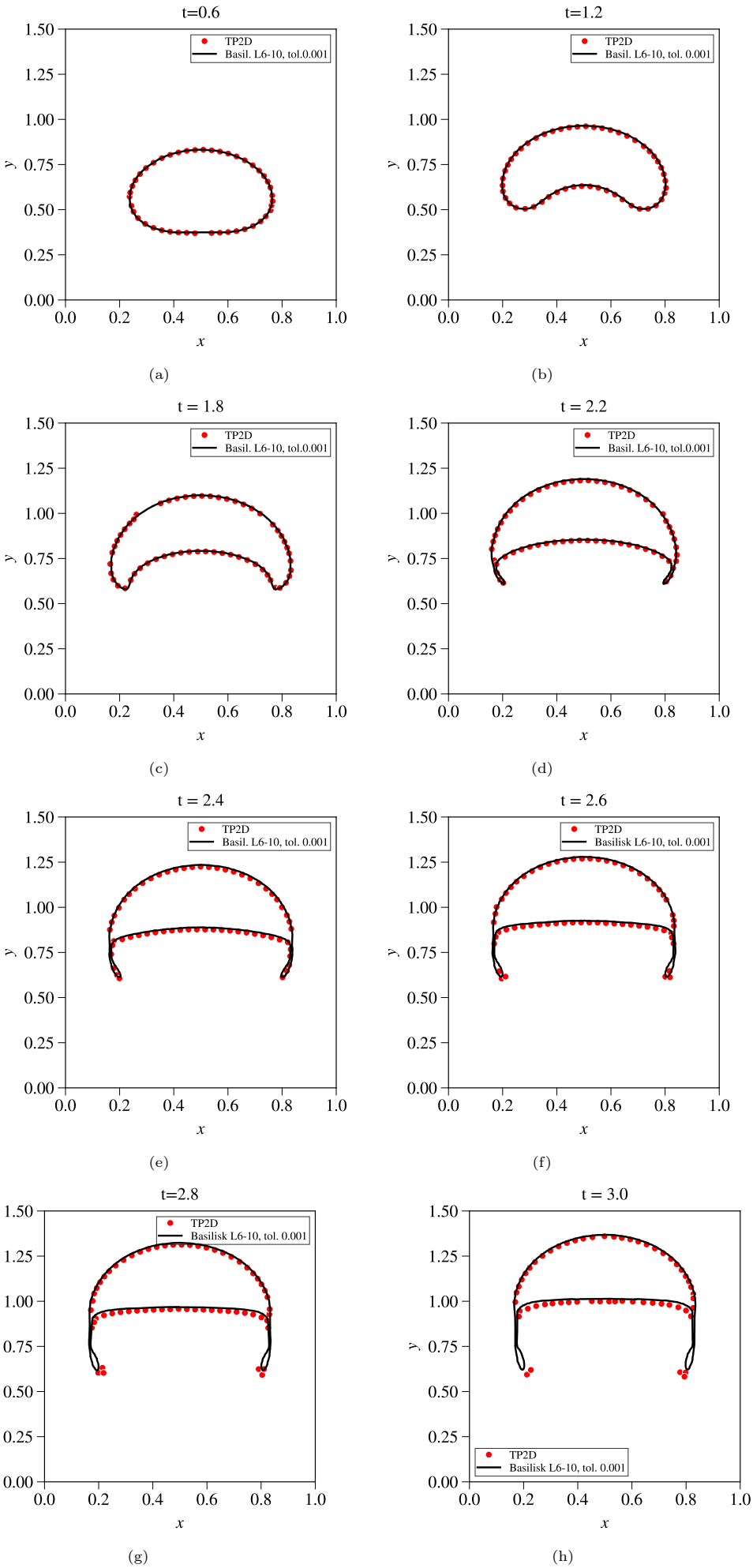

Figure 4.25: Case 2: Interface at different snapshots. Comparison between Basilisk and TP2D solver.

4.1.3. Basilisk vs OpenFOAM

Next, the performance of Basilisk code in the two-phase flow problem of the rising bubble in stagnant liquid is tested against OpenFOAM for both cases. For each case, six simulations with uniform meshes within the liquid tank have been performed with each software. In addition, due to the advantage of the adaptive grid with local refinement in Basilisk, four more simulations with varying resolution (maximum resolution near the interface) along time have been implemented in which in each time step the grid is adaptive within the cells where the value of interface change more than 0.001. The simulations with the most refined mesh of each software are used as reference solutions and therefore, the efficiency of each simulation of each software is tested in the sense of self-convergence. Moreover, both software is compared both to each other and against the predictions of the MooNMD code presented in [2].

All simulations in both Basilisk and OpenFOAM are using a cell-centered grid and the solvers are using the same configuration settings and schemes. In particular, diagonally implicit Runge-Kutta method of second-order has been used for temporal discretization and central spatial discretization scheme for both diffusive and convective terms of Navier-Stokes equations. In addition, fully discretization of the shear strain rate tensor (all three terms) has been concluded to give more accurate results in Basilisk. Moreover, $CFL < 0.1$ has been applied for preserving stability (especially for case 2) while 12 corrector steps have been used in the PISO algorithm for achieving high accuracy and keep the error always below 0.001 at the velocity-pressure calculation.

To make the differences between the different meshes and software visible, table 4.2 for the first and 4.3 for the second case have been created. These tables indicate the number of cells per dimension, the number of processors used, the accuracy of each simulation compared to the reference solution (mesh F of each software) by measuring the L1-norm of the two benchmark quantities (y and u_y), the total simulation time and the amount of computational time per processor per cell per time step.

Case 1

As mentioned in 4.1.1, the first configuration simulates a rising bubble with small density and viscosity ratios while the strong interfacial forces are keeping the gas-liquid interface consistent. The results of each simulation are checked from the reference solutions (mesh F) of each software both visually (final shape) and quantitatively by checking the evolution benchmark quantities (y and u_y).

Table 4.2 indicates the mesh used in each simulation and its data. In the first place, a direct comparison between simulations with the same uniform meshes (A, B, C, D, E, F) can be done between OpenFOAM and Basilisk. An important conclusion is that Basilisk shows better self-convergence to the reference solution (mesh F) in coarser meshes than OpenFOAM because the deviation in the ordinate of the position and velocity of the bubble is always smaller in Basilisk. In particular, as the mesh is becoming finer (after mesh C), the difference in absolute values between the two software becomes more significant, i.e. values in Basilisk are one order of magnitude smaller. Moreover, the order of magnitude of the computational time needed per processor per cell per time step remains small even for meshes with high resolution in Basilisk while in OpenFOAM, it increases after mesh D. These differences become even greater when non-uniform adaptive meshes are used in Basilisks simulations in which the mesh is refined as much as possible near the interface whereas everywhere else remains coarse (meshes E5, E6, E7, E8). Comparing to mesh E, the simulations with adaptive meshes last up to 8 times less since the degrees of freedom (DOF) are much less, while the deviation from the reference mesh F remains low.

The above quantitative conclusions become visible in figures 4.26 and 4.27. The bubble rising velocity and position converge faster in uniform meshes in Basilisk than in OpenFOAM while adaptive meshes show great accuracy (4.26b, 4.27b). Moreover, the velocity curve along time in Basilisk coincides with MooNMD identically.

Table 4.2: Simulation data for each mesh and software for case 1. The table illustrates the number of cells per dimension, the number of processors used, the L1-norm of the two benchmark quantities (y and u_y), the total simulation time and the amount of computational time per processor per cell per time step.

OpenFOAM

Mesh	Nx	Ny	Ncells	Nproc	$\|\|e_y\|\|_1$	$\|\|e_u\|\|_1$	Iter.	t_{sim}	t_{sim}* N_{proc}/N_{cells}/iter.
A	16	32	512	1	0.010053883	0.055258588	262	5	3.72734E-05
B	32	64	2048	1	0.00650898	0.041308687	472	36	3.72418E-05
C	64	128	8192	1	0.005091715	0.036623344	904	402	5.42835E-05
D	128	256	32768	2	0.004118119	0.030283293	1739	4044	0.000141936
E	256	512	131072	7	0.002626718	0.019796888	3364	10714	0.000170092
F (ref)	512	1024	524288	16	-	-	6449	60010	0.000283976

Basilisk

Mesh	Nx	Ny	Ncells	N_{proc}	$\|\|e_y\|\|_1$	$\|\|e_u\|\|_1$	Iter.	t_{sim}	t_{sim}* N_{proc}/N_{cells}/iter
A	16	32	512	1	0.0055113	0.0330930	216	6	5.67E-05
B	32	64	2048	1	0.0024737	0.0061449	433	31	3.55E-05
C	64	128	8192	1	0.001532	0.0030585	863	314	4.44E-05
D	128	256	32768	2	0.0006702	0.0014417	1784	2372	8.11E-05
E	256	512	131072	7	0.0001901	0.0004872	4614	4450	5.15E-05
F (ref)	512	1024	524288	16	-	-	13015	38500	9.02E-05
E5	32< Nx, Ny <512		~ 2K	2	0.0043992	0.0255144	4614	603.3	0.000119
E6	64< Nx, Ny <512		~3K	2	0.0018982	0.0128921	4614	1359	0.000163
E7	128< Nx, Ny <512		~9K	2	0.0009833	0.005348	4614	1929	8.89E-05
E8	256< Nx, Ny <512		~34K	2	0.000523	0.0016617	4614	7940	0.000101

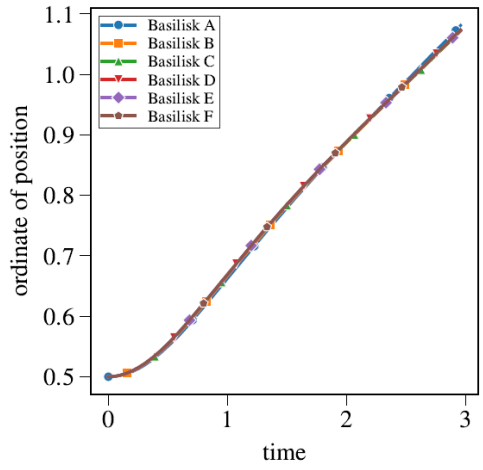

(a) Uniform meshes in Basilisk.

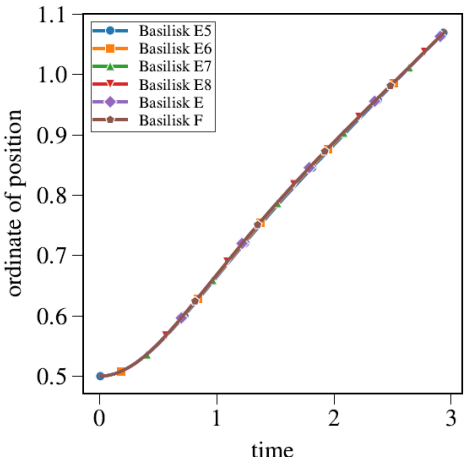

(b) Non-uniform adaptive meshes in Basilisk.

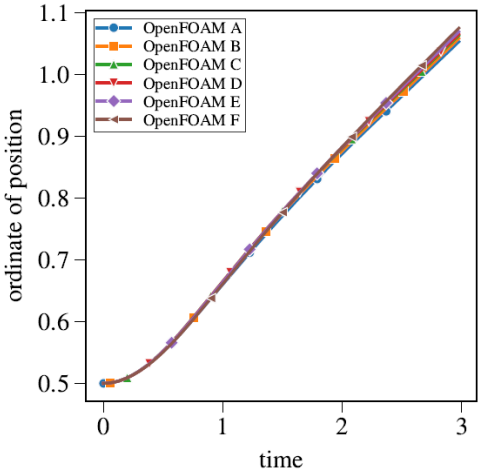

(c) Uniform meshes in OpenFOAM.

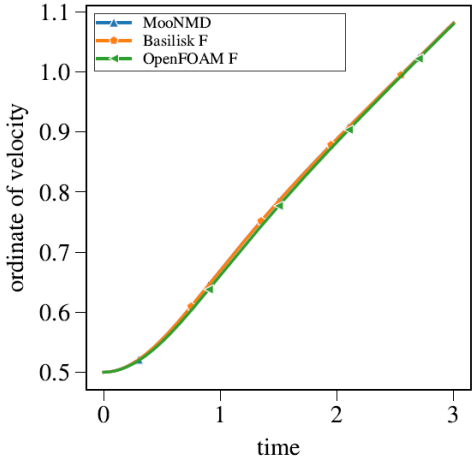

(d) Reference meshes in Basilisk, OpenFOAM, MooNMD.

Figure 4.26: Case 1: Ordinate of bubble's position along time from simulations with different meshes in different software.

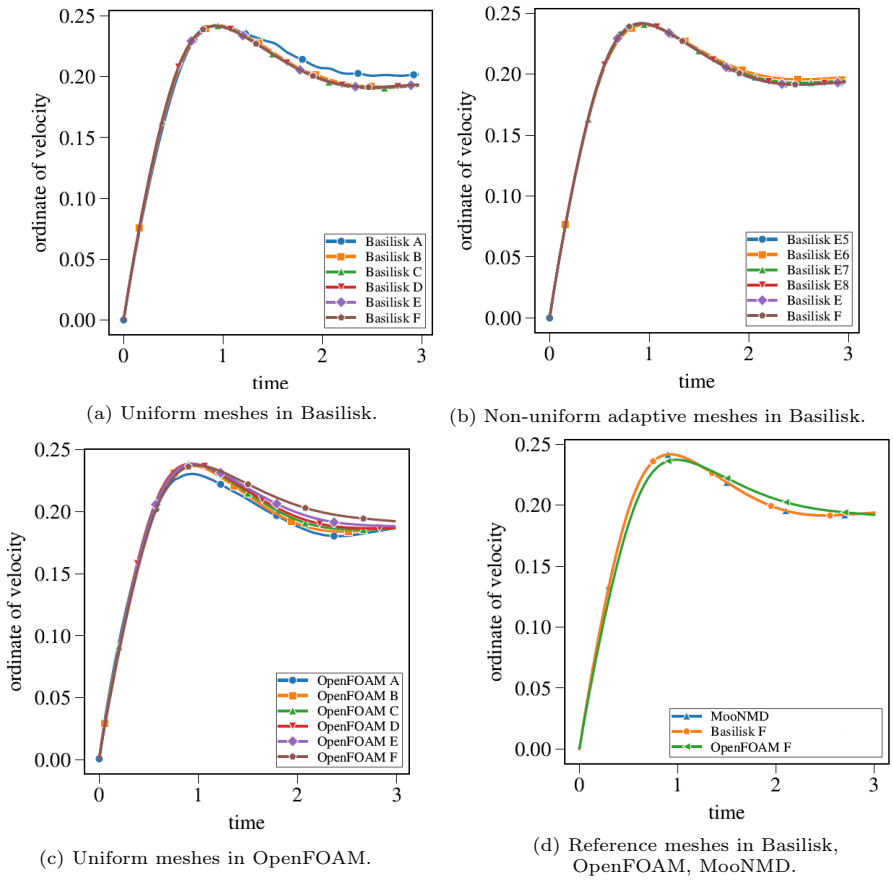

(a) Uniform meshes in Basilisk.

(b) Non-uniform adaptive meshes in Basilisk.

(c) Uniform meshes in OpenFOAM.

(d) Reference meshes in Basilisk, OpenFOAM, MooNMD.

Figure 4.27: Case 1: Ordinate of bubble's velocity along time from simulations with different meshes in different software.

Regarding the final shape, the bubble ends up with an ellipsoidal regime in all software. Figure 4.28 shows the resulting shape of simulations with uniform grids in OpenFOAM, uniform/ non-uniform adapted grids in Basilisk and the reference meshes in Basilisk, OpenFOAM, and MooNMD (as presented in [2]). Both Basilisk and OpenFOAM capture the final shape very accurately at both meshes E and F. Moreover, all adaptive non-uniform meshes with refinement around the interface in Basilisk achieve accurate shape even for a coarse grid elsewhere in the domain (mesh E5).

Case 2

As mentioned in section 4.1.2, the second configuration is more challenging and simulates a rising bubble with bigger density and viscosity ratios for three seconds. The final shape of the bubble is between the skirted and dimpled ellipsoidal-cap with a possible break up phenomenon at the tail.

Table 4.3 illustrates all the useful data of each simulation. Similarly to what was concluded for case one, Basilisk seems to show better convergence to the reference simulation (mesh F) for coarse grids (meshes A, B) for the two benchmark quantities (y and u_y). For finer meshes (C, D, E) though, the differences in accuracy are negligible. However, in Basilisk, the gain of computational time needed per processor per cell per time step remains significant. Furthermore, by using an adaptive mesh with local refinement around the liquid-gas interface in Basilisk (meshes E5, E6, E7, E8), the same accuracy for bubbles position and velocity can be achieved with much less computational effort since less total simulation time (in comparison with mesh E) with fewer processors (2 instead of 7) give similar results.

The evolution of the bubble mean rising velocity (u_y) and position (y) is illustrated in figure 4.29 for uniform meshes in OpenFOAM, uniform/non-uniform adaptive meshes in Basilisk and reference solutions in OpenFOAM, Basilisk, and MooNMD. Basilisk shows better convergence for coarser meshes in velocity and position while in reference meshes (4.29d, 4.29h), velocity plots of OpenFOAM and Basilisk coincides with a small deviation from MooNMD in the area of the second velocity maximum. Except for mesh E5, all adaptive meshes in Basilisk capture the velocity evolution with great precision.

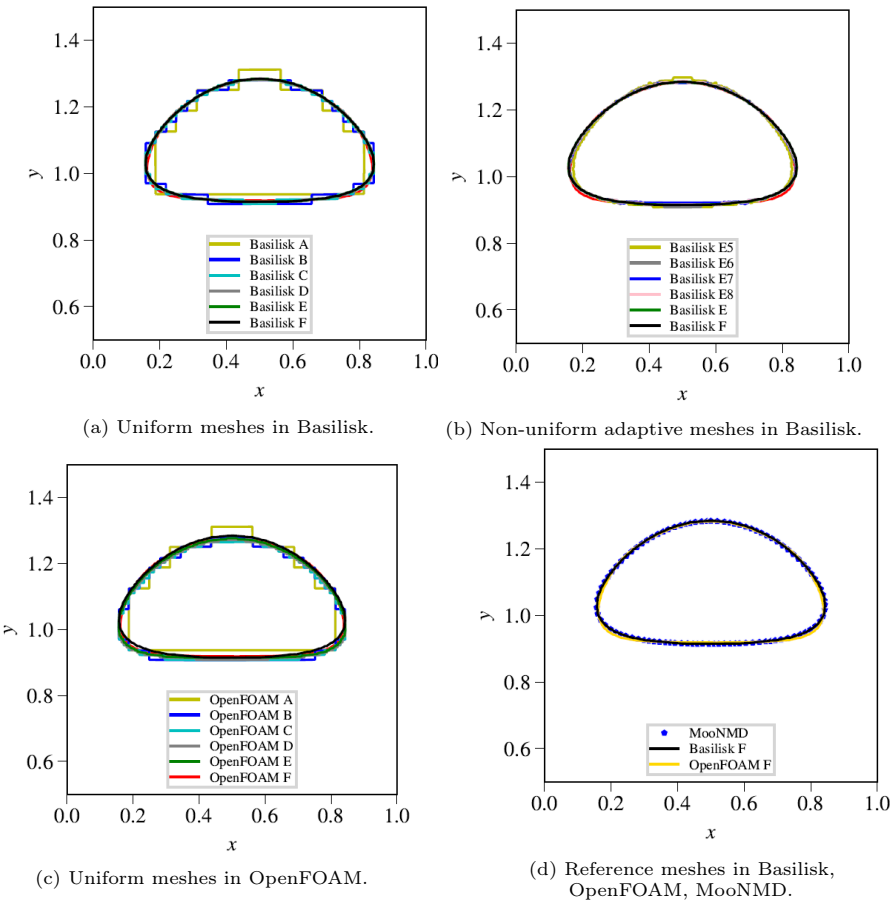

(a) Uniform meshes in Basilisk.

(b) Non-uniform adaptive meshes in Basilisk.

(c) Uniform meshes in OpenFOAM.

(d) Reference meshes in Basilisk, OpenFOAM, MooNMD.

Figure 4.28: Case 1:Final bubble's shape ($t = 3$) from simulations with different meshes in different software.

Table 4.3: Simulation data for each mesh and software for case 2.The table illustrates the number of cells per dimension, the number of processors used, the L1-norm of the two benchmark quantities (y and u_y), the total simulation time and the amount of computational time per processor per cell per time step.

OpenFOAM									
Mesh	Nx	Ny	Ncells	N_{proc}	$\|\|e_y\|\|_1$	$\|\|e_u\|\|_1$	Iter.	t_{sim}	t_{sim}* N_{proc}/N_{cells}/iter
A	16	32	512	1	0.020644	0.094559	283	5	3.45E-05
B	32	64	2048	1	0.013496	0.0597795	599	40	3.26E-05
C	64	128	8192	1	0.005868	0.034879	1146	439	4.67E-05
D	128	256	32768	2	0.002979	0.020916	2173	4237	0.000119
E	256	512	131072	7	0.00161	0.01060	4166	14096	0.000180
F (ref)	512	1024	524288	16	-	-	8160	78353	0.000293
Basilisk									
Mesh	Nx	Ny	Ncells	N_{proc}	$\|\|e_y\|\|_1$	$\|\|e_u\|\|_1$	Iter.	t_{sim}	t_{sim}* N_{proc}/N_{cells}/iter
A	16	32	512	1	0.00638	0.027158	229	6	5.80E-05
B	32	64	2048	1	0.007861	0.031076	478	35	3.59E-05
C	64	128	8192	1	0.005334	0.03344	983	350	4.34E-05
D	128	256	32768	2	0.003155	0.022860	1897	2815	9.05E-05
E	256	512	131072	7	0.001591	0.01119	3706	3929	5.66E-05
F (ref)	512	1024	524288	16	-	0	7365	23000	9.53E-05
E5	32< Nx, Ny <512		~4K	2	0.002306	0.020500	2683	696.8	0.000138
E6	64< Nx, Ny <512		~5K	2	0.003208	0.013297	2662	1269	0.000194
E7	128< Nx, Ny <512		~11k	2	0.003164	0.019591	2655	2405	0.000168
E8	256< Nx, Ny <512		~35k	2	0.002191	0.018020	2711	4290	9.18E-05

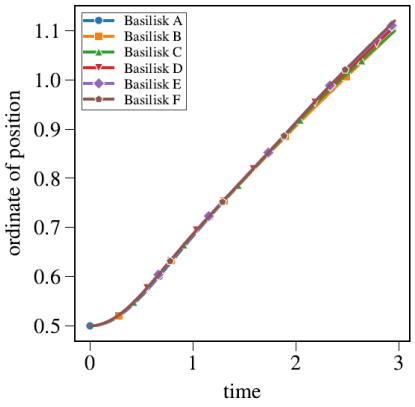

(a) Uniform meshes in Basilisk.

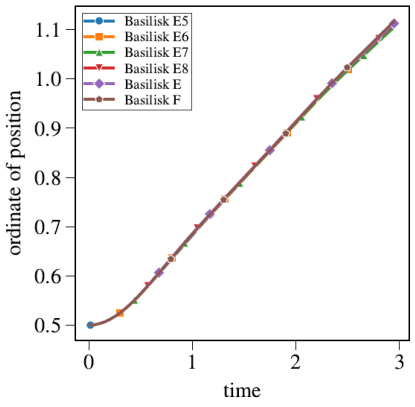

(b) Non-uniform adaptive meshes in Basilisk.

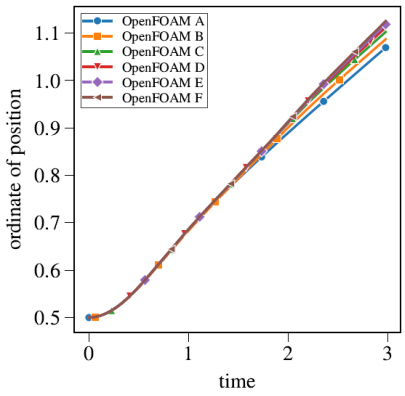

(c) Uniform meshes in OpenFOAM.

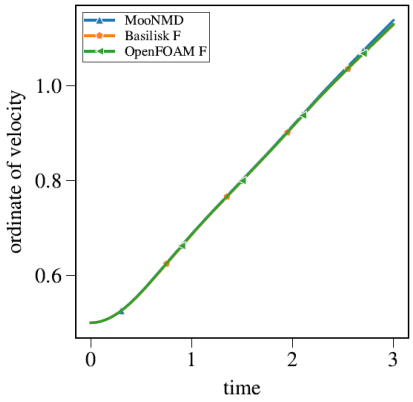

(d) Reference meshes in Basilisk, OpenFOAM, MooNMD.

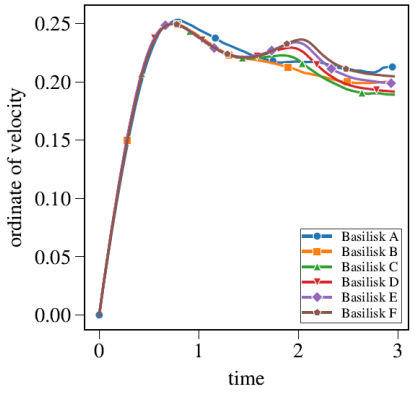

(e) Uniform meshes in Basilisk.

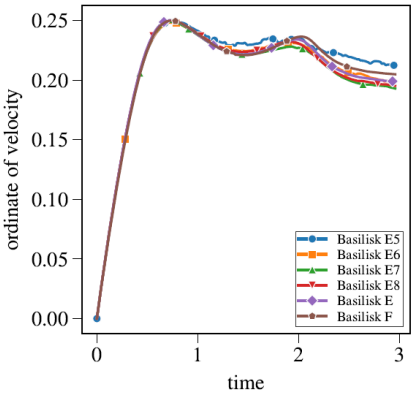

(f) Non-uniform adaptive meshes in Basilisk.

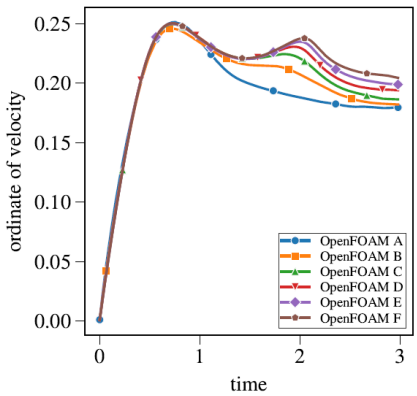

(g) Uniform meshes in OpenFOAM.

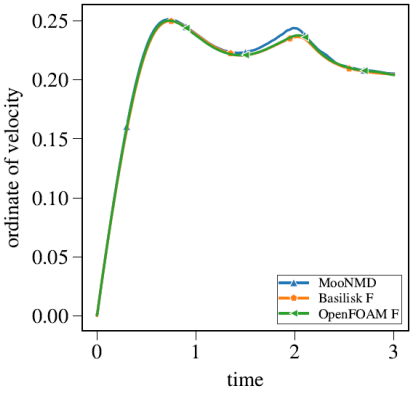

(h) Reference meshes in Basilisk, OpenFOAM, MooNMD.

Figure 4.29: Case 2: Ordinate of bubble's position and velocity along time in simulations with different meshes and software.

Figure 4.30 indicates the final shape of the bubble for simulations with a uniform grid in OpenFOAM, uniform and adapted grid in Basilisk as well as the comparison between simulations with reference meshes between Basilisk, OpenFOAM and MooNMD (4.30d). As expected from the study of [2], the final shape of the bubble is like dimpled ellipsoidal-cap with two long trailing filaments without the presence of a break up of bubbles interface. Furthermore, all adaptive non-uniform meshes near the interface in Basilisk (4.30b) match better the shape of the reference simulation than those with uniform meshes in Basilisk and/or OpenFOAM (4.28a, 4.30c).

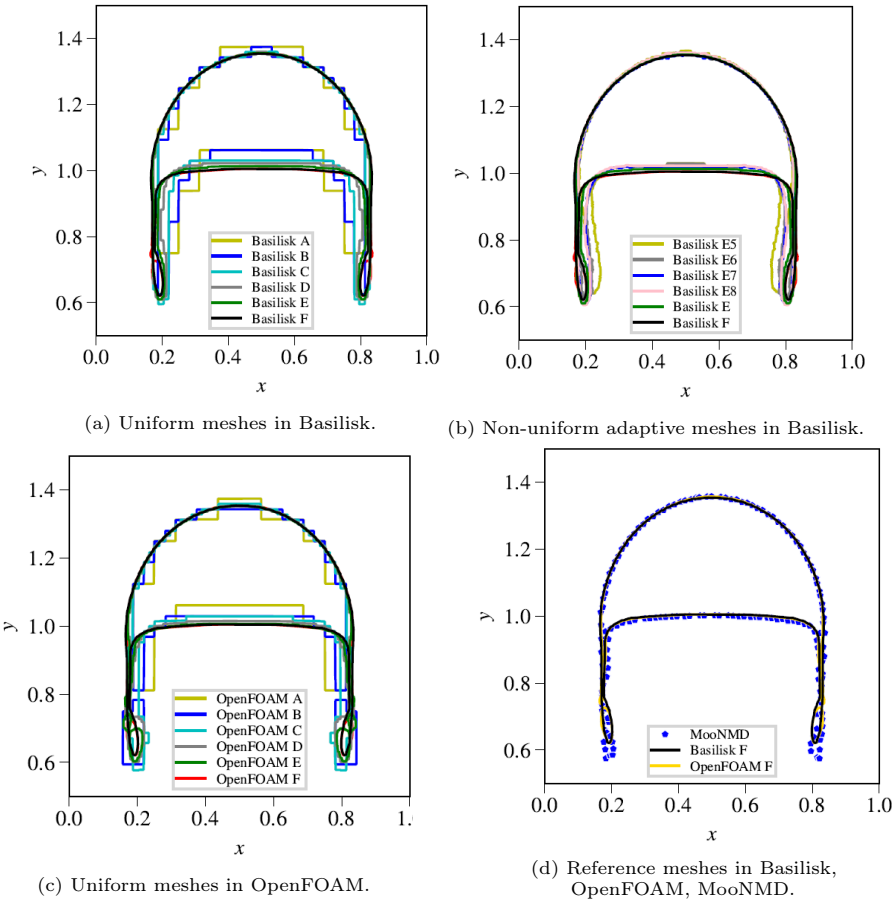

(a) Uniform meshes in Basilisk.

(b) Non-uniform adaptive meshes in Basilisk.

(c) Uniform meshes in OpenFOAM.

(d) Reference meshes in Basilisk, OpenFOAM, MooNMD.

Figure 4.30: Case 2: Final bubble's shape ($t = 3$) from simulations with different meshes in different software.

All in all, in both cases that analyzed in two-phase flow, Basilisk is found to be superior to OpenFOAM in terms of computational time and accuracy for simulations with the same uniform meshes. When using the adaptive grids with local refinement, the gain from computational effort is further increased by at least one order of magnitude. This section illustrated the potential of Basilisk to run precise simulations of two-phase flows with little computational effort and this is the reason that Basilisk was selected for running high-fidelity Taylor bubble flows.

4.2. Laminar Taylor bubble flow

4.2.1. Two-dimensional flow

The next validation case regards the laminar Taylor bubble flow in the context as illustrated [4]. In this survey, the authors simulated in ANSYS Fluent a wide range of laminar Taylor bubble flows in a stagnant liquid, by performing simulations with different Morton and Eötvös numbers. As mentioned in chapter 2.3, these two non-dimensional numbers (input parameters) together with the Froude number (output parameter) can fully describe the dynamic behavior of the Taylor bubble. The study in [4] is focused on the influence of those numbers on the hydrodynamic features that occur at the nose region, wake region and the thin liquid film created between the bubble and the pipe wall. The evolution of bubble velocity is also analyzed and all predictions of [4] are validated with the experimental results of [69], [70].

Among the different cases presented in [4], three pairs of Mo-Eo are selected to be simulated in Basilisk which result in three different flow regimes: convex tail without wake, concave tail without wake, and concave tail with wake. The choice of these configurations have been also done because the comparison can be implemented not only against the results from [4], [69], [70] but also the numerical predictions from OpenFoam as recently presented in [1].

	Tail	Wake	M	Eo	σ [N/m]	ν_ℓ [m^2/s]
Case 1	concave	yes	0.0431	187	0.000529	2.84×10^{-5}
Case 2	concave	no	0.0164	71	0.001394	4.60×10^{-5}
Case 3	convex	no	0.0164	25	0.003960	1.01×10^{-4}

Figure 4.31: Values of the properties of the simulated cases in Basilisk taken from [1], [4].

All the differences between the three cases are illustrated in figure 4.31. The rest domain and fluid properties that are not mentioned in the table are the same in all simulations: pipe Diameter $D = 0.01m$, pipe length $L = 11 \cdot D$, gas and liquid densities $\rho_g = 1kg/m^3$, $\rho_l = 100kg/m^3$ and gas kinematic viscosity $\nu_g = 10^{-5}m^2/sec$. Moreover, the Taylor bubble flow is laminar in all cases so the bubble movement in circumferential axis can be considered negligible. Therefore, the simulations can be performed in two dimensions: axial (z-direction) and radial (r-direction). The initial shape of the Taylor bubble is a hemispherical (semi-circle in 2D) front nose of diameter $D_{tb} = D - 2\delta$, with δ the film thickness, and a cylindrical main part (rectangle in 2D) of length three times the pipe diameter and width D_{tb}. Therefore, the tail of the bubble initially is flat in all simulations. The bubble is symmetrical along the pipe axis and initially the middle of its cylindrical body coincides is set to be at the point $(0.25L, 0)$ of the pipe. Thus, on the axis of the pipe ($y = 0$), symmetry boundary conditions are imposed and the simulation is performed only for the upper half of the domain ($y > 0$) which reduces computational cost and time. The initial guess for film thickness is calculated from formula 4.6 illustrated in [108]:

$$\delta = \left(\frac{3\nu_l u_{TB}}{2g(R-\delta)} (R-\delta)^2 \right)^{\frac{1}{3}}, \tag{4.6}$$

where $R = 0.5D$ and initial bubble velocity U_{TB} (only in axial direction) is calculated with the general correlation presented in [109]:

$$Fr = \frac{U_{TB}}{\sqrt{gD}} = 0.345 \left(1 - e^{\frac{-0.01 N_f}{0.345}} \right) \left(1 - e^{\frac{3.37 - Eo}{m}} \right), \tag{4.7}$$

where $N_f = \left(\frac{Eo^3}{Mo} \right)^{\frac{1}{4}}$ is the inverse viscosity number and m a parameter depending on N_f.

All simulations have been chosen to be implemented in Basilisk using a Moving Frame of Reference (MFR) which is attached to the Taylor bubble with non-periodic inlet/outlet boundary conditions as suggested in [4] and [1]. This approach solves the two main problems in the case of using a non-moving frame of reference with periodic pipe. In particular, for a choice of MFR:

- firstly, there is no need to implement a pressure jump condition from the inlet to the outlet and secondly,
- in the first case where breaking up of small bubbles occurs at the tail of the Taylor bubble, the small bubbles exit the domain together with the liquid flow and do not interact with the Taylor bubble nose as it may happen in the case of periodic (and not long enough) pipe.

In the MFR approach, the bubble remains fixed in its initial position and never exits the domain. This is achieved by balancing the buoyancy of the bubble with a force coming from the liquid which is set on a movement towards its nose. In each time step, the inlet liquid (at the top of the domain) is adapted to a uniform velocity given by the following formula:

$$U_{inlet}^{n+1} = U_{inlet}^{n} - \beta U_{TB} \tag{4.8}$$

,where β is an under-relaxation factor which in the simulations performed in Basilisk is set to half and U_{TB} is the bubble velocity in the MFR which is calculated in each time step from volume-averaged gas velocity (as calculated from NS equation in axial-direction) in the gas volume fraction $V*$.

$$U_{TB} = \frac{1}{V*} \int_{V*} \alpha (u \cdot \hat{z}) dV \tag{4.9}$$

The inlet liquid velocity in an MFR keeps the bubble fixed at the same position as it acts in the opposite direction to the buoyancy. Moreover, the wall is also set to have the same velocity with inlet liquid in all simulations since the flow problem regards a Taylor bubble flow in stagnant liquid. The same approach is described in [1]. Figure 4.32 illustrates the construction of the MFR approach as presented in [4].

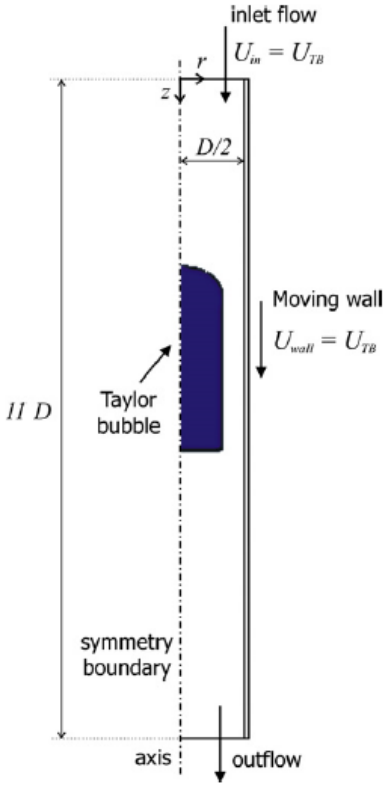

Figure 4.32: Schematic representation of the domain, boundary and initially conditions for the MFR approach as presented in [4].

All three simulation cases are implemented in Basilisk for a maximum refinement level 12 and a minimum refinement level 10 within the pipe domain while at the solid wall (from the outer side of the pipe) the level of refinement is forced to the minimum possible level, i.e. 2. In each time step, the mesh

is refined up to the maximum level near the interface and in all cells of pipe region near the wall (from the inner side of the pipe). The tolerance given for the gas volume fraction is 0.0001 while the tolerance in the region near the wall is set to 0.1 for all simulations. Since Basilisk has a varying amount of cells in each time step, an interpolation is used to create a uniform mesh (2288x104) similar to the reference solutions, so that the aspect ratio of cells is unity (since $L = 11D$). An implicit treatment of velocity with post-processing is applied in each time step to achieve a damping of velocity near the inside pipe wall for the construction of the embedded boundaries. As it is illustrated in the next section, although this post-processing approach to the standard Basilisk solver for damping the velocity near the pipe wall seems to work fine in two dimensions, it shows an important divergence in three-dimensions.

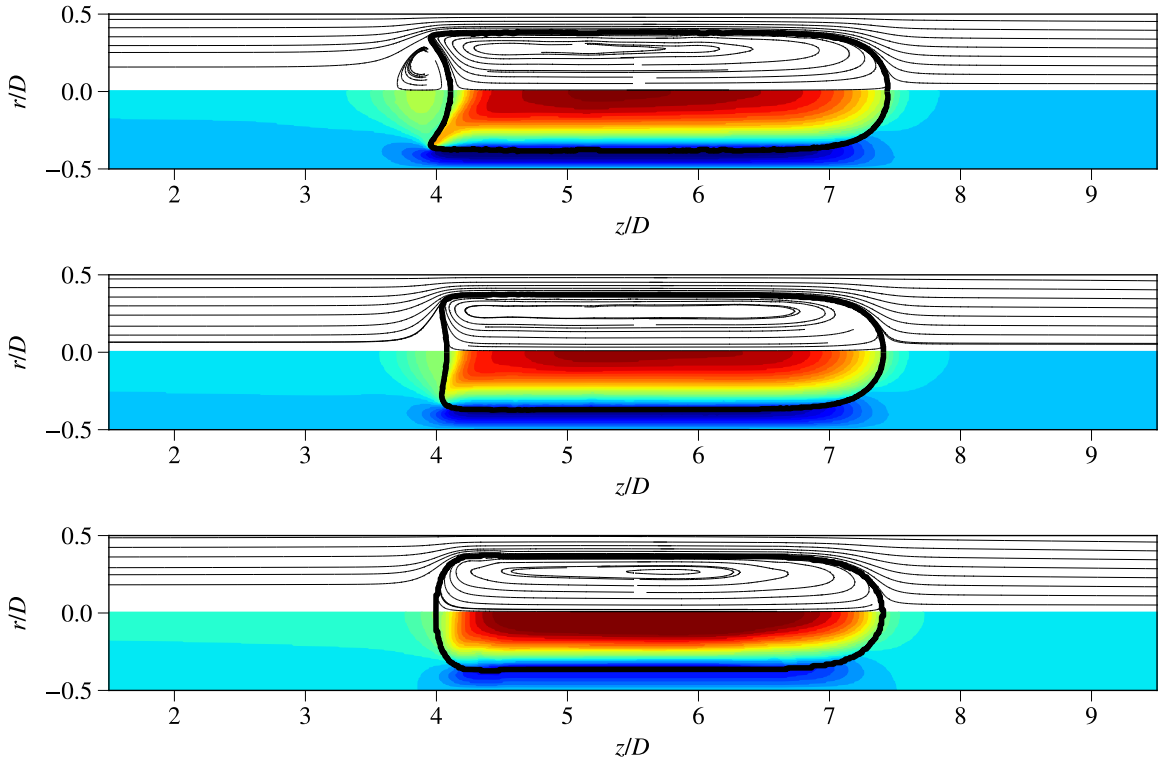

Figure 4.33: Streamlines contours (top half of each figure) and axial component of liquid velocity scaled by actual Taylor bubble velocity for an MFR attached to the bubble (bottom half of each figure) for the three cases (case 1 top, case 2 middle, and case 3 bottom figure). The color map ranges from -1 (dark blue) to 1 (dark red). The interface of the Taylor bubble (black line) at f = 0.5. Simulations performed in 2D with levels of refinement ranging from 10 to 12.

The results of the three simulations cases are indicated in figure 4.33. Starting from the first case at the top sub-figure and ending at the third case at the bottom, each sub-figure is divided into two different pieces. The upper part illustrates the streamline contours while the lower part shows the axial component of liquid velocity scaled by actual Taylor bubble velocity for an MFR attached to the bubble. Comparing with [4, ANSYS] and [1, figure 4, OpenFOAM] , all cases show the expected behaviour. In particular, the Taylor bubble has a concave tail with wake in case 1, concave tail without wake in case 2 and convex tail without wake in case 3. Moreover, in all cases, the Taylor bubble has a thoroidal vortex. This occurs due to the fact that the axial velocity is positive (dark red in the color map) near the core of the bubble and negative (blue) near the interface. All simulation cases indicate (almost) steady-state. In particular, the free-stream liquid velocity (e.g. in the inlet) is resulted around $u_{inlet} \sim 0.1$ for the first case, $u_{inlet} = 0.09$ for the second and $u_{inlet} = 0.061$ for the third case in Basilisk. Similarly with OpenFOAM simulations illustrated in [1], some unsteadiness at the tail of the bubble occured in Basilisk at the first case with break up of small bubbles as the time is passing and therefore, a time-averaging procedure is performed for the calculation of the steady axial velocity.

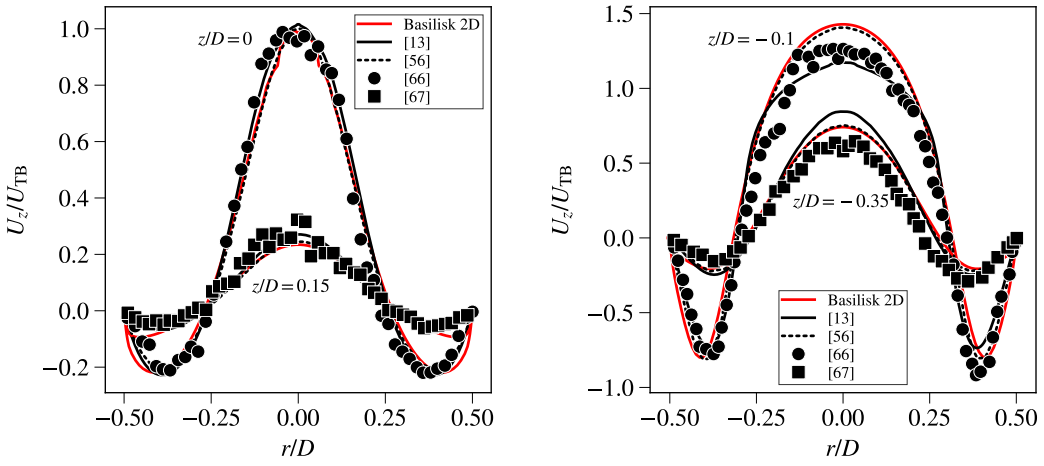

(a) (b)

Figure 4.34: Comparison of dimensionless axial velocity $\frac{U_z}{U_{TB}}$ for case 1 (concave tail with wake) between Basilisk and numerical results of [4, ANSYS], [1, OpenFOAM] and experimental results of [69], [70]. Comparison is performed in a non-moving frame of reference (NMFR) and the measurements are implemented for the radial planes located at distance $z = 0$ and $z = 0.15D$ upstream the bubble nose (left sub-figure) and in the wake region downstream the bubble (right sub-figure) at distance $z = -0.1D$ and $z = -0.35D$ from the tail. Simulation in 2D with levels of refinement ranging from 10 to 12.

A quantitative comparison of axial velocity scaled with the actual bubble velocity $\frac{U_z}{U_{TB}}$ for the first case (concave tail with wake) is implemented between Basilisk and the numerical results as presented in [4, figure 4] obtained with ANSYS, in [1, figure 5] obtained with OpenFOAM. All of them are also compared against the experiments performed in [69], [70]. The liquid velocity is measured both upstream the Taylor bubble (4.34a), exactly at the nose interface and at distance $z = 0.15D$ from the nose, and downstream the tail of the bubble (4.34b) at distances $z = 0.1D$ and $z = 0.35D$ in absolute values. The scaled axial velocity is calculated for an NMFR and the results in Basilisk are in line with the other studies, i.e. the axial velocity follows a parabola curve. In particular, both upstream and downstream of the bubble, the liquid velocity is maximum at the middle of the pipe ($r = 0$) and closer to the interface ($z = 0$) while it reaches a negative value at the thin liquid film between the wall and the bubble.

In general, good quantitative and qualitative matching of Basilisk for all cases with numerical findings of [4, ANSYS], [1, OpenFOAM] and experimental results of [69], [70]. After the successful implementation of the laminar Taylor bubble flow in two dimensions, an extension of the same study into three dimensions is performed in Basilisk. The reason for this decision is that since the main goal is to simulate a Taylor bubble in turbulent flow later, it is necessary firstly to validate Basilisk in three-dimensional two-phase flow in the simpler case of laminar flow.

4.2.2. Three-dimensional flow

The above laminar Taylor bubble flow problem is also simulated in Basilisk in three-dimensions. Although more computational cost in comparison with the 2D (two orders of magnitude more cells for the same simulation parameters), interesting conclusions can be extracted from the three-dimensional simulation which is useful for the turbulent Taylor bubble flow later. For a choice of a maximum refinement level 10 (11 for the first case) and a minimum refinement level 9 (10 for the first case), the domain is split into more than 2 million cube cells.

Although figure 4.35 indicates similar quantitative results for streamline contours with 4.33 for all cases, figures 4.36a , 4.36b show a deviation of the axial liquid velocity profile in the region near the wall which is not present in 2 dimensions(4.34a).

This deviation leads to the need for an improved N.S. solver in Basilisk as described in section 3.2. The solver uses general PISO-like approach built around a general Runge-Kutta (RK) Butcher tableau, fully discretizes the shear strain rate tensor, uses harmonic mixing for the computation of viscosity, and implements the volume penalization method for the smoother damping of the velocity near the inside walls. The latter is the most important reason why the modified solver produces accurate predictions for the axial velocity profiles as indicated in figures 4.37a, 4.37b.

The explanation for the deviation between the standard and modified solver can be seen in figure 4.38 indicating the radial velocity profile. Although the standard N.S. conserves mass, a part of it is not advected along the pipe but it is moving into the radial direction. Moreover, the modified N.S. solution results in a smoother velocity damping at the wall.

Another interesting observation is the fact that steady-state is achieved for all cases from very early time steps in the modified three-dimensional simulation in Basilisk. In particular, the steady inlet liquid velocity found to be $u_1 = -0.096$, $u_2 = -0.087$, $u_3 = -0.044$ for the first, second and third case correspondingly. On the contrary, simulation in Basilisk in two-dimensions as well as in [1] predicted some unsteadiness for the first case.

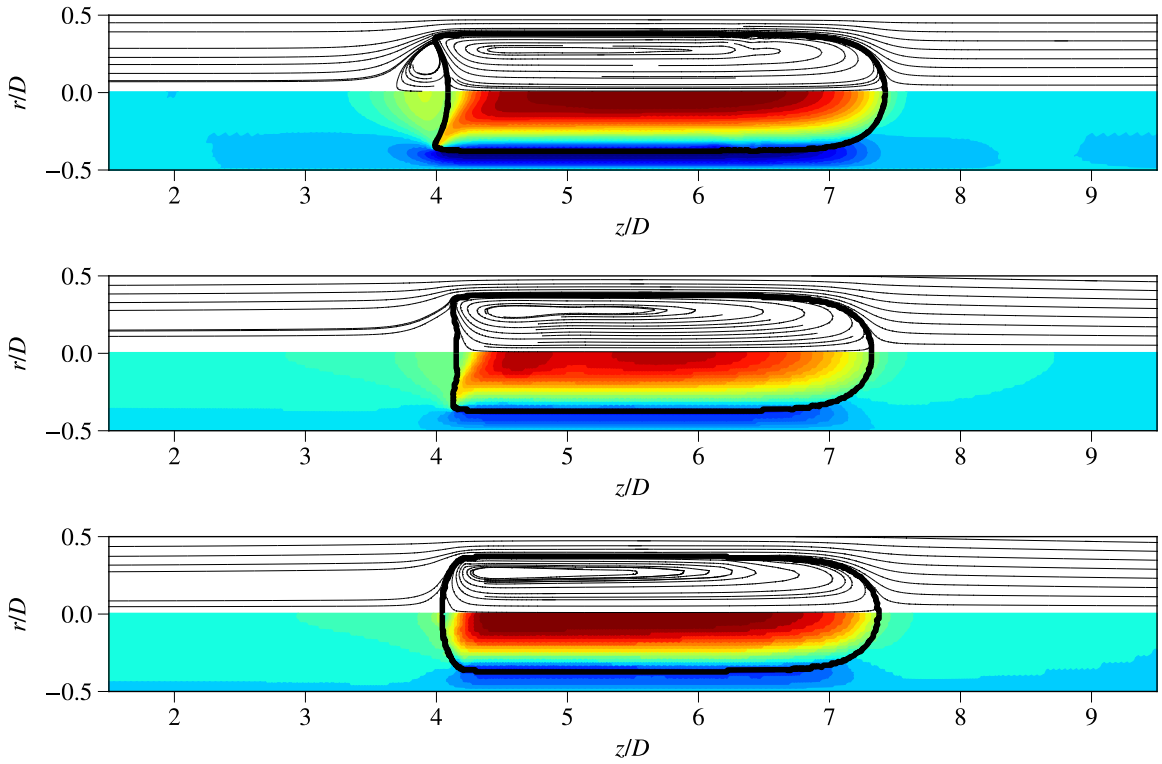

Figure 4.35: Streamlines contours (top half of each figure) and axial component of liquid velocity scaled by actual Taylor bubble velocity for an MFR attached to the bubble (bottom half of each figure) for the three cases (case 1 top, case 2 middle, and case 3 bottom figure). The color map ranges from -1 (dark blue) to 1 (dark red). The interface of the Taylor bubble (black line) at f = 0.5. Simulation in 3D with levels of refinement ranging from 9 to 11.

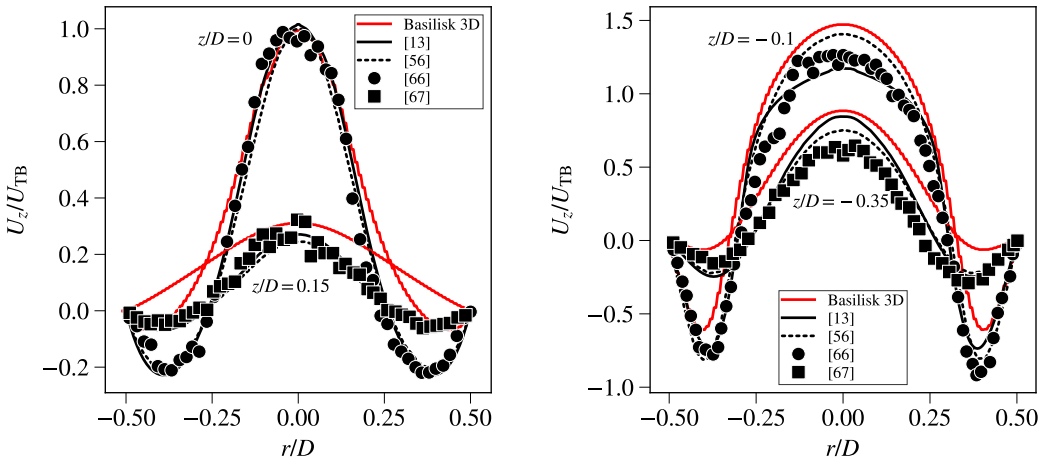

(a) (b)

Figure 4.36: Simulation in 3D with standard N.S. Basilisk solver and levels of refinement ranging from 10 to 11. Comparison of dimensionless axial velocity $\frac{U_z}{U_{TB}}$ for case 1 (concave tail with wake) between Basilisk and numerical results of [4, ANSYS], [1, OpenFOAM] and experimental results of [69], [70]. Comparison is performed in a non-moving frame of reference (NMFR) and the measurements are implemented for the radial planes located at distance $z = 0$ and $z = 0.15D$ upstream the bubble nose (left sub-figure) and in the wake region downstream the bubble (right sub-figure) at distance $z = -0.1D$ and $z = -0.35D$ from the tail.

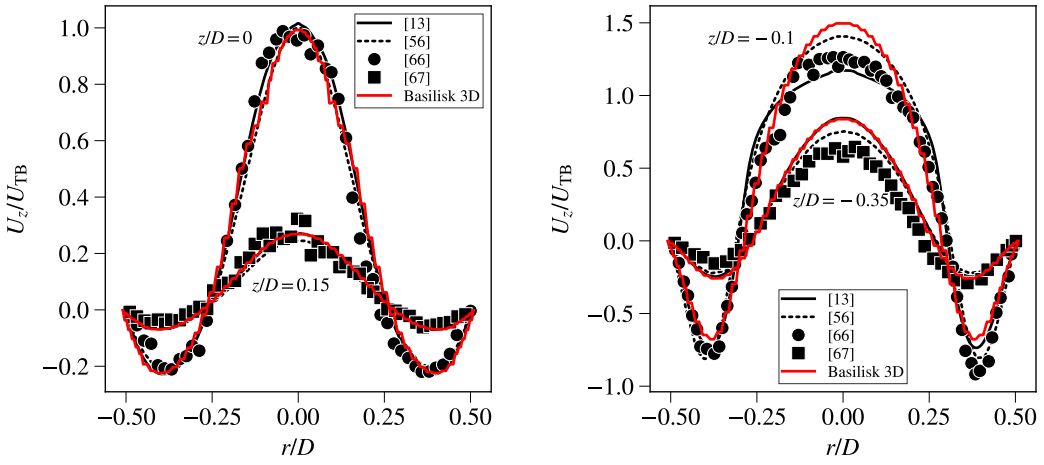

(a) (b)

Figure 4.37: Simulation in 3D with modified N.S. solver levels of refinement ranging from 10 to 11. Comparison of dimensionless axial velocity $\frac{U_z}{U_{TB}}$ for case 1 (concave tail with wake) between Basilisk and numerical results of [4, ANSYS], [1, OpenFOAM] and experimental results of [69], [70]. Comparison is performed in a non-moving frame of reference (NMFR) and the measurements are implemented for the radial planes located at distance $z = 0$ and $z = 0.15D$ upstream the bubble nose (left sub-figure) and in the wake region downstream the bubble (right sub-figure) at distance $z = -0.1D$ and $z = -0.35D$ from the tail.

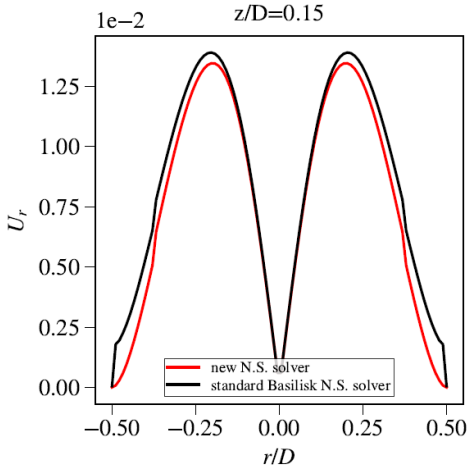

Figure 4.38: Radial velocity profile ahead the nose at distance $z/D = 0.15$. Comparison between 3D standard and modified N.S. solver.

The three-dimensional approach provide useful information about how gas fraction, velocity, and pressure field are distributed across pipe axis. In particular, planes normal to axial direction can be created by slicing the pipe at certain positions upstream, downstream, and in the middle of the bubble.

The analysis is presented only for the first case since it results in the most interesting hydrodynamic features among the three cases (unsteadiness, concave tail, wake region with break up of small bubbles). Figure 4.39 indicates the cross-cutting plane of the pipe in the middle of the domain which is also the plane passing through the middle of the main cylindrical part of the bubble. Therefore,in figure 4.39a, the gas fraction is represented by a circle of radius $R - \delta$, as calculated by 4.6. The thin liquid film is also a circle that is created between the pipe wall and the bubble. As expected from figure 4.35, the streamwise velocity is changing from positive at the core of the bubble to negative as it approaches the interface due to the thoroidal vortex (4.39b).

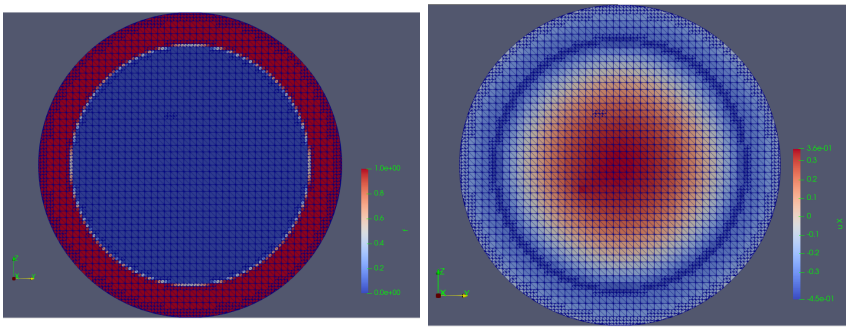

(a) (b)

Figure 4.39: Profile view of gas (void fraction $f = 0$) /liquid fraction ($f = 1$) (4.39a) and axial velocity (4.39b) by vertically slicing the pipe across the pipe axis at the middle of the domain for case 1.

Figure 4.40 illustrates a cross-cutting plane with the same orientation at the gas/liquid interface at the bubble's front nose. Since the nose is semi-spherical, the two-dimensional interface appears as a small circle (figure 4.40a). The axial component of velocity is dominant (figure 4.40b) with an equally distributed velocity to the other two directions (figures 4.40c, 4.40d).

Last but not least, figure 4.41 shows the plane normal to the axial direction in the region slightly downstream the tail of the bubble. Similarly to what indicated in two dimensions (figure 4.33), a wake appears in this small region and thus, the velocity is spreading in all directions with the same order of magnitude (figures 4.41b, 4.41c, 4.41d). Moreover, three small areas with bigger level of refinement come into view in sub-figure 4.41a. This is due to the small bubbles which break up from the Taylor bubble which would be more visible if the maximum level of refinement was greater.

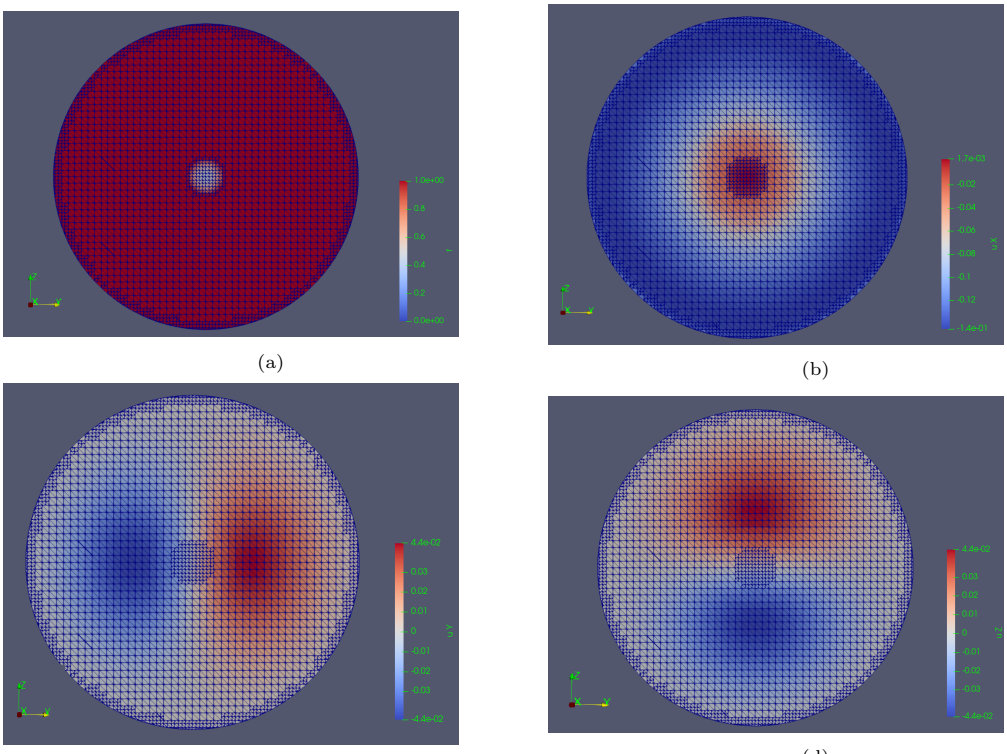

(a) (b) (c) (d)

Figure 4.40: Profile view of gas/liquid fraction (4.40a) and velocity components in x- (streamwise, 4.40b), y- (4.40c) and z-direction (4.40d) by slicing the domain across the pipe axis at the gas/liquid interface at bubble's nose for case 1.

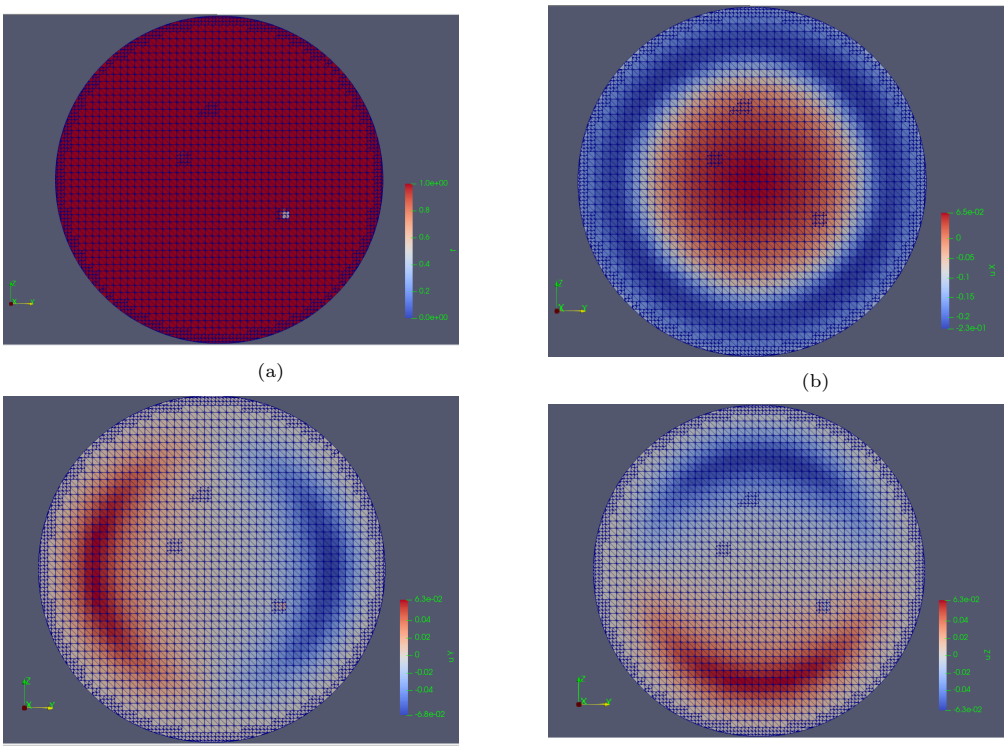

(a) (b) (c) (d)

Figure 4.41: Profile view of gas/liquid fraction (4.41a) and velocity components in x- (streamwise, 4.41b), y- (4.41c) and z-direction (4.41d) by slicing the domain across the pipe at the wake region downstream the bubble for case 1.

4.3. Turbulent co-current Taylor bubble flow

The results from laminar Taylor bubble flow 4.2 indicate that Basilisk shows great potential for producing high-fidelity simulations of Taylor bubbles in the turbulent co-current flow.

As mentioned in section 2.4.1, the only fully three-dimensional simulation that predicts the motion of an individual Taylor bubble in a turbulent co-current liquid flow is implemented in [1, OpenFOAM] which uses the setting as presented in the experimental results of [3]. The study of [1] indicates the results of a Large Eddy Simulation (LES) and is focused on the hydrodynamic features that happen in the wake region behind the Taylor bubble both qualitatively and quantitatively. Since an underestimation of the turbulent fluctuations in the wake of the Taylor bubble was observed in the LES results in [1], it was suggested by the authors that LES mesh resolution is not sufficient to capture the break-up and bubble formation accurately.

The current work comprises a continuation of the study of [1] and moves towards a DNS approach of co-current turbulent Taylor bubble flow using the Basilisk code. Before validating the results of Basilisk simulations against the reference studies of [1], [3] for turbulent co-current Taylor bubble flow, it is essential firstly to describe the simulation strategy that has been followed. Part of it is the simulation of single-phase pipe flow since upward the Taylor bubble, there is only fully developed turbulent liquid flow.

4.3.1. Single-phase turbulent pipe flow

The validation of the Basilisk code for single-phase turbulent pipe flow has been done both quantitatively and qualitatively against [92]. However, the current study is focused only on two-phase flows (and in particular, in Taylor bubble flows) so the validation of Basilisk in single-phase pipe flow is out of the scope of this work and will only be part of a future publication. The main objective from the simulation of turbulent single-phase pipe flow in the current work is to investigate the size of the necessary pipe length for producing a simulation with fully-developed turbulent liquid flow. The resulting flow field is used as the initial flow field of the Taylor bubble flow. This is the reason why the Basilisk code has been also tested for the flow parameters with the turbulent Taylor bubble flow (as presented in [3]).

As explained in chapter 1, when the flow in pipes becomes turbulent, large rotational eddies are forming in regions of high shear near the wall which results in non-smooth values of velocity and pressure fields. The local velocity within the eddies has components in all three dimensions and therefore, it is different from the bulk velocity of the stream. Thus, in turbulent pipe flow, a division of Reynolds number into the bulk and the friction one(near the wall) is necessary for the analysis. The bulk Reynolds number is based on the bulk mean velocity (4.3.1) and the channel width while the friction Reynolds to the friction velocity (4.3.1) correspondingly:

$$Re_{bulk} = \frac{u_{bulk} \cdot D}{\nu} \tag{4.10}$$

$$Re_{\tau} = \frac{u_{\tau} \cdot D}{\nu} \tag{4.11}$$

The turbulent pipe flow is simulated to validate Basilisks performance in a cylindrical domain, for which the volume penalization method is applied for modeling the velocity field near the wall as presented in 3.2. The turbulent flow of the liquid occurs in a cylindrical pipe of length $16D$ (with $D = 1.4cm$ the diameter of the pipe) with bulk Reynolds number $Re = 8250$. The liquid density is at $\rho = 1000kg/m^3$ and the kinematic viscosity $\nu = 10^{-3}m^2/sec$. The flow loses kinetic energy near the wall due to shear stress and is driven by a spatially uniform pressure gradient given by the formula 4.3.1 in [110]:

$$\frac{\partial p}{\partial x} = -4\frac{\rho u_{\tau}^2}{D} \tag{4.12}$$

Periodic boundary conditions are defined in the axial direction while no-slip for the velocity and zero normal-gradient for pressure at the wall are imposed in the other directions. The initial uniform axial velocity is set to $u_z = \frac{\nu Re}{D}$ while the initial uniform pressure field $p = 0$. Regarding the meshing strategy,

cell dimensions are expressed in wall units, i.e. the first layer of cells at the wall has a wall-normal size of roughly $\Delta y^+ = 1$ wall unit which is defined according to [110] as:

$$\Delta y^+ = \Delta y \frac{u_\tau}{\nu} = Re_\tau \frac{\Delta y}{D} \tag{4.13}$$

Figures 4.42 and 4.43 illustrate the average in time and space(in tangential direction) streamwise velocity and the root mean squared (RMS) velocity fluctuations for simulations with two different meshes in Basilisk. It is concluded that the coarser mesh 10-10 is accurate enough and shows negligible deviation from the finer mesh regarding streamwise velocity and velocity fluctuations. Moreover, as expected velocity fluctuations in the axial direction is bigger than in the other two directions. The friction Reynolds number has been computed equal with $Re_\tau = 532$.

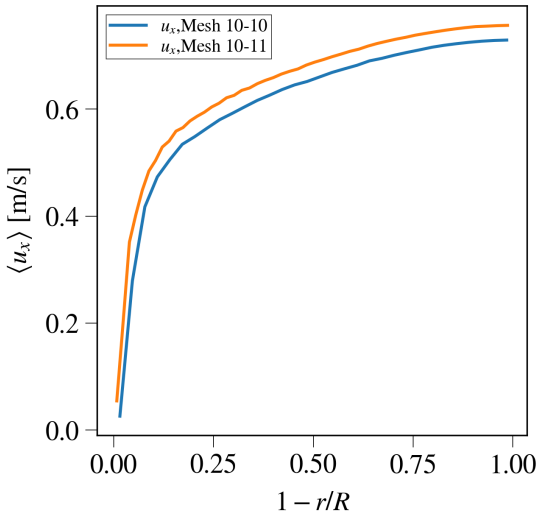

Figure 4.42: Streamwise velocity averaged in time and space(in tangential direction) for simulations with two different meshes in Basilisk.

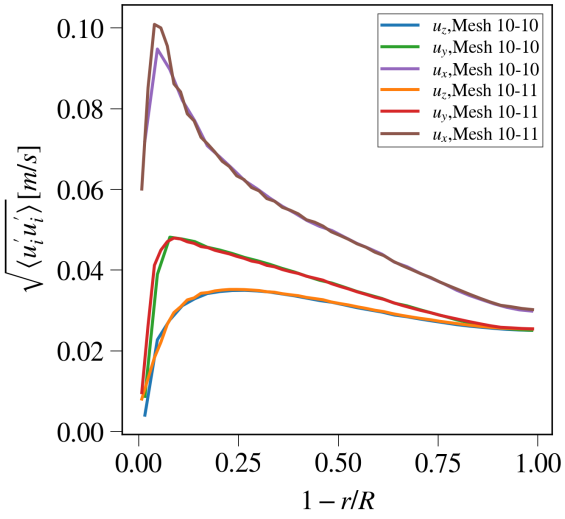

Figure 4.43: RMS Velocity fluctuations averaged in time and space(in tangential direction) for simulations with two different meshes in Basilisk.

The outcome of single-phase flow simulations in Basilisk is used for the simulation setup of the turbulent co-current Taylor bubble flow which is presented in the next sections. In particular, a snapshot of the velocity field at fully developed turbulent pipe flow is used as an initial snapshot for the two-phase simulation of Taylor bubble flow, where ahead of the bubble, single-phase liquid turbulence is recycled over an interval of $\pi \cdot D$ at the top boundary of the vertical pipe. The snapshot of turbulent pipe flow at time $t = 9s$ is illustrated in figure 4.44.

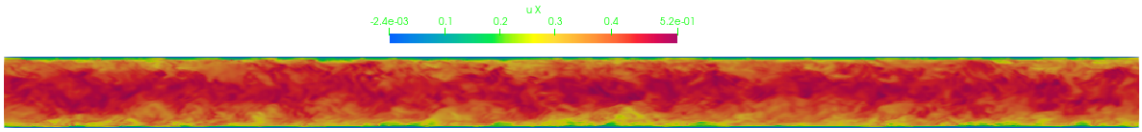

Figure 4.44: Streamwise velocity field in single-phase turbulent pipe flow in Basilisk at $t = 9s$.

4.3.2. Simulation setup

Table 4.4 illustrates the flow parameters for the turbulent co-current Taylor bubble as indicated in [1]. Since $Re = 8250$, it is clear that we are in the turbulent flow regime where the bubble (i.e. air) is moving upwards in the vertical pipe under buoyancy with actual velocity $u_{tb} = 0.83m/s$ and the inlet liquid (i.e. water) is flowing in the same direction with the bubble with actual velocity $u_{bulk} = 0.59m/s$ (positive in the direction opposite to gravity). The frictional velocity near the wall is $u_\tau = 0.038m/s$ according to equation 4.3.1. The very small Mo and the low Eo numbers indicate that interfacial forces are dominated in the flow with negligible viscous forces trying to delay the bubble decay. Although the turbulent Taylor bubble flow problem is completely unsteady, the bubble is expected to have a concave tail with the presence of the wake behind it for the given Mo and Eo numbers according to the studies of [3], [1]. The pipe in the experiment of [3] is six meters long and the initial bubble length (length of main cylindrical part) is $L_{tb} = 2D = 0.026m$.

Table 4.4: Flow properties for the turbulent co-current Taylor bubble as presented in [1].

Property	Value
Pipe diameter D	1.4 cm
Liquid bulk velocity U_{bulk}	0.59 m/s
Bulk Reynolds number Re_{bulk}	8250
Relative Taylor bubble velocity U_{tb}	0.24 m/s
Frictional velocity u^*	0.038 m/s
Eötvös number Eo	28
Morton number M	2.85×10^{-11}

The simulation setup of the turbulent co-current Taylor bubble flow setup is similar to the setup used in [1]. In the case of laminar Taylor bubble flow 4.2.1, the Taylor bubble started to move due to buoyancy in an initially stagnant liquid. Therefore, for a choice of MFR attached to the bubble, the relative wall velocity was equal with the relative inlet liquid velocity. However, this is not true in the case where the liquid has an actual inlet velocity. The wall velocity in this configuration for an MFR differs from the relative inlet liquid velocity by the actual mean liquid velocity, which is known as bulk velocity.

$$U_{wall} = U_{inlet}^{n+1} - U_{bulk} \tag{4.14}$$

Therefore, equations 4.8, 4.9 are now paired with equation 4.14 in each time step for an MFR. However, there are three important modifications in equations 4.8, 4.9 in the turbulent co-current case. In particular:

- Firstly, for the calculation of the volume-averaged bubble's velocity with equation 4.9, the chosen gas volume $V*$ is limited at the front half of the bubble only. The reason that the averaging occurs only at the nose is to avoid including in the calculations the volume of the small bubbles detached

from the tail of the bubble as the time goes on and which are either transported downwards with the liquid flow or merge again to the bubble.

- Secondly, to achieve accurate results, the initial velocity should already be turbulent. Therefore, single-phase pipe flow simulations with the same flow parameters as in two-phase flow were initially run in Basilisk for $t = 10s$. Different velocity profiles of the single-phase flow within this interval are set as the initial profile of the two-phase Taylor bubble flow for each simulation. Due to the randomness of turbulent flow, profiles from different snapshots are statistically independent of each other.
- A recycled adapted inlet flow has been used for verifying fully developed turbulent flow. The recycled cross-pipe Simulations of single-phase pipe flow in Basilisk shown that $\pi * D$ comprises a sufficient length (section 4.3.1).

$$\mathbf{U}_{inlet}^{n+1}(x,y,z) = \mathbf{U}_{inlet}^{n}(x - \pi \cdot D, y, z) - \beta U_{TB} \tag{4.15}$$

, where x is the axial direction and with under-relaxation parameter is chosen $\beta = 0.1$ such that the oscillations of the bubble's position are reduced along time. The idea of the recycled inlet was taken from [1].

The pipe length in Basilisk has been chosen $L = 16D = 0.224m$. Moreover, the thin liquid film was calculated as $\delta = 0.001m$ according to equation 4.6 so the diameter of the main cylindrical part of the bubble is set to $D_{tb} = 0.012m$. Last but not least, the bubble's nose is initially set to be at a distance $x = 1.5\pi D$ from the inlet such that there is sufficient margin of $0.5\pi D$ so that the recycling cross-section profile is far enough from the nose so that is not affected by the presence of the bubble. Moreover, there is enough distance downstream of the bubble until the outlet and in any case larger than the wake length. Figure 4.45 illustrates the domain and the simulation setup in Basilisk.

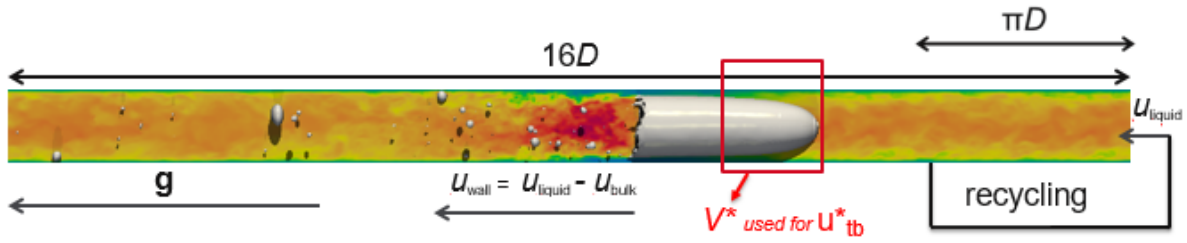

Figure 4.45: Simulation setup using an MFR attached on the bubble.

4.3.3. Preliminary simulations and discretization schemes

Despite the strong interfacial forces, the bubble is losing mass gradually due to instabilities at the tail, and therefore the problem is unsteady. The small bubbles that break up from the Taylor bubble are either carried away by the liquid flow or they merge back again to the bubble. Therefore, the flow problem is changing as time goes on since the mass of the bubble is reduced.

Preliminary simulations in Basilisk also indicate that the problem seems not only time-dependent but it is also sensitive to the selected mesh. The coarser the grid, the bigger loss of void is observed which is in agreement with whats is concluded in [1]. This happens because coarser grids cannot capture such sharply the actual curvature of the interface (especially at the tail) which leads the bubble to smear out and therefore, to bigger entrainment of liquid into the bubble which results in bigger bubble decay. However, decay in Basilisk seems to be much less in comparison with [1, OpenFOAM] at the same time snapshots since a decay of $D/2$ at pipe axis is not achieved even for simulations with very coarse meshes in Basilisk as figure 4.46 illustrates in which snapshots of the flow field are taken at specific times that are chosen with indicator the flow-through time (FFT). One FFT comprises the time which is needed for the inlet liquid to pass through the whole pipe if the bubble was not present with the given velocity, i.e.

$$FFT = \frac{L}{u_{bulk}} = \frac{0.224m}{0.59m/s} = 0.38s \tag{4.16}$$

Regarding mesh strategy, for a fully DNS approach, high resolution at the wall is necessary to minimize the artificial numerical dissipation. However, since stretched meshes could only be used in single-phase flow problems in Basilisk yet, no stretching has been implemented in the current study. Therefore, due to limited computing power, it is difficult to attain computational meshes with cell size $\Delta y^+ = 1$ (i.e. one wall unit as defined in 4.3.1) in the current study for the given setting.

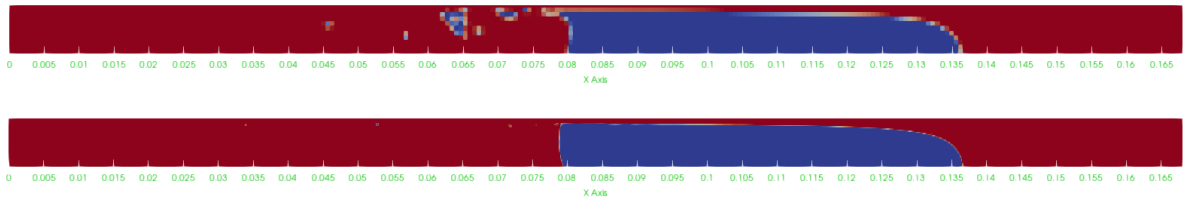

(a) Coarse (top) and fine(bottom) grid at half FFT.

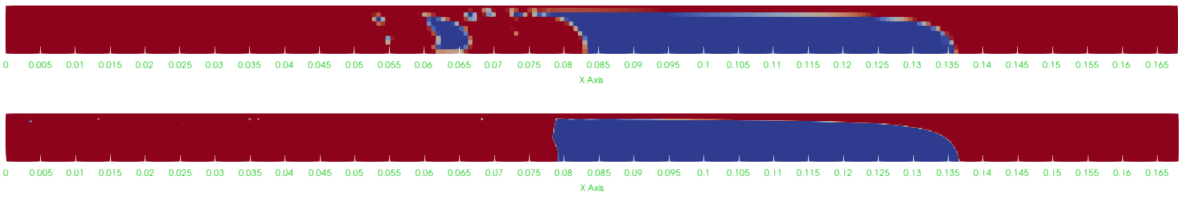

(b) Coarse (top) and fine(bottom) grid at 1 FFT.

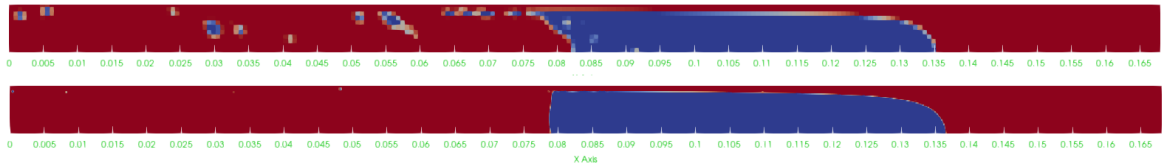

(c) Coarse (top) and fine(bottom) grid at 2 FFT.

Figure 4.46: Preliminary simulations of turbulent Taylor bubble flow at different snapshots for coarse at the top (levels of refinement 7-8) and fine grid at the bottom (level of refinements 9-10) with the same flow parameters.

Moreover, the choice of the spatial discretization scheme and time integration scheme affect the stability and convergence of the solution. Therefore, in the first place, it is important to select the best schemes for accomplishing a high-fidelity simulation of the turbulent Taylor bubble flow. For example, choosing a central/linear discretization scheme for both convective and diffusive terms, the bubble crashed and the simulation stops after a while. This happens because the scheme is not of a positive type for all Peclet numbers for all cells, i.e. the local mesh Peclet number is too large $|p| = h \cdot |u| \cdot Pe >> 2$ which leads to convergence problems [7].

This problem can be overcome by treating differently the convection term $\nabla \cdot (uu)$ of Navier-Stokes equations (equation 2.10) and the same time fully discretized the deformation tensor as described in section 3.2. In particular, if a first-order upwind scheme is used for the convection term (and central for the diffusive term), then stability is achieved. However, the upwind scheme is too dissipative, so it leads to numerical errors. A third option is to take a linear upwind scheme which is more accurate (second-order) than upwind. Nevertheless, there is a need to preserve monotonicity and prevent the local minimal/maximal by limiting the spatial velocity derivatives to realistic values. This can be done by applying advanced discretization schemes that use flux limiters in high-resolution schemes (TVD schemes) [7], [111]. The flux limiters differ from each other on the way they treat the fluxes between neighbor cells. Several flux limiters of order 2 (superbee, minmod, ospree, etc.) have been tested in Basilisk for the discretization of the convection term and compared to each other. The resulting shapes at $t = 3$ of the bubble are indicated in figure 4.47. The best choice found to be a combination of two schemes: minmod (limiter with less numerical dissipation) is only applied near the interface to ensure stability and flux monotonicity while far away from the the interface (i.e., in single-phase regions), central/linear scheme (limiter function is one) is selected to reduce artificial numerical dissipation.

To achieve the best combination of accuracy, convergence, and computational cost, the investigation has been also done on time integration schemes. For any choice of flux limiter for the spatial

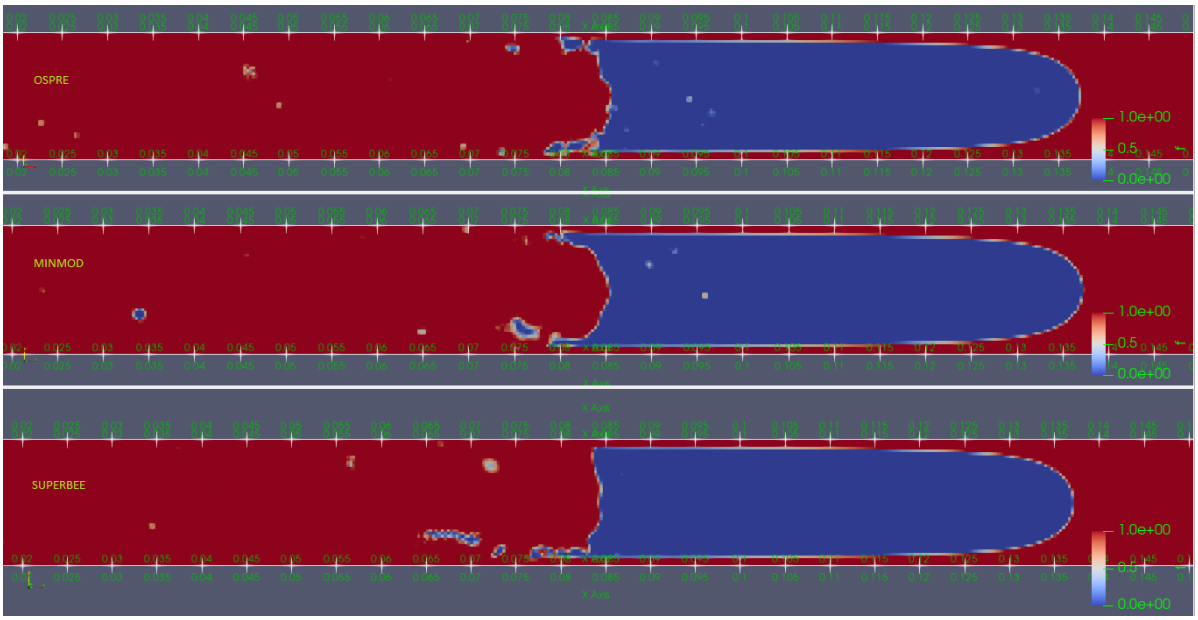

(a) Void fraction.

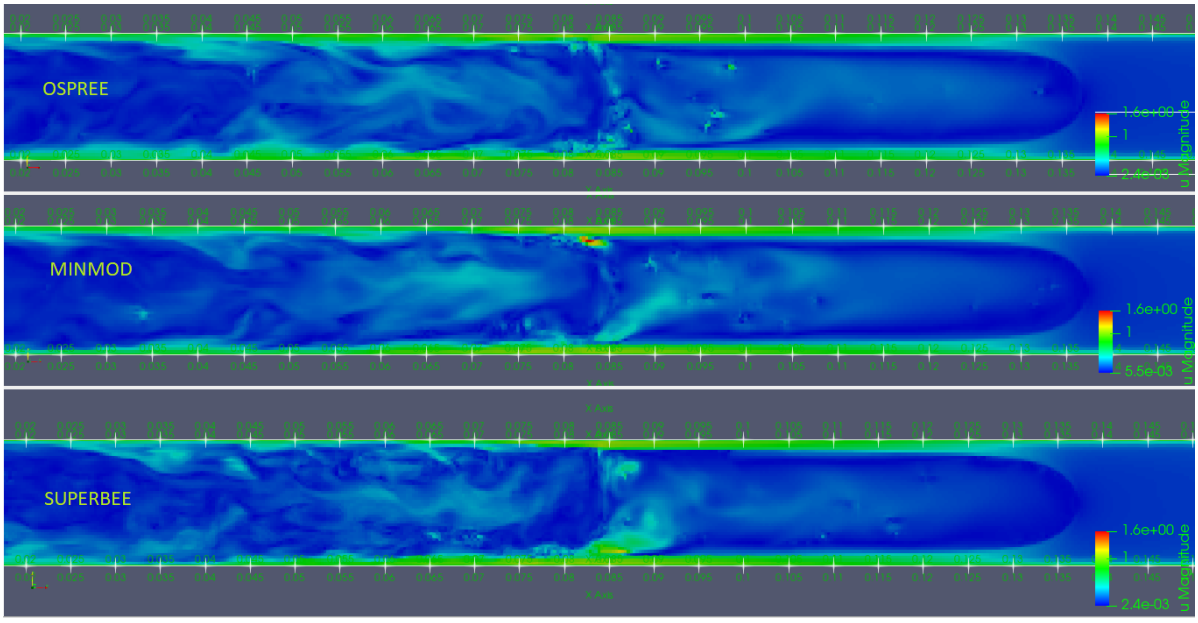

(b) Magnitude of velocity.

Figure 4.47: Preliminary simulations of turbulent Taylor bubble flow using different flux limiters (from top to bottom: ospree, minmod, superbee) at time snapshot at $t = 3s$ and a plane normal to the circumferential direction.

discretization of the convective term, an extra non-linear term is added in the momentum equation so fully implicit schemes found to be too costly in Basilisk. Therefore, several linear multistep time discretization implicit-explicit schemes (IMEX) were tried for the solution of the convection-diffusion problem, i.e. explicit Euler for the convective term and implicit Euler for the diffusive term. Basilisk was found to have great sensitivity in the selected RK scheme for turbulent Taylor bubble flows in terms of stability so a decision for improved IMEX schemes was taken as presented in [112] which have better stability regions than the best known IMEX multistep schemes over a wide parameter range. Among, the different choices, a second-order scheme was selected which uses a two-stage, second-order diagonally implicit Runge-Kutta scheme (which is stiffly accurate) for the diffusion and a three-stage, second-order explicit RK scheme for the convection. Furthermore, in all simulations $CFL < 0.4$ in each time step was made to ensure stability and fully discretization of the strain tensor was applied.

Last but not least, both linear and midpoint interpolation for the central part of the convective term have been tried. For linear interpolation, a linear distance weighting is used while for midpoint a 50%-50% of weighting is used. For a mesh without stretching, midpoint interpolation is found to be the best choice.

The cylindrical domain with the cell-centered mesh ($DOF = 4 \cdot cells$, i.e. three components of velocity and one for pressure) and the embedded no-slip boundary conditions at the wall are constructed with the modified Navier Stokes Basilisk solver similar to the laminar case that already described in section 3.2. PISO algorithm with two correctors were applied with given tolerance 0.0001.

4.3.4. Averaging strategy

Due to the bubble decay, the simulation of turbulent Taylor bubble flow problem needs to be measured within a specific time interval, otherwise, the simulation is running a different problem since the mass of the bubble is reducing along time. Therefore, the results of this unsteady flow problem have to been post-processed by applying the following averaging procedure for the results to be as accurate as possible:

- Firstly, averaging in time starting after simulation time $1FFT$ such that the flow is fully developed and the adapted inlet velocity has reached a kind of steady value.
- Averaging in space in the circumferential direction (along different angles θ) with interpolation the data to a structured cylindrical mesh.
- Ensemble averaging (4 simulations for each mesh was proven to be enough) with a statistically independent initial velocity field for obtaining converged results since the problem is unsteady.

Overall, the resulting output data from each mesh are presented in an x-r plane.

In addition to the above, use of phase-averaged velocity and fluctuations, i.e. the root mean square (RMS) of velocity components have been applied which are essential for measuring velocity and turbulent kinetic energy in the wake region. The velocity and fluctuation phased-averages are defined in the same way with the reference study of [1] so that a direct comparison can be done for mean gas velocity, mean liquid velocity, mean gas fluctuations and mean liquid fluctuations in all three directions:

$$\mathbf{U_g} = \frac{\overline{a_g \mathbf{U_g}}}{\overline{a_g}} \tag{4.17}$$

$$\mathbf{U_l} = \frac{\overline{a_l \mathbf{U_l}}}{\overline{a_l}} \tag{4.18}$$

$$RMS(\mathbf{U_g}) = \sqrt{\frac{\overline{\left(a_g \cdot \mathbf{U_g} - \overline{a_g \mathbf{U_g}}\right)^2}}{\overline{a_g^2}}} \tag{4.19}$$

$$RMS(\mathbf{U_l}) = \sqrt{\frac{\overline{\left(a_l \cdot \mathbf{U_l} - \overline{a_l \mathbf{U_l}}\right)^2}}{\overline{a_l^2}}} \tag{4.20}$$

, with $a_g = 1 - a_l$ the void fraction which ranges between 0 and 1.

4.3.5. Results

After the conclusions extracted by the preliminary simulations shown in the previous section, simulations with three different meshes (with minimum and maximum levels of refinement 9-10, 10-10 and 10-11 correspondingly) were performed in Basilisk according to the setting described previously. Table 4.5 indicates all simulation data. Regarding cell dimensions, the first layer of cells at the wall has a wall-normal size of roughly from $\Delta y^+ = 4$ to 16 wall units and DNS quality can only be approximated and not be reached. As it was observed even from preliminary simulations in section 4.3.3, the bubble decay at the tail is much less in Basilisk in comparison with [1, OpenFOAM]. In particular, the decay rate is measured as the shifted distance of the tail's point that lies on pipe axis and is computed $0.11D/sec$ (which corresponds to $4,7\%$ loss of initial total volume per second) for the coarsest and $0.016D/s$ (which corresponds to $0,7\%$ loss of initial total volume per second) for the finest mesh in Basilisk while in [1, OpenFOAM] was ranged between $0.4D/s$ (finest) and $1.2D/s$ (coarsest). For this reason, the averaging in time is performed for an interval of $2s$ repeated for 4 simulations for each mesh (ensemble averaging). The total computational time for 4 simulations with the same mesh in Basilisk ranges from around $8K$ (mesh 9-10) to $100K$ (mesh 10-11) CPU hours which can be characterized very low considering the DOF (DOF = amount of cells). Each simulation has been running with 128 cores each and therefore, lasted between 1 and 8 days.

				N_{cells}/D		Δy^+					
Mesh	l_{min}	l_{max}	N_{cells}	**min**	**max**	**min**	**max**	$N_{ensemble}$	T [s]	**CFL**	**Decay rate [D/s]**
9-10	9	10	~950k	32	64	16.6	8.3	4	2.0	0.4	0.11
10-10	10	10	3.5M	64	64	8.3	8.3	4	2.0	0.4	0.057
10-11	10	11	~5.4M	64	128	8.3	4.2	4	2.0	0.4	0.016

Table 4.5: Simulation data for the turbulent co-current Taylor bubble for three different meshes in Basilisk.

A three-dimensional visualization of the liquid axial velocity field and velocity magnitude of the turbulent co-current Taylor bubble flow computed in Basilisk can be seen in figure 4.48 at snapshots every $0.5s$ for simulations with uniform mesh 10-10. The visualization is extracted with the liquid flow upstream of the bubble being fully developed from the beginning of the simulation. In all simulations in Basilisk, bubble's nose is elongated slightly after early steps (before $t = 0.5s$). This can be explained by the oscillations in bubble's position at the beginning due to the small value of the under-relaxation parameter ($\beta = 0.1$) and the variation of the value of total force the bubble accepts since the adaptive inlet velocity needs some time (almost $1FFT$) until a kind of almost steady state is reached for the value of the relative inlet velocity (around $-0.2m/s$). Despite the nose's elongation, turbulent pipe flow upstream is not affected that much from the presence of the bubble even for distances close to the nose. Therefore, the safety margin (after $\pi \cdot D$) upstream the bubble can be even smaller than $0.5\pi \cdot D$. Moreover, the wake behind the bubble can be observed with a positive value of the velocity near the pipe axis and very negative in the thin liquid film near the wall. It can be observed that the decay rate is very low (i.e. $0.057D/sec$) along time. The wake length seems somewhat constant in all snapshots. Some of the small bubbles that break up from the main bubble move away with the liquid flow while most of them are recirculated due to the toroidal vortex in the wake and may merge back to the bubble.

Figure 4.49 indicates a cross-section view of the ensemble (4 simulations), time ($t = 2s$), and space (in the circumferential direction) averaging of void fraction along the pipe axis for the three different meshes. Similar to what is concluded from the calculated values of the decay rate, the mean void fraction shows similar behavior in all three meshes. This verifies that the time interval of $t = 2s$ and the ensemble averaging of 4 simulations is enough such that the resulting mean void fraction is (almost) mesh-independent. A small instant deviation of mesh 10-10 at the cross-section passing through the bubble's tail can be explained by the uniform mesh and the use of adaptive function in meshes 9-10 and 10-11 near the gas-liquid interface. Whenever the adaptive function is used in the cells near the tail, it suppresses the value of void fraction by interpolating back-and-forth. This interpolation results in a damping of the void fraction in this area. The use of dynamically refined mesh near the interface and in particular near bubble's tail is visible in the next two figures (4.50 and 4.51).

Figure 4.50 indicates two 2D consecutive void fraction's snapshots as extracted from Paraview with mode "surface with edges" for the simulation with refinement levels $9 - 10$. The top sub-figures (4.50a

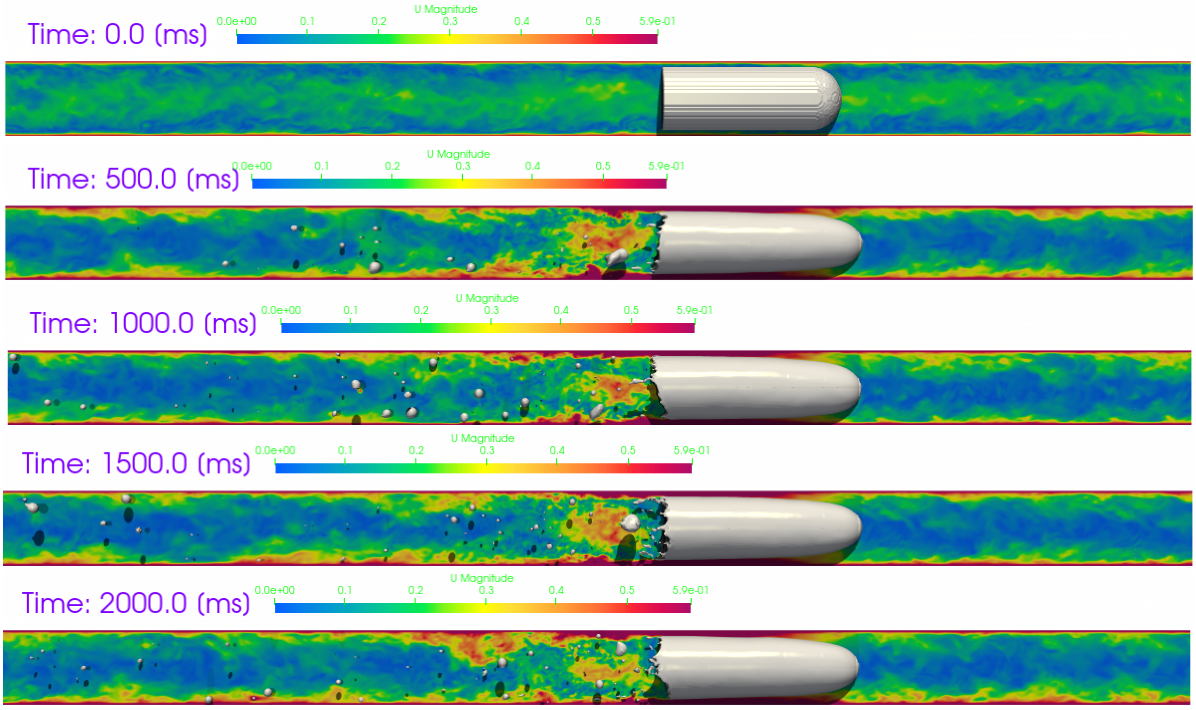

(a)

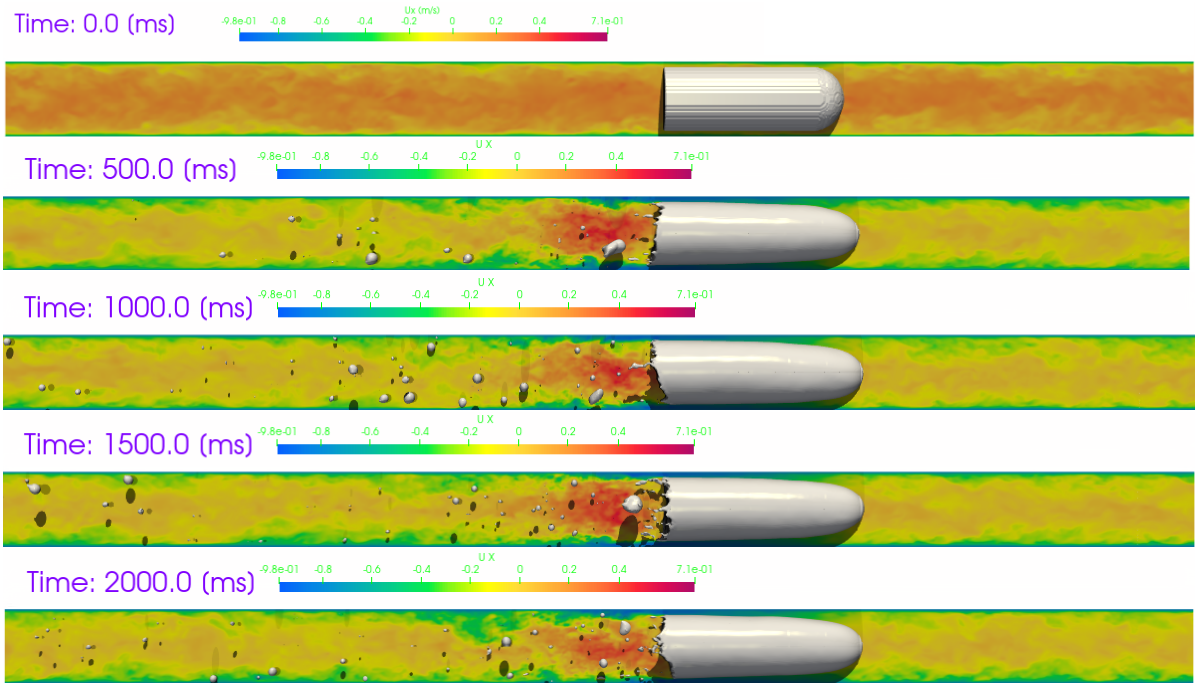

(b)

Figure 4.48: Time evolution of magnitude (4.48a) and streamwise (4.48b) velocity for simulation with mesh 10-10.

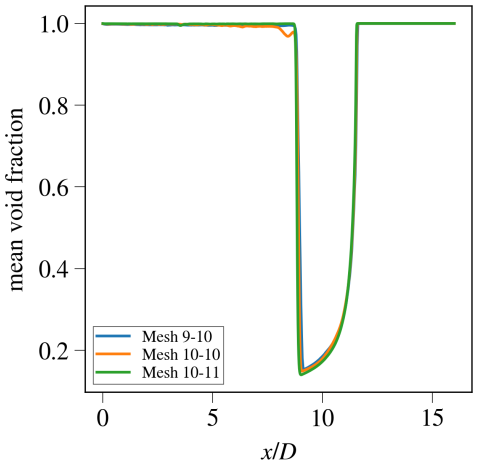

Figure 4.49: Cross-section view of the ensemble, time and space averaging of void fraction along the pipe axis for the three different meshes (9-10, 10-10 and 10-11) in Basilisk.

and 4.50b) illustrate all pipe domain around the bubble while the sub-figures at the bottom (4.50c and 4.50d) indicate a zoom of the top sub-figures across the half bubble's tail. During the transition from $t = 1.9s$ to $t = 2s$, some coarser cells (approximately just after the vertical plane at $x = 0.126$) are splitted into $2^3 = 8$ (i.e. in all three directions) smaller cells due to the mesh refinement at the interface from level 9 to level 10 while some other finer cells (approximately just before the vertical plane at $x = 0.126$) are merged in groups of $2^3 = 8$ as explained in 3.1.

The space, time and ensemble-averaged qualitative results in Basilisk are indicated in figure 4.51. Starting from the simulations coarsest mesh (9-10) at the top sub-figure and ending at the simulation with the finest mesh at the bottom, each sub-figure illustrates the cross-section image of streamline contours, bubble's shape and the streamwise component of velocity scaled by actual Taylor bubble velocity for an MFR attached to the bubble. In all cases, a toroidal vortex appears both within the bubble and in the wake. Although the toroidal vortex within the bubble shows similar behavior in all cases, the vortex at the wake region is larger for the coarsest mesh 9-10 (top figure) and extends at $3D$ length, the region in which higher axial velocity appears. A small area of overlapping of the two vortices is observed in each case which is larger in the coarsest grid and this explains why it results in bigger bubble decay. Moreover, the average shape of the tail seems very sensitive to the selection of mesh since it ranges from flat at meshes 9-10 and 10-11 to slightly concave at mesh 10-10. This difference between uniform and non-uniform meshes is something that was already observed in figure 4.49 and can be explained by the use of the adaptive function near the gas-liquid interface which results in slightly different tail curvature.

Comparing with the reference study of [1, figure 10, OpenFOAM], simulations in Basilisk illustrate a smaller area of overlapping of the two vortices and as a consequence, much less bubble decay along time. The length of the vortex in the wake in [1, figure 10, OpenFOAM] was found to be shorter than Basilisk for coarser meshes. Furthermore, the curvature of the tail was found to be concave in all examined grids while the shape of the tail in Basilisk seems to be mesh-dependent and affected by the use of adaptive function in non-uniform meshes. However, the time-averaging in simulations of [1, figure 10, OpenFOAM] was implemented for much smaller window (ranging from $1FFT$ to $3FFT$) while all simulations in Basilisk was averaged for $2s$ since simulations in [1, figure 10, OpenFOAM] was by far more mesh-dependent than Basilisk.

Next, a direct quantitative comparison is done between Basilisk and reference studies of [3] and [1, OpenFOAM] regarding the axial and radial velocity in the wake behind the bubble. Figure 4.52 indicates the computed axial (4.52a,4.52b,4.52c) and radial (4.52d,4.52e,4.52f) velocity scaled by the relative velocity in Basilisk [3, experiments] and [1, figure 13, OpenFOAM] at radial cross-section profiles at distances $0.6D$ (left), $1D$ (middle) and $2D$ (right) behind the tail. In general, there is good agreement between Basilisk and [1, figure 13, OpenFOAM] for the axial velocity at the wake except for a small overestimation of simulation mesh 9-10 in Basilisk at distance $2D$ from the tail due to the estimated

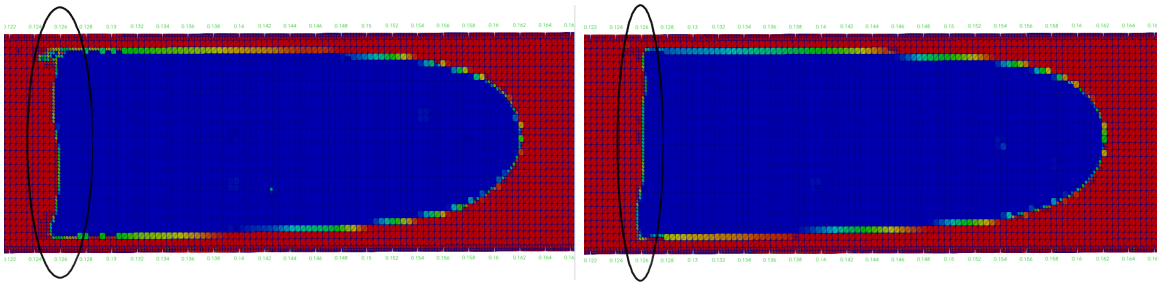

(a) $t = 1.9s$

(b) $t = 2s$

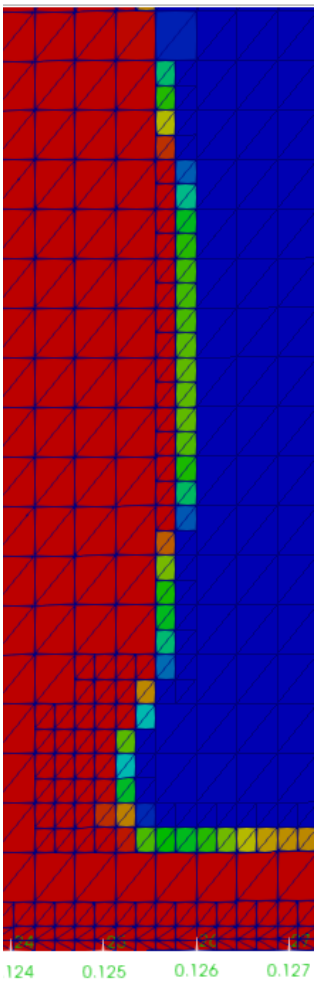

(c) zoom of 4.50a across the half bubble's tail in $t = 1.9s$

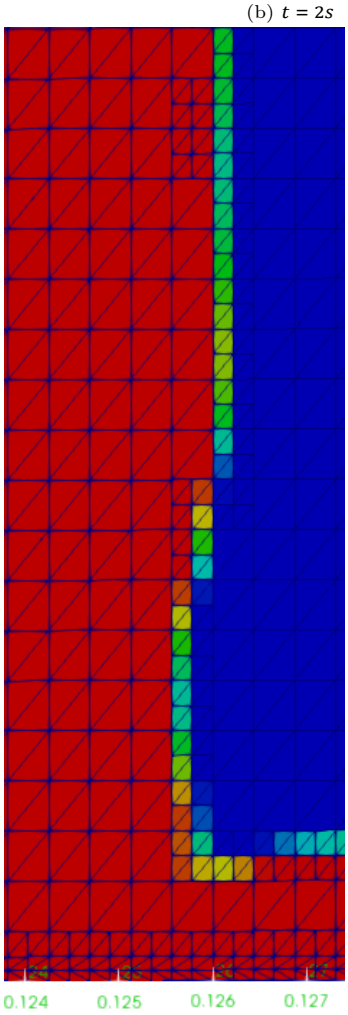

(d) zoom of 4.50b across the half bubble's tail in $t = 2s$

Figure 4.50: Void fraction's snapshots of simulation with adaptive mesh. Refinement levels 10 near the interface and along pipe wall and 9 everywhere else. Blue color for gas and red for liquid.

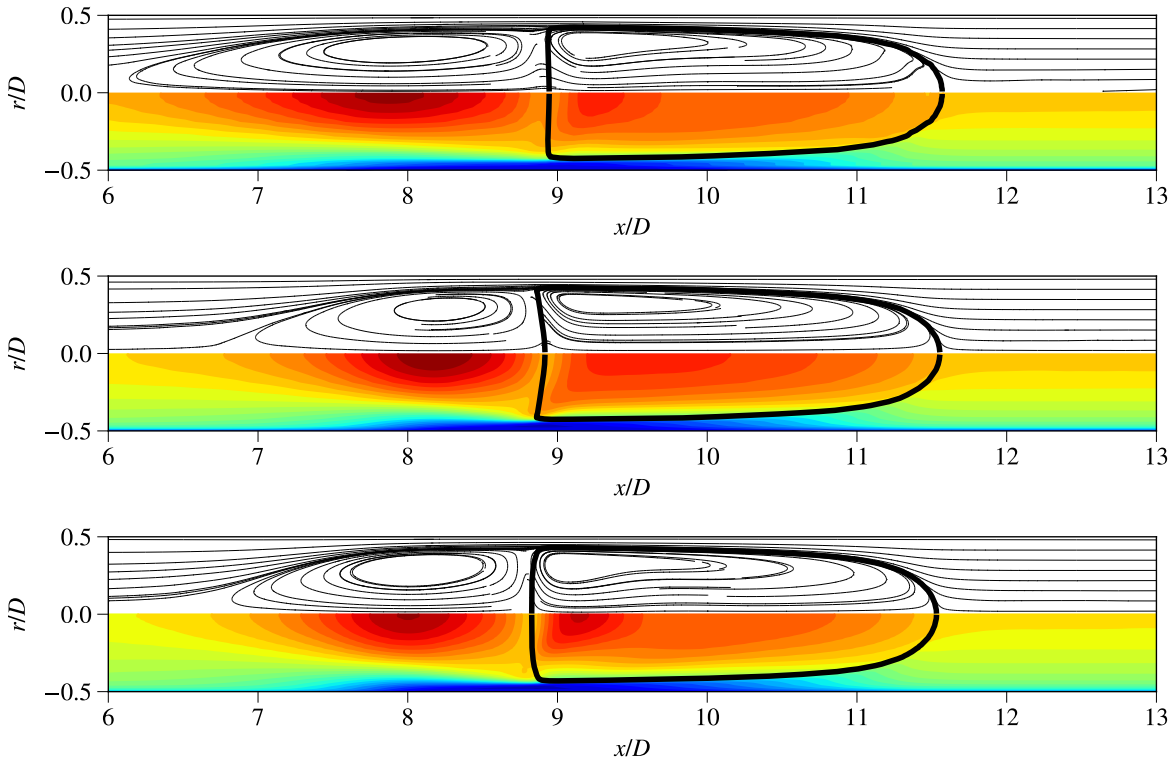

Figure 4.51: Space, time and ensemble-averaged streamline contours (top half of each figure) and axial component of velocity scaled by actual Taylor bubble velocity for an MFR attached to the bubble (bottom half of each figure) for the three meshes (9-10 top, 10-10 middle, and 10-11 bottom figure). The color map ranges from -1 (dark blue) to 1 (dark red). The interface of the Taylor bubble (black line) at f = 0.5.

length of the wake. Regarding the radial velocity profiles, predictions from the two finest meshes in Basilisk match with those of [1, figure 13, OpenFOAM], except at distance $1D$ where weaker radial velocity in Basilisk is observed due to longer wake length. On the other hand, experiments of [3] result in smaller wake so there is a small deviation from simulations in both axial and radial velocity at almost all distances but with the same trend and extreme values.

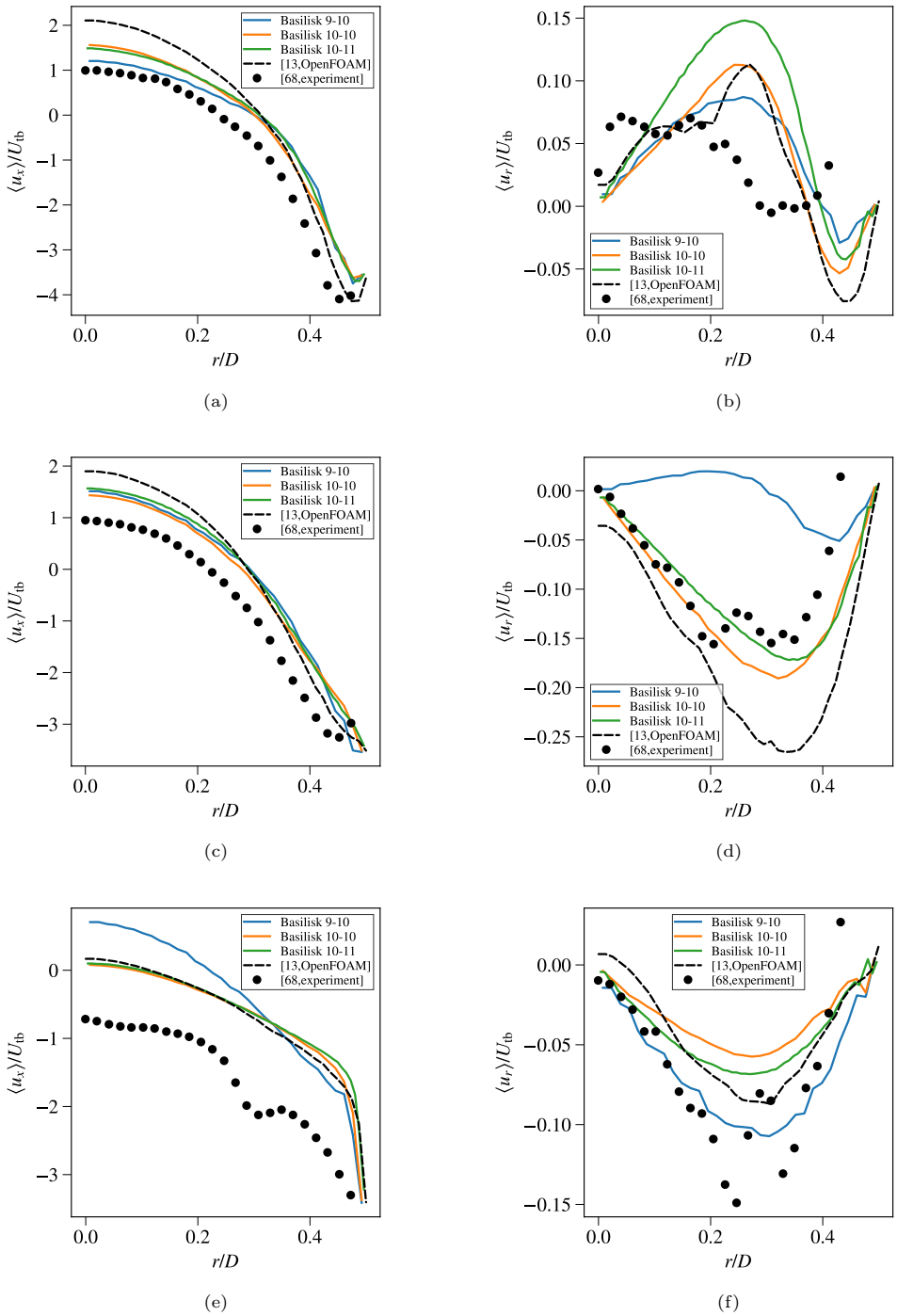

Figure 4.52: Averaged axial (left) and radial (right) velocity for different meshes in Basilisk at distances $0.6D$ (top), $1D$ (middle) and $2D$ (bottom) downstream the bubble's tail and comparison against [3] and [1, figure 13, OpenFOAM].

Figure 4.53 illustrates the scaled velocity fluctuations in axial and radial directions at the same cross-section radial profiles and distances. RMS of velocity in each direction is calculated according to

equation 4.19 and the comparison is done again against the reference studies of [3] and [1, figure 14, OpenFOAM]. Although simulations in [1, OpenFOAM] illustrate much larger bubble's decay rate, the predictions of simulation with meshes 10-10 and 10-11 in Basilisk are in favor of the results of [1, figure 14,OpenFOAM] in both radial and velocity fluctuations. However, the predicted velocity fluctuations from both software are underestimated compared to the experimental values of [3].

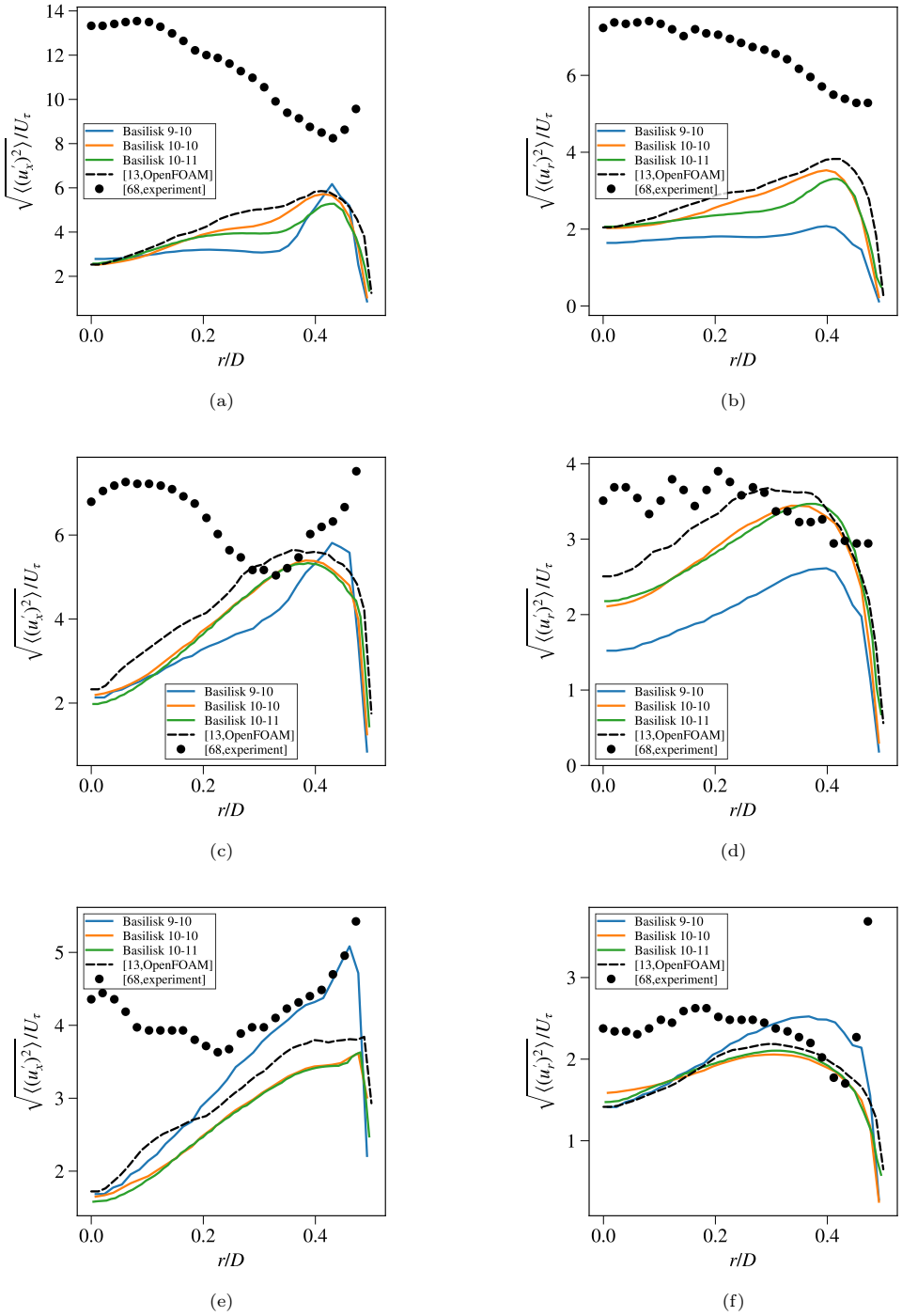

Figure 4.53: RMS of averaged axial (left) and radial (right) velocity for different meshes in Basilisk at distances $0.6D$ (top), $1D$ (middle) and $2D$ (bottom) downstream the bubble's tail and comparison against [3] and [1, figure 14, OpenFOAM].

5

Influence of pipe diameter and bubble length on Taylor bubble flows

The validation cases demonstrated in chapter 4 (i.e laminar bubble flow, laminar Taylor bubble flow, and turbulent co/counter-current Taylor bubble flow) indicate that the developed Basilisk code produces results that are in very good agreement with the published literature and with a low computational cost. In this chapter, the study of Taylor bubble flow is extended to the cases in which the liquid flows in the direction of gravity and counter-acts the movement of the Taylor bubble. This flow problem is known as the counter-current Taylor bubble flow.

The simulations are performed in Basilisk in both laminar and turbulent counter-current Taylor bubble flow using the experimental setting of [5]. The objective of these simulations is to investigate the influence of the pipe diameter and the bubble's length on the Taylor bubble flow and in particular, on the bubble decay rate and the gas-liquid interface. For this reason, the same setting, flow parameters, and discretization methods are used in both laminar and turbulent flow with the only difference the value of pipe diameter (which affects Re, Mo, Eo numbers) which is set to $D = 1.24cm$ for laminar and $2.6cm$ for turbulent flow. To check the effect of bubble length, three different values of bubble lengths have been chosen common in both laminar and turbulent flow: $2D$, $4D$ and $6D$.

5.1. Simulation strategy

Table 5.1 indicates the values of the flow parameters that depend on the value of the pipe diameter and therefore, are different between the laminar and turbulent counter-current Taylor bubble flow. The interfacial forces are much stronger than the viscous forces (very small Mo) while the Reynolds number changes from $Re = 2200$ to $Re = 5600$. Although the liquid flow is still laminar upstream the bubble in the simulations with the small pipe diameter, becomes semi-turbulent at the wake so a fully 3D simulation has been implemented in Basilisk since the goal is to capture the volume of bubble disintegration as accurately as possible. Water and air at a temperature of 30^oC are the selected fluids for this two-phase flow problem.

Table 5.1: Flow properties of laminar and turbulent counter-current Taylor bubble flow used in Basilisk simulations taken from experiments of [5].

Parameter	laminar	turbulent
Pipe diameter D	$0.0124m$	$0.026m$
Initial bubble length L_b	$2D$ / $4D$ / $6D$	$2D$ / $4D$ / $6D$
Bulk Reynolds number Re_{bulk}	2200	5600
Eötvös number Eo	21	92
Morton number Mo	$1.1 \cdot 10^{-11}$	$1.1 \cdot 10^{-11}$
Froude number Fr	0.4	0.34

Since bubble rising velocity is on the opposite direction of the liquid velocity, a non-moving frame of

reference (NMFR) has been selected in Basilisk. Depending on the value of the inlet liquid flow (which creates a force that counteracts buoyancy), the bubble may move upward, downward, or stay at an almost fixed position. The idea of simulations in Basilisk is to have an adapted axial inlet flow which is balanced by buoyancy and therefore, make the bubble remain at a fixed position ($u_{tb} = 0$). Therefore, the simulation strategy of counter-current Taylor bubble flow looks similar to the one described and used for turbulent co-current Taylor bubble flow (section 4.3.2) with an MFR attached to the bubble where for $U_{bulk} < U_{tb}$ the simulation setup was converted to a counter-current Taylor bubble flow problem. Thus, equations 4.9, 4.8 can fully describe the simulated Taylor bubble flow. However, since the wall is stationary in an NMFR, equation 4.14 is replaced in each time step by:

$$u_{wall} = 0 \tag{5.1}$$

Apart from that, the simulation setup for both flows is similar to the one described in section 4.3.2). Two single-phase pipe flow simulations (one for laminar and one for turbulent) were initially carried out in Basilisk for $t = 6sec$ with the same flow parameters as in two-phase flows and their final velocity profile were used as the initial liquid velocity profile of Taylor-bubble simulations so that each two-phase Taylor bubble flow simulation starts with a fully laminar/turbulent developed flow. Moreover, the inlet velocity profile is adapted by the actual Taylor bubble velocity and also recycled by taking the streamwise cross-section velocity profile at distance πD from the inlet so that the resulted inlet velocity is not a plug flow (equation 4.15 with under-relaxation parameter is chosen $\beta = 0.1$.).

Figures 5.1a and 5.1b illustrate the simulation setup used in Basilisk for laminar and turbulent counter-current Taylor bubble flows respectively. For all choices of bubble length, the simulation setup is the same with pipe length equal to $L = 16D = 0.1984m$ for laminar and $L = 16D = 0.416m$ for turbulent flow and initial bubble width $D_b = 0.85D$.

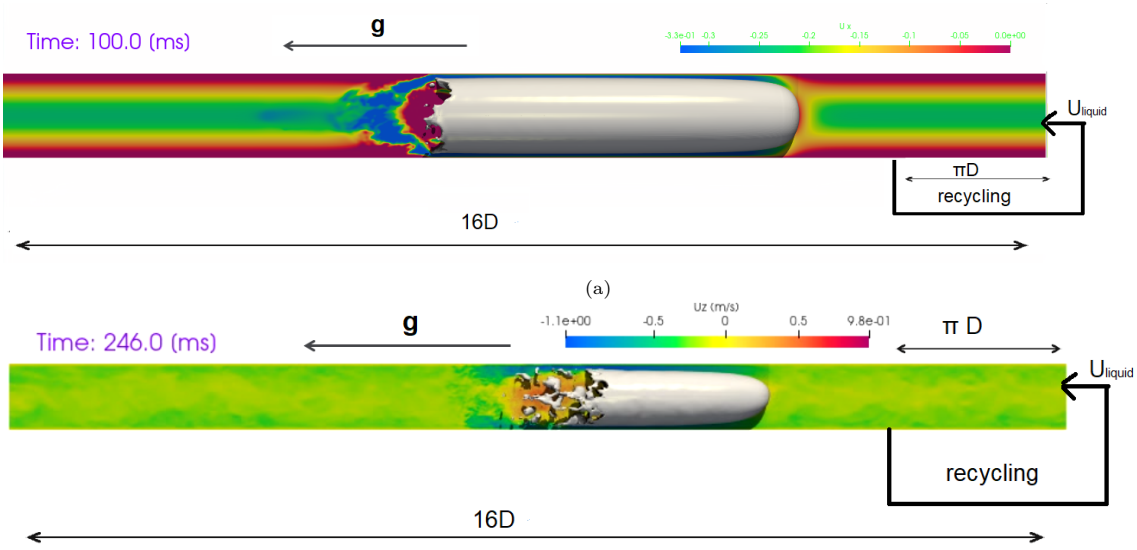

Figure 5.1: Simulation setup for an NMFR used in all simulations of laminar (5.1a) and turbulent (5.1b) counter-current Taylor bubble flow.

Since the target is to capture the average bubble decay as accurately as possible, all simulations have been performed for $t = 10s$ using a uniform mesh with refinement level 10 everywhere which results in constant mesh size $h = L/2^l = 0.1984/2^{10} = 0.19375mm$ for laminar and $h = L/2^l = 0.416/2^{10} = 0.4mm$ for turbulent flow. This ends up at $3.5M$ cells (and DOF) for both flows. The modified N.S solver has been applied in Basilisk as described in section 3.2 using the volume penalization method for the smooth damping of velocity near the wall. Crank-Nicolson has been used for the temporal discretization to minimize the computational time while the linear scheme is used for spatial discretization everywhere in the domain except in the cells near the interface where the minmod flux limiter is applied to the convection term. Moreover, the CFL number is set less than 0.4 in each time step to ensure stability. Last but not least, only one simulation per bubble length is performed for $t = 10s$ so averaging

only in time and space (in the circumferential direction) is applied (not ensemble) together with the interpolation of the data to a structured cylindrical mesh.

5.2. Laminar counter-current Taylor bubble flow

Figure 5.2 illustrates a three-dimensional visualization of the streamwise velocity field and its evolution along time for all three simulations. In particular, sub-figure 5.2a shows the evolution (by taking snapshots every $2.5s$) of the simulation with initial bubble length $2D$ while sub-figures 5.2b and 5.2c show the velocity field for the simulations with initial bubble length $4D$ and $6D$ correspondingly. It can be easily observed that in all cases, the majority of the bubble decay occurs between $t = 0$ and $t = 2.5s$ while after that, the rate of bubble decay is somehow similar to the rate that the bubble gains gas by merging back some of the bubbles that have been detached. Moreover, most of the detached bubbles seem to be trapped in the wake while only a few are transported away of the pipe domain by the laminar liquid flow.

Figure 5.3 illustrates the cross-section view of streamline contours, bubbles shape and the axial component of velocity averaged in time (for an interval of $t = 10s$) and space (in the circumferential direction) for all three simulations of laminar counter-current Taylor bubble flow. Two toroidal vortices appear in all simulation cases: one at the wake region behind the bubble of length $1D$ and one within the bubble. Although the length of each vortex seems to be independent of the initial bubble length, the average curvature of the tail is ranging from flat with a trend to convex for the shorter bubble to flat with a small trend to concave for the longer bubbles. Moreover, the toroidal vortex within the bubble is stronger for the longest bubble and weaker for the shortest.

The critical value for which the force created by the adapted axial inlet flow reaches an almost steady-state and is balanced by buoyancy so that the bubble remains at a fixed position ($u_{tb} = 0$) is found to be on average around $u_{inlet} = -0.085m/s$ in Basilisk. The value of the streamwise component of the inlet velocity seems independent of the choice of the bubble length as indicated in figure 5.9 and is achieved $0.05sec$ after the beginning of the two-phase flow. After this time, the streamwise component of the inlet velocity is fluctuating up to $0.01m/s$ around the (almost) steady critical value. The equilibrium happens so early because the bubble was initialized in a fully developed laminar flow (i.e. was restarted from single-phase flow). For bigger (absolute) value than the critical of inlet liquid flow, the bubble is moving at an NMFR in the direction of the liquid flow while for smaller values the buoyancy is overcoming the liquid flow and the bubble is moving up.

Like [5] observed experimentally, the choice bubble length does not influence on the (almost) steady inlet flow. However, there is an underestimation of around 30% of the value indicated in [5]. This may happen because the thickness of the boundary layer in Basilisk seems bigger than the thin liquid film between the bubble and the pipe wall which affects the almost steady value of the adapted inlet while in experiments, the width of the boundary layer is often cut artificially upstream the bubble such that it does not affect the flow.

Three instant gas volumetric flow rates at different pipe cross-sections are illustrated in figure 5.5. All three pipe cross-sections are placed far downstream of the bubble and near the output (liquid flow is coming from the negative direction), i.e. figure 5.5a shows the gas volumetric rates at $x = 2D$, figure 5.5b at $x = D$ and figure 5.5c at $x = 0.5D$. The choice of the pipe cross-sections has been made such that each of them is outside the wake region for all bubble lengths. The wake length has been computed around $1D$ in all simulations (5.3), which is three times less than the axial distance between the tail of the longer simulated bubble (i.e. $6D$) and the first measured cross-section ($x = 2D$ at sub-figure 5.10a). However, some instant negative (i.e. opposite to the direction of the liquid velocity) flows are observed especially at the two cross-sections closer to the wake (at $x = 1D$ and $x = 2D$), which means that some instant recirculations of the detached bubbles still exists far away from the wake. To be able to make a direct comparison, a time-shifting is necessary because the tail of the longer bubble is closer to the cross-sections than the others. Therefore, the time starts ($t = 0$) from the time point in which the void fraction at the specific cross-pipe section is non-zero for each simulation (bubble length $2D, 4D, 6D$), i.e. the first detached bubbles are passing from this cross-section. No big differences in the gas volumetric flow rates along time can be observed between the various bubble lengths.

Figure 5.6 indicates the ratio of the initial bubble volume that has left the domain along shifted time (with the same post-processing procedure described before) for all three simulations of laminar counter-current Taylor bubble flow. The volume of gas that exits the domain is very low for two reasons.

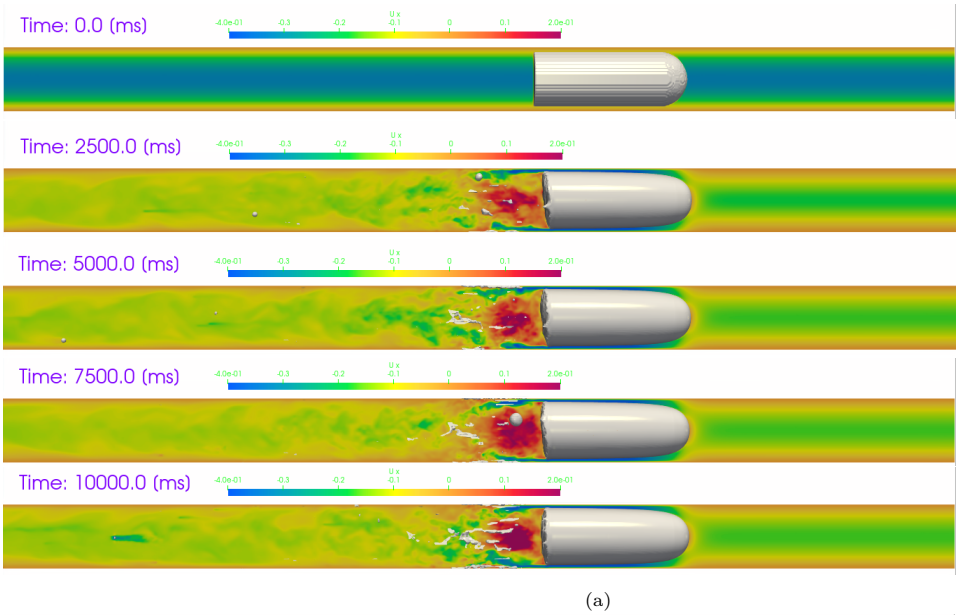

(a)

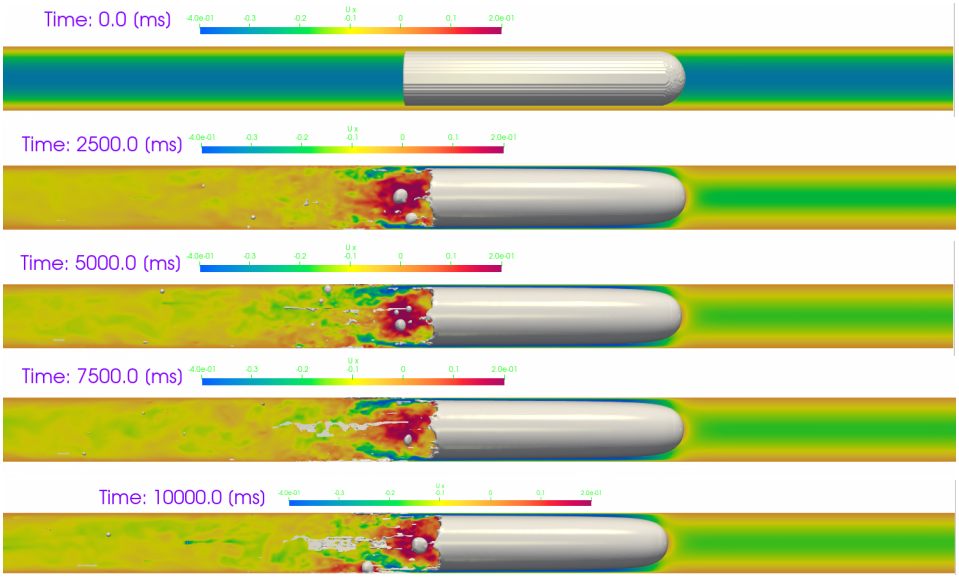

(b)

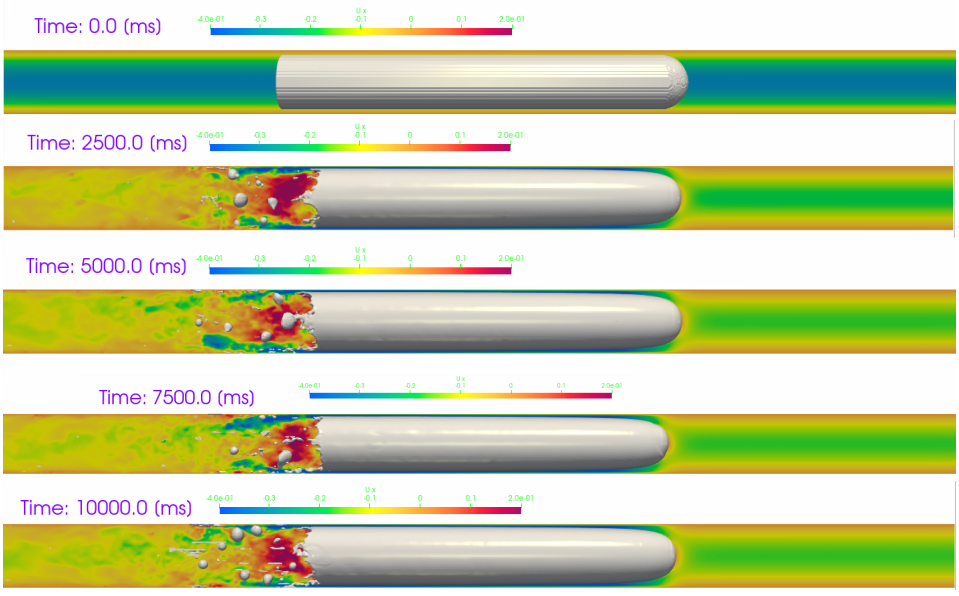

(c)

Figure 5.2: Time evolution of liquid streamwise velocity and bubble behaviour for simulations of laminar counter-current Taylor bubble flow with initial bubble length $2D$ (5.2a), $4D$ (5.2b) and $6D$ (5.2c).

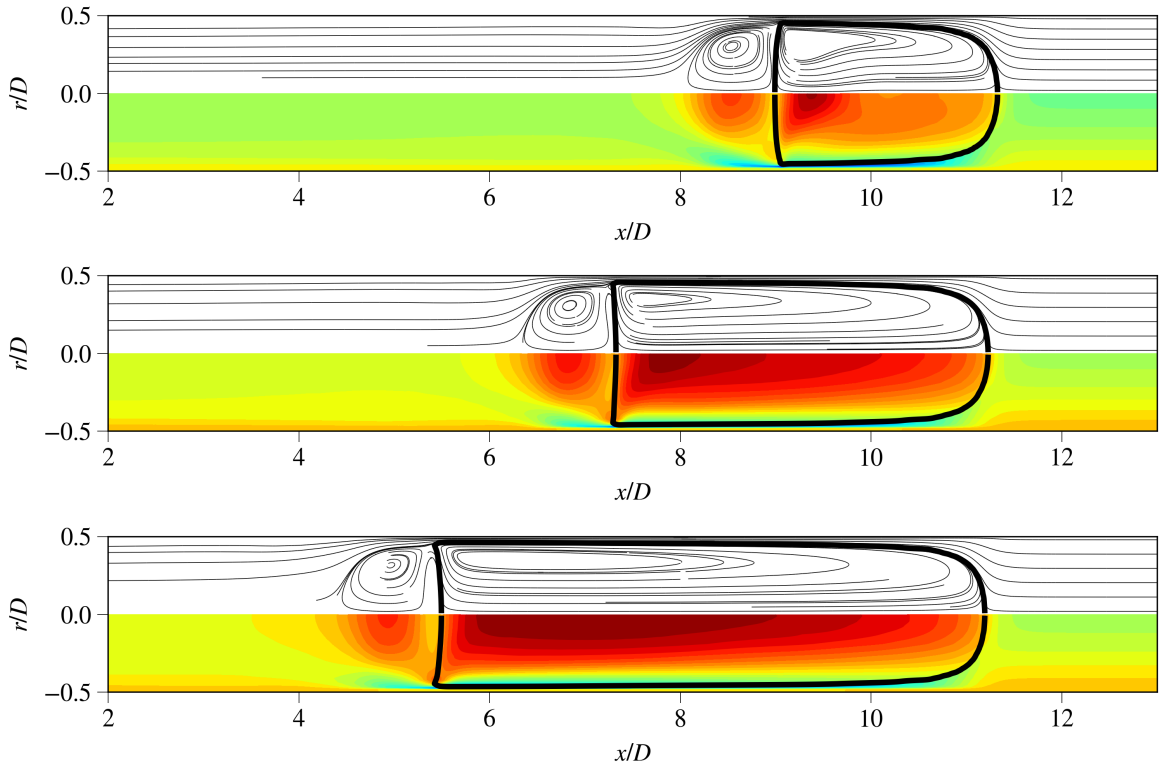

Figure 5.3: Space and time-averaged streamline contours (top half of each figure) and axial component of velocity scaled by Taylor bubble velocity (bottom half of each figure) for the three simulations of laminar counter-current Taylor bubble flow with different initial bubble length ($2D$ top, $4D$ middle, and $6D$ bottom figure). The color map ranges from -1 (blue) to 1 (dark red). The interface of the Taylor bubble (black line) at f = 0.5.

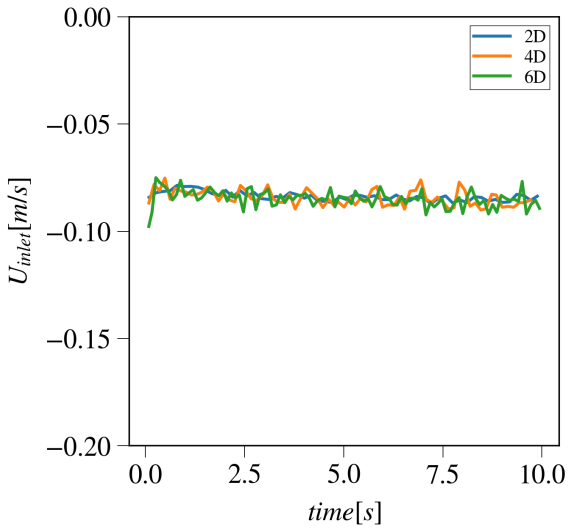

Figure 5.4: Value of adapted streamwise velocity at the inlet along time for three simulations with different initial bubble lengths in laminar counter-current Taylor bubble flow.

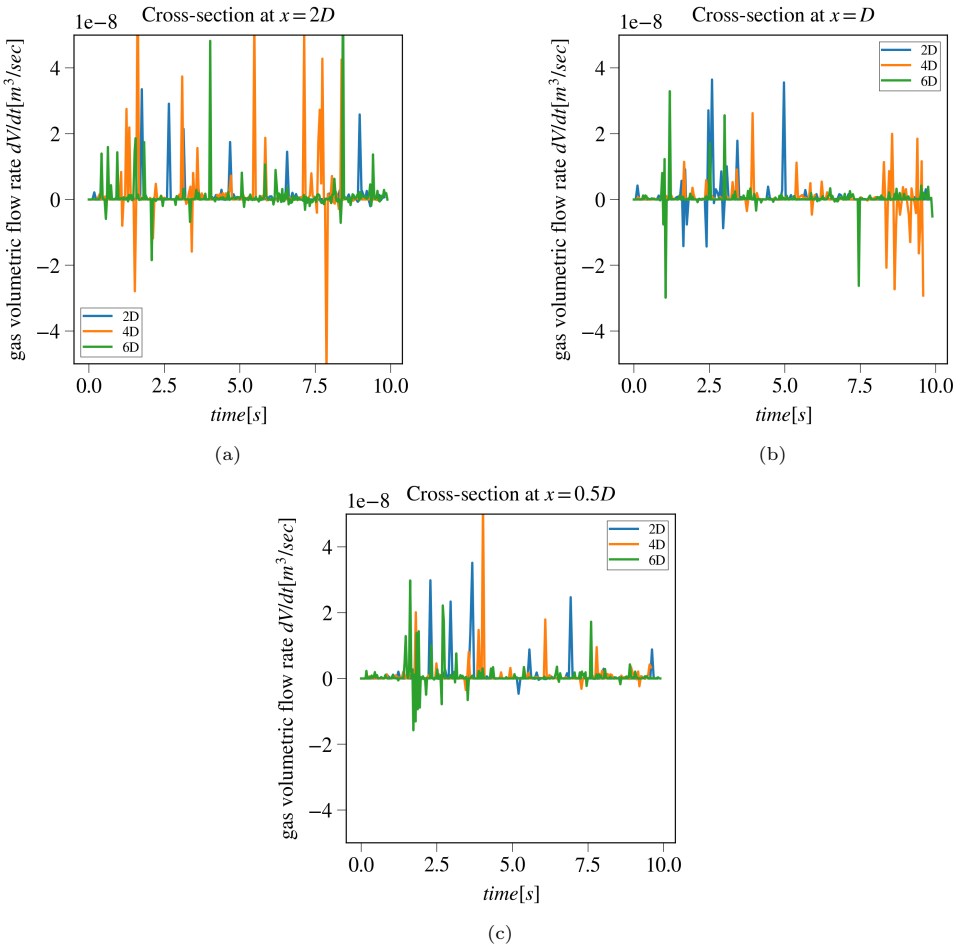

Figure 5.5: Instant gas volumetric flow rates at three different pipe cross-sections downstream the wake along shifted time in laminar counter-current Taylor bubble flow. Time starts when the first detached bubble is passing from each cross-section for each simulation case.

Firstly, the flow downstream the bubble is very weak and secondly, Eo is quite big in the laminar flow which means that the interfacial forces are strong resulting in less loss of void. Therefore, the ratio of the initial bubble volume that has been lost is smaller for larger bubbles in the laminar flow even though the loss of void is almost the same in absolute values for all simulations (since the initial bubble volume of bubble with length $6D$ is almost three times greater than the one of $2D$).

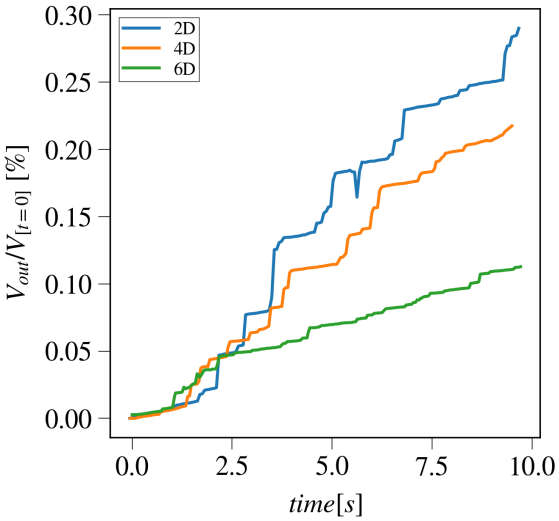

Figure 5.6: Cumulative percentage of the initial bubble volume that has been detached and transported outside the domain by the liquid flow within the $t = 10s$ for different bubble lengths in the laminar counter-current Taylor bubble flow. Time starts when the first detached bubble is passing from each cross-section for each simulation case.

5.3. Turbulent counter-current Taylor bubble flow

The three-dimensional visualization of the evolution axial liquid velocity field of the turbulent counter-current Taylor bubble flow can be seen in figure 5.7. Sub-figures 5.7a, 5.7b, 5.7c indicate the streamwise velocity field at snapshots of $2.5s$ for each simulation case. Similar to what was observed in the laminar counter-current case in section 5.2, the most significant bubble decay is noticed during the first $t = 2.5s$ in all cases. After that, the detached gas volume from the bubble's tail is of a similar order of magnitude with the gas volume attached to the tail. Another interesting observation is the fact that the bubble not only oscillates back and forth from in the axial direction (due to the adapted inlet) but also in the radial direction as well. This is in contract to the turbulent co-current flow in which the bubble was oscillating only in the axial direction (section 4.3). The trend of this movement of the bubble to the radial direction wall happened not suddenly but gradually (started slightly to appear around t=4s) and is neither continuous nor constant. However, this wobbly behavior of the Taylor bubble is also observed in [5] and affects the the length and behavior of the wake. For example, in the case of a bubble with initial length $2D$, the center of mass of the bubble seems closer to the pipe wall from the "upper" side (in two-dimensional representation) at $t = 5s$ while it moves again to the pipe axis at $t = 7.5s$ before it ends up near the "bottom" side wall (in two-dimensional representation) at the final time. In general, after careful attention to the bubble's evolution, it can be concluded that this radial movement starts happening after $2 - 3s$ and it gradually continues as time goes.

The fact that this radial movement is instant and random (in the sense that it is not in favor of a specific side of the cylindrical pipe wall) can be verified from figure 5.8 which shows the bubble's position, the scaled streamwise velocity and streamline contours averaged in time (for $t = 10s$) and space (in the circumferential direction) for each simulation. The toroidal vortex at the wake is of length $1.5D$ for all bubbles while the vortex that appears within the bubble is stronger for the longest bubble as predicted for the laminar case in section 5.2. However, opposite the laminar case, the choice of the bubble's length seems independent of the curvature of the tail in the turbulent counter-current case. In particular, all simulations show a flat tail with a trend to concave for the part of the tail closer to the wall.

The streamwise component of the inlet adapted velocity along time for each simulation is indicated in figure 5.9. The mean value of the axial adapted inlet velocity is found to be around $-0.16m/s$ independent of the choice of the bubble length. Of course, since the flow is turbulent, the inlet adapted value never reach a steady state but $0.1s$ after the beginning of the flow (i.e. restart of single-phase flow with bubble initialization), the value of the inlet streamwise velocity is fluctuating only up to $0.2m/s$ around the mean value. Similar to what is expected from the laminar counter-current Taylor bubble flow (section 5.2), no significant difference is observed between the simulations with different initial bubble length, so it can be concluded that the choice of bubble length does not affect the value of the adapted inlet, something that is also observed in the experiments of [5]. The predicted mean value of the inlet velocity in Basilisk is slightly underestimated compared to the experiment of [5] ($-0.17m/s$). However, the underestimation in turbulent counter-current Taylor bubble flow is much less than the laminar case and approaches only 7% which is within the tolerance limits given by [5].

Similar to what has been done in figure 5.5 for laminar counter-current Taylor bubble flow, the instant gas volumetric flow rates at three different pipe cross-sections are presented in figure 5.10. Figure 5.10a indicates the gas volumetric flow rates at $x = 2D$, figure 5.10b at $x = D$ and figure 5.10c at $x = 0.5D$. The wake length in the turbulent counter-current Taylor bubble flow has been computed around $1.5D$ in all simulations (5.8), which is half than the axial distance between the tail of the longer simulated bubble (i.e. $6D$) and the first measured cross-section ($x = 2D$ at sub-figure 5.10a). Again, a time-shifting is applied and for each simulation, the time starts ($t = 0$) from the time point in which the first detached bubbles are flowing through each pipe cross-section. The simulation with the longest bubble shows greater values of flow rates because the longer bubble results in more loss of void. Moreover, the cross-sections (mainly the first one, i.e. (5.10a)) of the longest bubble are closer to the wake region than the rest and even though the average wake length is $1.5D$, some recirculation is still observed.

The cumulative ratio of the initial bubble volume that has left the pipe domain along shifted time (with the same post-processing procedure described before) is illustrated in figure 5.11 for all three simulations of turbulent counter-current Taylor bubble flow. Even though the time has been shifted, the cumulative gas volume which exits the domain seems dependent on the bubble's length. In particular, the largest ratio (1.06%) is observed for the longest bubble (i.e. $6D$) in such a strong turbulent counter-

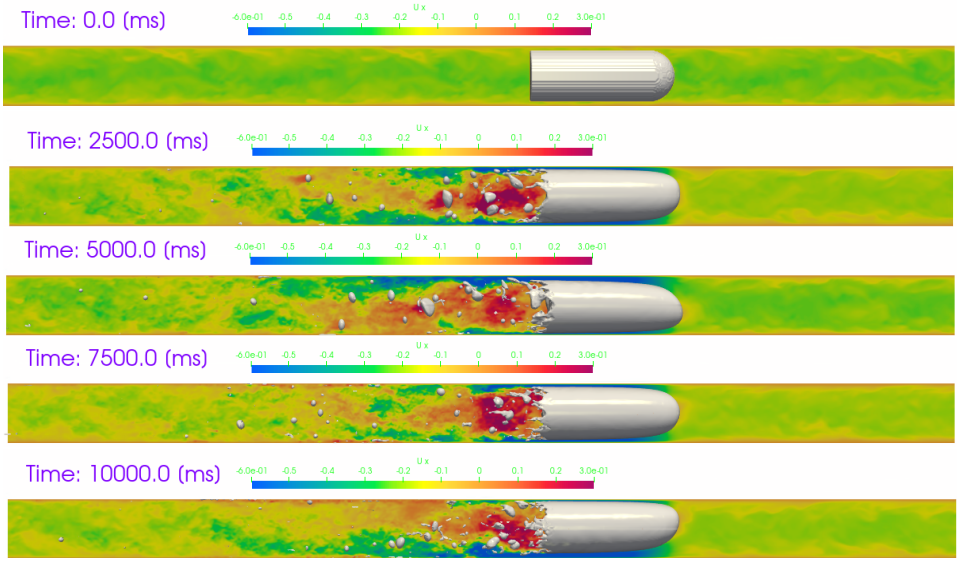

(a)

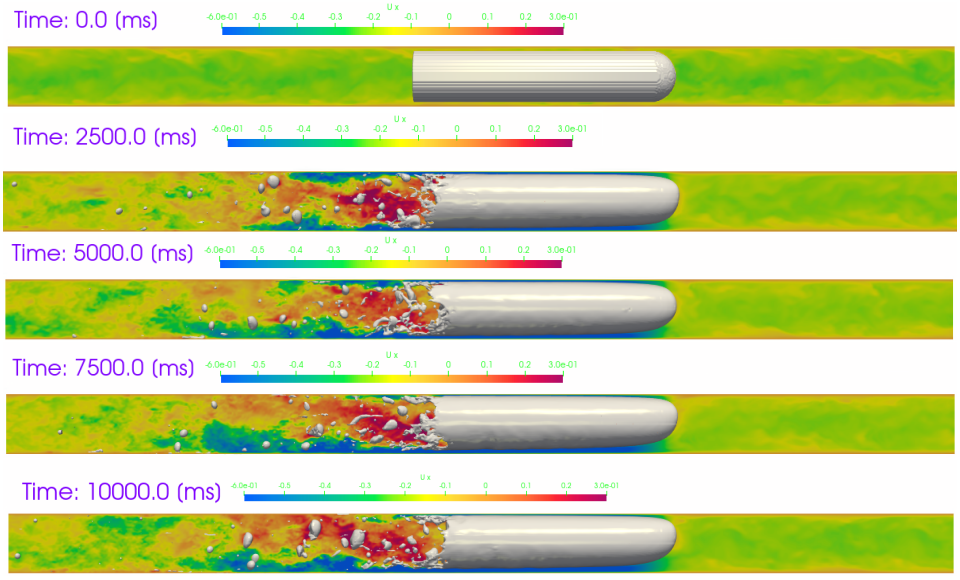

(b)

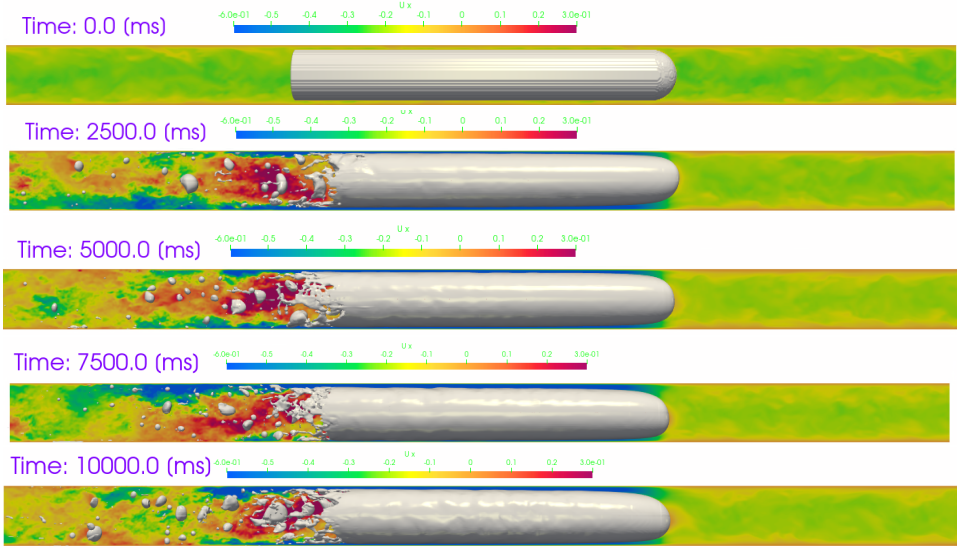

(c)

Figure 5.7: Time evolution of liquid streamwise velocity and bubble behaviour for simulations of turbulent counter-current Taylor bubble flow with initial bubble length $2D$ (5.7a), $4D$ (5.7b) and $6D$ (5.7c).

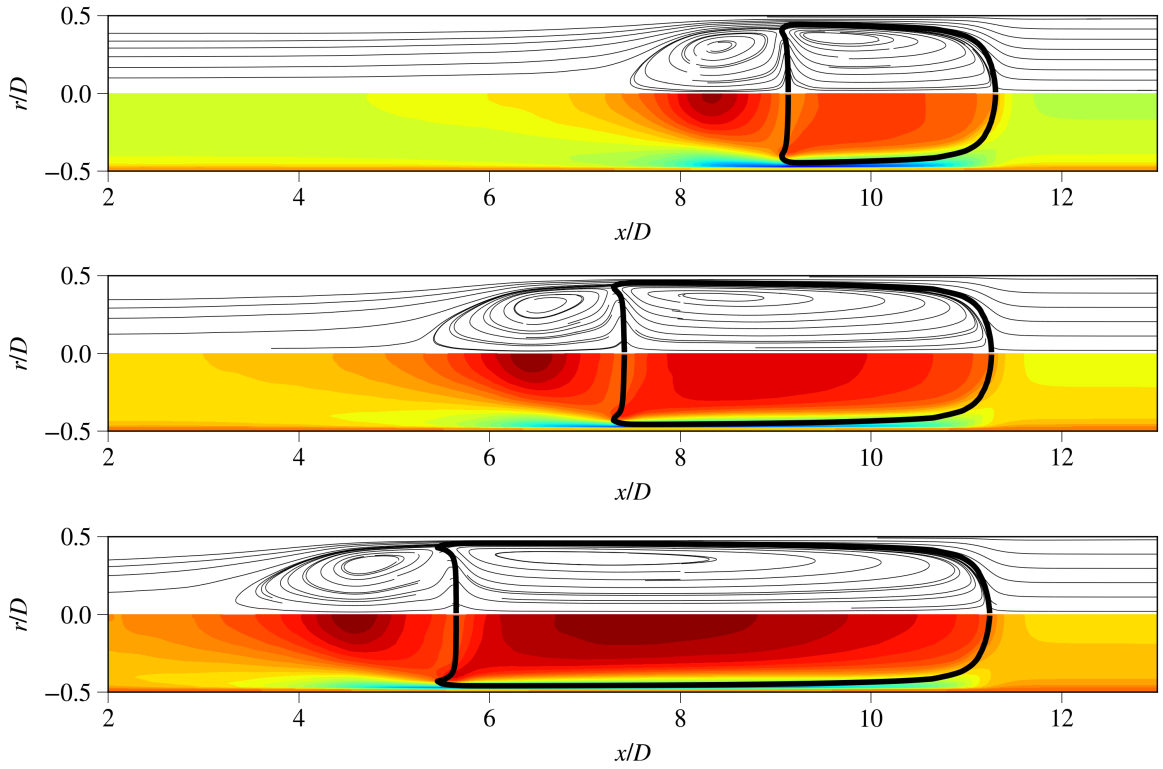

Figure 5.8: Space and time-averaged streamline contours (top half of each figure) and axial component of velocity scaled by Taylor bubble velocity (bottom half of each figure) for the three simulations of turbulent counter-current Taylor bubble flow with different initial bubble length (2D top, 4D middle, and 6D bottom figure). The color map ranges from -1 (dark blue) to 1 (dark red). The interface of the Taylor bubble (black line) at f = 0.5.

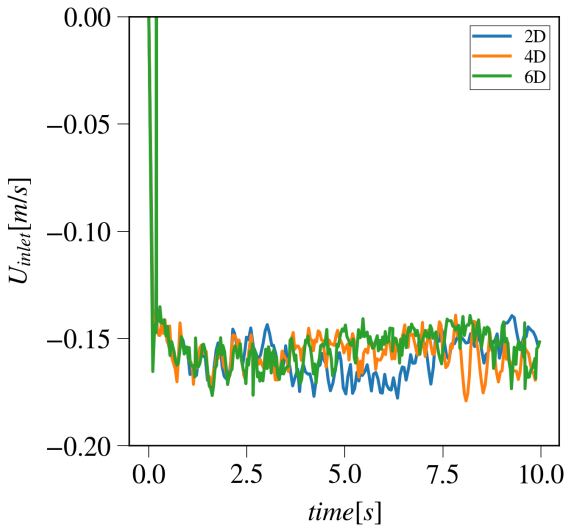

Figure 5.9: Value of adapted streamwise velocity at the inlet along time for three simulations with different initial bubble lengths in turbulent counter-current Taylor bubble flow.

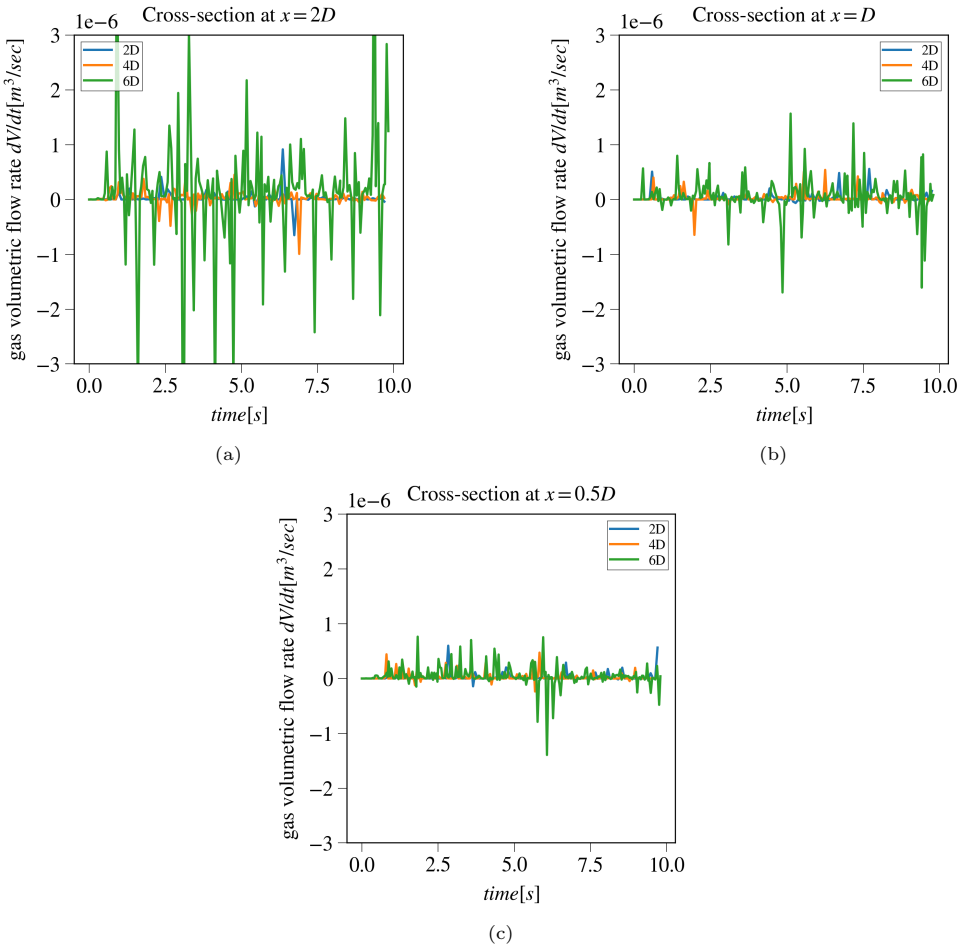

Figure 5.10: Instant gas volumetric flow rates at three different pipe cross-sections downstream the wake along shifted time in turbulent counter-current Taylor bubble flow. Time starts when the first detached bubble is passing from each cross-section for each simulation case.

current Taylor bubble flow, opposite to what has been predicted in the laminar flow in figure 5.6. However, the cumulative ratio of gas that has left the pipe domain after $t = 10s$ for the shortest bubble (i.e. $2D$) is very close to the one of the longest (0.93%) and definitely greater than the ratio bubble of length $4D$ (0.58%). In absolute values, the volume of the detached bubbles that have been transported away with the flow is approximately equal between the shortest and the bubble of moderate length, since the initial bubble volume of the latter, is almost double of the latter.

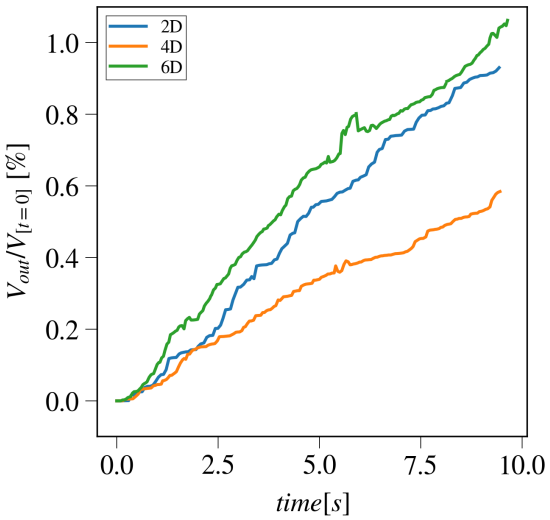

Figure 5.11: Cumulative percentage of the initial bubble volume that has been detached and transported outside the domain by the liquid flow within the $t = 10s$ for different bubble lengths in the turbulent counter-current Taylor bubble flow. Time starts when the first detached bubble is passing from each cross-section for each simulation case.

5.4. Turbulent vs laminar counter-current Taylor bubble flow

After having analyzed how the initial bubble length influences the bubble behavior and its decay rate, the study is extended on how the selection of pipe diameter (and therefore also Eo, Re) affects the bubble decay. Therefore, a direct comparison between the results extracted from laminar (small pipe) in section 5.2 and turbulent counter-current Taylor bubble flow is implemented.

Before starting the comparison, it is better firstly clarifying the relation between the initial Taylor bubble volumes. Due to the bullet shape of the Taylor bubble (cylindrical main part and semi-spherical front nose), the total initial volume is given by:

$$V_{t=0} = \pi r^2 \cdot L_b + \frac{2}{3}\pi r^3 = \pi \left(\frac{D_b}{2}\right)^2 \cdot (x \cdot D) + \frac{2}{3}\pi \left(\frac{D_b}{2}\right)^3 \tag{5.2}$$

,

with L_b the bubble's length which equals with x times the pipe diameter (with x represents the factor 2,4 or 6 for the current setting) and r the radius of the spherical nose which is equal with $r = \frac{D_b}{2}$. Due to the choice of the pipe diameter that has been made for laminar and turbulent case ($\frac{D_{big}}{D_{small}} \sim 2$), the initial bubble volume of small pipe diameter is around one order of magnitude smaller than the initial bubble volume of the big diameter for all the selected choices of bubble length, and in particular, $\frac{V^{big}_{[t=0]}}{V^{small}_{t=0}} \sim 9$.

The comparison of the resulting bubble decay between small and big pipe (or equivalently, between laminar and turbulent flow) starts with figure 5.12 which shows the ratio of the initial gas volume that has been transported outside the pipe domain of $L = 16D$ by the liquid flow for both small (small) and big (turbulent) pipe along (non-shifted) time. Each sub-figure of 5.12 indicates a different bubble length. As already mentioned before, the pipe diameter is smaller (half) for the laminar case and thus, the distance between the tail of the bubble and the outlet is smaller (half) but so does the axial liquid

velocity and therefore, no time-shift is applied at this case. Although the initial Taylor bubble volume in the turbulent case is nine times more than in the laminar flow in all simulations, the ratio of the detached bubbles that have been transported with the flow after $t = 10s$ is ranging from three to five times more than the respective ratio in the laminar flow for all cases. This means that the total amount of gas volume that has been carried out away is from 27 to 51 times greater in turbulent than the laminar case. This difference between laminar and turbulent flows can be explained by the fact that the laminar flow is too weak to detach too much volume of the initial bubble. However, to make a more accurate prediction about this, it is essential to check how much gas volume of the detached bubbles is trapped within the wake region of its simulation and compare against the volume of gas that exits the pipe domain.

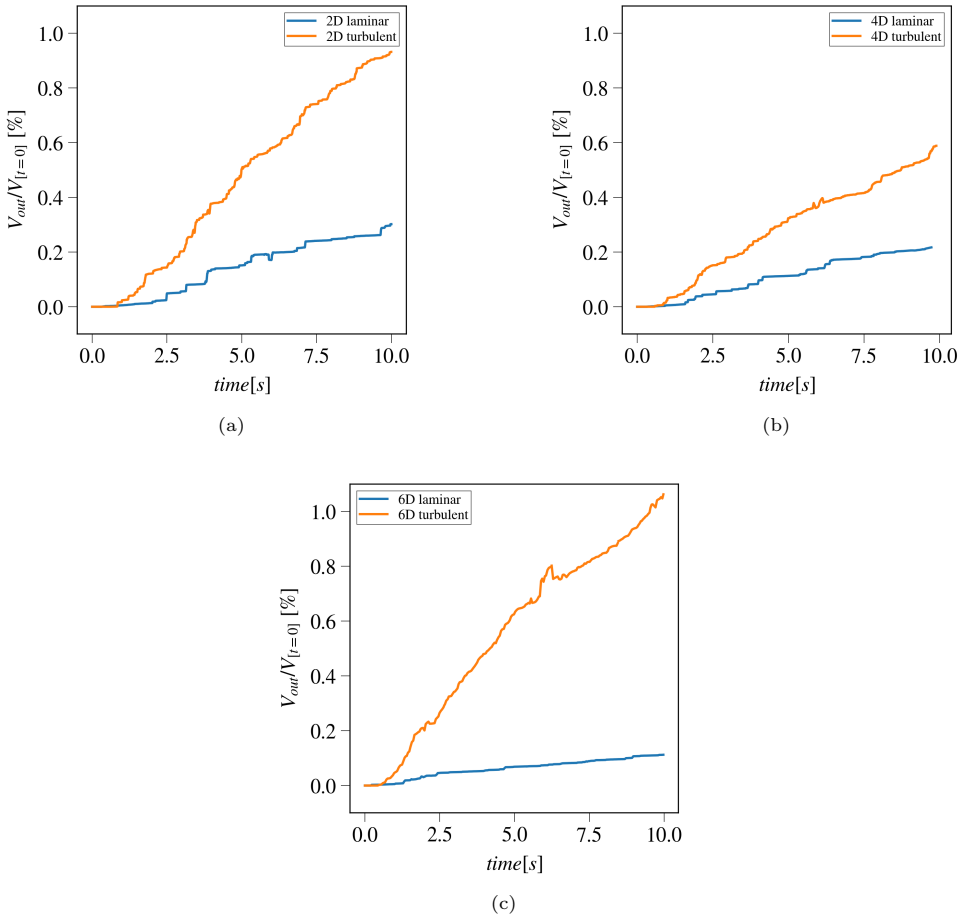

Figure 5.12: Cumulative percentage of the initial bubble volume that has been detached and transported outside the domain by the liquid flow within the $t = 10s$ for different bubble lengths in both turbulent and laminar counter-current Taylor bubble flow.

Figure 5.13 indicates the difference between laminar and turbulent flow both in the volumetric amount of the detached bubbles and also in the volume of "trapped" gas within the wake. It consists of three cross-section views of time (for an interval of $t = 10s$) and space (in the circumferential and radial directions) averaging of void fraction along the scaled (by the value of the pipe diameter in each case) pipe axis for small (laminar flow) and big pipe (turbulent) diameter. There are three sub-figures, one for each initial bubble length ($2D$, $4D$, $6D$) so the initial ratio of the mean void fraction in each pipe cross-section is the same for both simulations indicated in each sub-figure. The laminar flow results in less detached bubbles since not only 27 times less gas is leaving the domain as already indicated in figure 5.12 but also less gas is trapped in the wake behind the bubble for all simulation cases.

To approximate the difference in the loss of void between the two flows quantitatively and estimate the ratio of the detached bubbles that finally exits the pipe domain within $t = 10s$ for each bubble length,

an assumption came from the deployment of figures 5.3 and 5.8 has been made. These figures illustrated that after the average (in time and space) curvature of the tail is flat shaped and perpendicular to the direction of gravity. Therefore, every cell center that lies on the tail interface, has been shifted by the same distance due to the loss of void. Therefore, it is enough to compute the mean shifted distance of the tails point that lies on the pipe axis and then expand it to all points belong to the surface of the tail interface. With this approach, the volumetric bubble decay can be accurately approximated by including all the detached small bubbles that have been merged back to the bubble. The shifted distance is calculated lower for the cases of laminar flow and equals with $0.075D$, 0.3 and 0.59 for bubble's initial length $2D$, $4D$ and $6D$ respectively which corresponds to the ratio of loss of void over initial bubble diameter equal with 0.033, 0.07 and 0.093 according to the following formula:

$$\Delta V = \pi r^2 \cdot H \tag{5.3}$$

, where H is the averaged (in time for $t = 10s$ and space in both circumferential and radial direction) shifted distance of all points that lie on the flat interface of the bubble's tail of radius r.

Similarly, for turbulent flow, the shifted distances are greater and in particular, they are measured $0.11D$, $0.425D$ and $0.6D$ which corresponds to a volumetric loss of void equal with 0.049, 0.099 and 0.095 times the initial bubble volume $V_{[t=0]}$ for bubble's initial length $2D$, $4D$ and $6D$ respectively. Therefore, it seems that the volumetric loss of void is comparable between the laminar and turbulent flow when expressed as a ratio over initial bubble volume. Moreover, it seems that the ratio of loss of void over initial bubble volume is increasing with increasing bubble length except for the transient from $4D$ to $6D$ in the turbulent counter-current Taylor bubble flow.

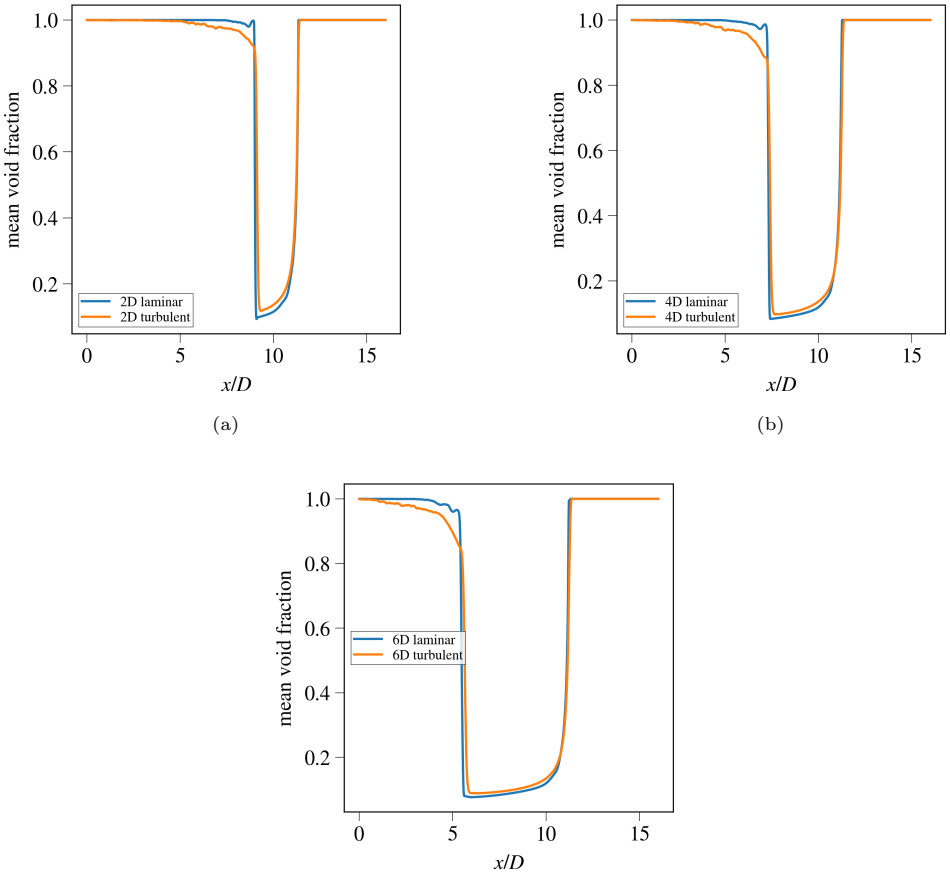

Figure 5.13: Cross-section views of the time and space averaging of void fraction along the pipe axis for the three different bubble lengths (5.13a for $2D$, 5.13b for $4D$, 5.13c for $6D$) in both laminar and turbulent counter-current Taylor bubble flow.

To sum up, table 5.2 summarizes the most important data of the simulations performed in both laminar (section 5.2) and turbulent counter-current Taylor bubble flow. In particular, the table indicates the initial bubble length, the bubble diameter, the ratio of volumetric bubble decay over initial bubble volume, the mesh size, Re number, the mean value of adapted inlet velocity, the wake length, the total wall-clock time, the ratio of volumetric bubble decay over the initial bubble volume, the ratio of the total volume of gas left pipe domain of $L = 16D$ in $t = 10s$ over initial bubble volume and the ratio of total volume of gas left pipe domain over the total loss of void. The degrees of freedom are equal with the amount of cells for a cell-centered approach (cells= DOF) and each simulation has used 64 cores. The most interesting values of this figure are the three last columns indicating the relation between initial bubble volume, total loss of void and total volume of gas that left the pipe domain. The loss of void in the case of laminar flow is one order of magnitude less (in absolute values) than the loss of void in the turbulent flow which is expected since Eo is around four times smaller in the laminar flow. However, when taking account of the initial bubble volumes, the ratio between the two flows is comparable. Regarding the ratio of the volume of the detached bubbles that have left the pipe domain over the total loss of void after $t = 10s$, it remains small for both flows and ranges from 1.2% to 8.8% (depending on initial bubble length) for weaker laminar flow and from 6% to 18.8% for the strongest turbulent flow.

Table 5.2: Simulation data for the laminar and turbulent counter-current Taylor bubble flow: Initial bubble length, bubble diameter, initial gas volume, mesh size, Re number, the mean value of adapted inlet velocity, wake length, total wall-clock time, the ratio of volumetric bubble decay over initial bubble volume, the ratio of the total volume of gas left pipe domain over initial bubble volume, and the ratio of the volumetric gas that left the domain over the total volumetric loss of void.

L_b	$D[m]$	$V_{[t=0]}[m^3]$	h	Re	$\bar{u}_{inlet}[m/s]$	L_{wake}	$t_{wall}[d]$	$1-\frac{V_{[t=10]}}{V_{[t=0]}}$	$\frac{V_{out}}{V_{[t=0]}}$	$\frac{V_{out}}{V_{[t=10]}}$
$2D$	0.0124	$2.5E-06$	$16D/2^{10}$	1400	0.085	$1D$	8	0.03	0.0029	0.088
$4D$	0.0124	$4.7E-06$	$16D/2^{10}$	1400	0.085	$1D$	11	0.07	0.0022	0.032
$6D$	0.0124	$6.9E-06$	$16D/2^{10}$	1400	0.085	$1D$	16	0.09	0.0011	0.012
$2D$	0.026	$2.3E-05$	$16D/2^{10}$	5200	0.16	$1.5D$	8	0.049	0.0093	0.188
$4D$	0.026	$4.2E-05$	$16D/2^{10}$	5200	0.16	$1.5D$	11	0.099	0.0058	0.059
$6D$	0.026	$6.2E-05$	$16D/2^{10}$	5200	0.16	$1.5D$	14	0.097	0.0106	0.11

6

Conclusions

The current work demonstrates a systematic approach towards DNS of turbulent co-current and counter-current Taylor bubble flow and comprises a continuation of the work of [1, OpenFOAM]. The developed code was written in Basilisk open-source software using an "octree" grid approach which allows for adaptive local grid refinement. Basilisk has been validated for three different two-phase flow regimes against published literature.

Firstly, predictions from Basilisk were compared for a two-dimensional bubble rising in a liquid column against three independent studies presented in [2] for two different configurations. The rising bubble simulations in Basilisk showed that the bubble's position, shape, and rise velocity were in excellent agreement with [2] and at much less computational cost due to the local adaptive refinement strategy. Then, the same simulations were executed in OpenFOAM, and the results illustrated that Basilisk captures the gas-liquid interface both much sharper due to its accurate solution of advection equation and in less time even for uniform meshes.

Next, simulations in the laminar Taylor bubble flow rising in a stagnant liquid were carried out in Basilisk for three different configurations as presented in [4]. In the first place, these simulations were implemented using a two-dimensional axial symmetry of the pipe since, in the laminar flow regime, the changes in the circumferential direction can be considered negligible. The predictions of Basilisk for all configurations were in favor of all reference studies ([4, ANSYS], [1, OpenFOAM], [70], [69]). Then, the same simulations were performed in three-dimensions in Basilisk as well where it was observed that using the standard N.S. solver in Basilisk with explicit damping of velocity at the pipe wall does not give the expected solution. For this reason, the direct volume penalization method was implemented implicitly within a modified Basilisk N.S. solver instead which produced results of excellent accuracy.

The conclusions from the above validation cases paved the way towards the main target of the current work: High-fidelity simulations of fully turbulent co-current Taylor bubble flow in Basilisk. Due to the limited computational resources and the inability of stretched mesh in two-phase flows, simulations were carried out with three computational meshes with cell sizes ranging from 16 to 4 wall units according to the experimental setting described in [3]. Although these meshes are too coarse for DNS quality, they assist in providing further insight into the performance of the developed Basilisk solver at a reasonable computational cost. The same simulation strategy with [1, OpenFOAM] was followed allowing for a direct comparison of the results. It was observed that the loss of void of the Taylor bubble in Basilisk was much smaller than what was predicted by OpenFOAM due to the sharper capturing of gas-liquid interface. This increased the allowable averaging time while decreasing the number of simulations in the ensemble. In general, the results of Basilisk for mean streamwise and radial velocity and velocity fluctuations are in qualitative agreement with [1, OpenFOAM] while both software shows significant deviation from the experimental findings of [3] in the velocity fluctuations.

After the successful validation of simulations in the co-current Taylor bubble flow, the work was extended beyond its initial scope by simulating laminar and turbulent counter-current Taylor bubble flow by using the same simulation strategy. The flow parameters of the experiment of [5] were used and simulations were performed in Basilisk for small (laminar flow) and big (turbulent flow) values of pipe diameter and for three different initial bubble lengths. The analysis was focused on how the bubble decay rate is affected by the selection of pipe diameter and initial bubble length, keeping all the

rest parameters the same. Except having calculated the total loss of void, measurements of how much gas exited the domain or remained in the wake were also performed. The results showed that longer bubbles lead to greater in absolute values bubble decay volumetric rates whereas most of the detached bubbles are trapped within the wake and are not transported away with the liquid flow for both laminar and turbulent counter-current flows. Regarding the selection of the value of the pipe diameter (and therefore the type of the flow), simulations in turbulent counter-current Taylor bubble flows resulted in about $27 - 51$ times more detached gas volume in absolute values for the same choice of initial bubble length. Furthermore, in all simulation cases, the total rate of loss of void was not constant along time. It was observed that the loss of void is greater during the first simulation second and after that, the bubble decay rate becomes almost equal to the bubble merging rate, i.e. the rate of the volume of the detached bubbles which are merging back to the Taylor bubble is only slightly smaller than the rate of loss of void.

To sum up, the current work illustrates a proof of concept of simulating turbulent co/counter-current Taylor bubble flow at affordable computational cost and with good numerical accuracy. With additional computational resources available or/and with the implementation of a stretched mesh in two-phase flows, this work should pave the way towards DNS of turbulent co-current Taylor bubble flow. The simulation data from both co-current and counter-current turbulent Taylor bubble flows can be proven useful for the development of low-order turbulence models or/and the validation of more general two-phase modeling strategies.

Bibliography

[1] E.M.A. Frederix, E.M.J. Komen, I. Tiselj, and B. Mikuz. LES of turbulent co-current taylor bubble ow. 2020.

[2] S. Hysing, Stefan Turek, Dmitri Kuzmin, Nicola Parolini, Erik Burman, Sashikumaar Ganesan, and Lutz Tobiska. Quantitative benchmark computations of twodimensional bubble dynamics. International Journal for Numerical Methods in Fluids, 60:1259 – 1288, 08 2009.

[3] L. Shemer, A. Gulitski, and D. Barnea. On the turbulent structure in the wake of taylor bubbles rising in vertical pipes. 19(3):035108, 2007-03.

[4] J.D.P. Araújo, J.M. Miranda, A.M.F.R. Pinto, and J.B.L.M. Campos. Wide-ranging survey on the laminar flow of individual taylor bubbles rising through stagnant newtonian liquids. 43:131–148, 2012-07.

[5] B. Mikuz, J. Kamnikar, J. Prosek and I. Tiselj. Experimental observation of Taylor bubble disintegration in turbulent flow. 28th International Conference Nuclear Energy for New Europe, (Portoro, Slovenia, September 2019).

[6] P. Kundu, I. Cohen, and D. Dowling. Fluid mechanics. Elsevier/AP, sixth edition edition, 2016.

[7] P Wesseling. Principles of Computational Fluid Dynamics. Springer Series in Computational Mathematics. Springer-Verlag, 2001.

[8] G. F. Pinder. Numerical methods for solving partial differential equations: a comprehensive introduction for scientists and engineers. John Wiley and Sons, Inc, 2018.

[9] S. Yoon and D. Kwak. Implicit methods for the navier-stokes equations. Computing Systems in Engineering, 1(2):535–547, 1990-01.

[10] J. Tu, G.H. Yeoh, and C. Liu. Computational Fluid Dynamics. Elsevier, third edition, 2019.

[11] Single-phase vs multi-phase fluid flow. https://www.nuclear-power.net/nuclear-engineering/fluid-dynamics/flow-regime/.

[12] C. E. Brennen. Fundamentals of multiphase flow. Cambridge University Press, 2005.

[13] C. T. Crowe. Multiphase Flow Handbook. CRC Press, 2005.

[14] Y. Zhang A. Faghri. Multiphase systems and phase changes. https://www.thermalfluidscentral.org/e-resources/download.php?id=72.

[15] S. Solmaz. Multiphase flow in cfd: Basics and modeling. https://www.simscale.com/blog/2017/12/multiphase-flow/.

[16] A. Bakker. Applied computational fluid dynamics. https://www.bakker.org/dartmouth06/engs150/.

[17] G.T Oud. A dual interface method in cylindrical coordinates for two-phase pipe flows. 2017. OCLC: 7792811336.

[18] C. W. Hirt and B. Nichols. Volume of fluid (vof) method for the dynamics of free. 1981.

[19] M. Kataja. Multiphase flows in process industry: ProMoni. VTT, 2005. OCLC: 500207414.

[20] A.O. Morgado, J.M. Miranda, J.D.P. Araújo, and J.B.L.M. Campos. Review on vertical gasliquid slug flow. 85:348–368, 2016-10.

[21] J. Fabre and A. Line. Modeling of two-phase slug flow. 24(1):21–46, 1992-01.

[22] J. Thaker and J. Banerjee. Characterization of two-phase slug flow sub-regimes using flow visualization. 135:561–576, 2015-11-01.

[23] X. Lu and A. Prosperetti. A numerical study of taylor bubbles. 48(1):242–252, 2009-01-07.

[24] E.Z. Massoud, Q. Xiao, H.A. El-Gamal, and M.A. Teamah. Numerical study of an individual taylor bubble rising through stagnant liquids under laminar flow regime. 162:117–137, 2018-08.

[25] S. Quan. Co-current flow effects on a rising taylor bubble. 37(8):888–897, 2011-10.

[26] J. D. Bugg, K. Mack, and K. S. Rezkallah. A numerical model of taylor bubbles rising through stagnant liquids in vertical tubes. 24(2):271–281, 1998-03-01.

[27] T. Taha and Z.F. Cui. CFD modelling of slug flow in vertical tubes. 61(2):676–687, 2006-01.

[28] J.D. Bugg and G.A. Saad. The velocity field around a taylor bubble rising in a stagnant viscous fluid: numerical and experimental results. 28(5):791–803, 2002-05.

[29] G. Keshavarzi, G. H. Yeoh, and T. Barber. Comparison of the VOF and CLSVOF methods in interface capturing of a rising bubble. 5(1):43–55, 2013-03.

[30] M. L. Talley, M. D. Zimmer, and I. A. Bolotnov. Coalescence prevention algorithm for level set method. 139(8):081301, 2017-08-01.

[31] E. Gutiérrez, N. Balcázar, E. Bartrons, and J. Rigola. Numerical study of taylor bubbles rising in a stagnant liquid using a level-set/moving-mesh method. 164:158–177, 2017-06.

[32] F. Behafarid, K.E. Jansen, and M.Z. Podowski. A study on large bubble motion and liquid film in vertical pipes and inclined narrow channels. 75:288–299, 2015-10.

[33] N. Balcázar, L. Jofre, Oriol Lehmkuhl, J. Castro, and J. Rigola. A finite-volume/level-set method for simulating two-phase flows on unstructured grids. 64:55–72, 2014-09.

[34] M. Sussman, E. Fatemi, P. Smereka, and S. Osher. An improved level set method for incompressible two-phase flows. 27(5):663–680, 1998-06-01.

[35] Level set method for multiphase flow. `https://www.simscale.com/docs/content/simwiki/numerics/what-is-the-transport-equation.html#multiphase-flow`.

[36] S. Mimouni, R. Denèfle, and S. Fleau, S.and Vincent. Multifield approach and interface locating method for two-phase flows in nuclear power plant. In Philippe Gourbesville, Jean A. Cunge, and Guy Caignaert, editors, Advances in Hydroinformatics, pages 483–500. Springer Singapore, 2016.

[37] N. Balcázar, O. Lehmkuhl, Lluís Jofre, and A. Oliva. Level-set simulations of buoyancy-driven motion of single and multiple bubbles. 56:91–107, 2015-12.

[38] H. Shaban and S. Tavoularis. Detached eddy simulations of rising taylor bubbles. 107:289–300, 2018-10.

[39] M.C.F. Silva, J.B.L.M. Campos, and J.D.P. Araújo. Mass transfer from a soluble taylor bubble to the surrounding flowing liquid in a vertical macro tube a numerical approach. 144:47–62, 2019-04.

[40] Transport equation. `https://www.simscale.com/docs/content/simwiki/numerics/what-is-the-transport-equation.html`.

[41] W. F. Noh and P. Woodward. SLIC (simple line interface calculation). In Adriaan I. van de Vooren and Pieter J. Zandbergen, editors, Proceedings of the Fifth International Conference on Numerical Methods in Fluid Dynamics June 28 July 2, 1976 Twente University, Enschede, Lecture Notes in Physics, pages 330–340. Springer, 1976.

[42] R. Scardovelli and S. Zaleski. Direct numerical simulation of free surface and interfacial flow. 31(1):567–603, 1999-01.

[43] D. Youngs. Time-dependent multi-material flow with large fluid distortion. In Num. Method Fluid Dyn., volume 24, pages 273–285. 1982-01-01.

[44] A. Pathak and M. Raessi. A three-dimensional volume-of-fluid method for reconstructing and advecting three-material interfaces forming contact lines. 307:550–573, 2016-02-15.

[45] T. Boeck, J. Li, E. López-Pagés, P. Yecko, and S. Zaleski. Ligament formation in sheared liquidgas layers. 21(1):59–76, 2006-12-01.

[46] P. Cifani, W.R. Michalek, G.J.M. Priems, J.G.M. Kuerten, C.W.M. van der Geld, and B.J. Geurts. A comparison between the surface compression method and an interface reconstruction method for the VOF approach. 136:421–435, 2016-09.

[47] O. Ubbink and R.I. Issa. A method for capturing sharp fluid interfaces on arbitrary meshes. 153(1):26–50, 1999-07.

[48] D.L. Sun and W.Q. Tao. A coupled volume-of-fluid and level set (VOSET) method for computing incompressible two-phase flows. 53(4):645–655, 2010-01.

[49] X. Yang, A. J. James, J. Lowengrub, X. Zheng, and V. Cristini. An adaptive coupled level-set/volume-of-fluid interface capturing method for unstructured triangular grids. 217(2):364–394, 2006-09.

[50] N. Balcázar, O. Lehmkuhl, L. Jofre, J. Rigola, and A. Oliva. A coupled volume-of-fluid/level-set method for simulation of two-phase flows on unstructured meshes. 124:12–29, 2016-01.

[51] S. P. van der Pijl, A. Segal, C. Vuik, and P. Wesseling. A mass-conserving level-set method for modelling of multi-phase flows. 47(4):339–361, 2005-02-10.

[52] Ansys Fluent ver. 14.0 2011 Theory guide. Canonsburg, USA: Ansys Inc.

[53] M. Dang, J. Yue, and G. Chen. Numerical simulation of taylor bubble formation in a microchannel with a converging shape mixing junction. Chemical Engineering Journal, 262:616 – 627, 2015.

[54] B. A. Nichita, I. Zun, and J. Thome. A level set method coupled with a volume of fluid method for modeling of gas-liquid interface in bubbly flow. Journal of Fluids Engineering, 132, 08 2010.

[55] A. Igaadi, R. E. Amraoui, and H. E. Mghari. Simulation of bubble dynamic behavior in subcooled flow boiling9 application to energy systems design. In 2018 6th International Renewable and Sustainable Energy Conference (IRSEC), pages 1–6, Dec 2018.

[56] J. Hua and D. Mortensen. A front tracking method for simulation of two-phase interfacial flows on adaptive unstructured meshes for complex geometries. International Journal of Multiphase Flow, 119:166 – 179, 2019.

[57] Learncax. `learncax.com/class/multiphase-flow-modeling-using-ansys-fluent-detail`.

[58] Ansys-approaches to multiphase modeling. `https://www.afs.enea.it/project/neptunius/docs/fluent/html/th/node293.htm`.

[59] J. B. L. M. Campos and J. R. F. Guedes De Carvalho. An experimental study of the wake of gas slugs rising in liquids. 196:27–37, 1988-11.

[60] Pardo R. Yánez R. Trallero J.L. Joseph D.D. Viana, F. Universal correlation for the rise velocity of long gas bubbles in round pipes. Journal of Fluid Mechanics, 494:379 – 398, 11 2003.

[61] V. K. Prasad, D. Chatterjee, and S. P. Singh. Numerical simulation of gas-bubble formation through two submerged orifices. Sādhanā, 43(11):171, Sep 2018.

[62] H. Tsuge, Y. Tanaka, K. Terasaka, and Hirokazu Matsue. Bubble formation in flowing liquid under reduced gravity. Chemical Engineering Science, 52(21):3671 – 3676, 1997.

[63] M. T. Sena Esteves and J. R. F. Guedes De Carvalho. Liquid-side mass transfer coefficient for gas slugs rising in liquids. 48(20):3497–3506, 1993-10-01.

[64] G. Montoya and E. Baglietto. Resolved interface of taylor bubble simulations to support eulerian multiphase closures derivation. page 13.

[65] OpenCFD. OpenFOAM - Official home of The Open Source Computational Fluid Dynamics (CFD) Toolbox. http://www.openfoam.com, (2019-09-25).

[66] WIPO global brand database. https://www3.wipo.int/branddb/en/index.jsp?q={%22searches%22:%5b{%22te%22:%22openfoam%22,%22fi%22:%22BRAND%22}%5d},(2019-10-01).

[67] R. van Hout, A. Gulitski, D. Barnea, and L. Shemer. Experimental investigation of the velocity field induced by a taylor bubble rising in stagnant water. 28(4):579–596, 2002-04-01.

[68] J. L. G. Oliveira, C. W. M. van der Geld, and J. G. M. Kuerten. Lagrangian and eulerian statistics of pipe flows measured with 3d-PTV at moderate and high reynolds numbers. 91(1):105–137, 2013-07.

[69] S. Nogueira, M.L. Riethmuler, J.B.L.M. Campos, and A.M.F.R. Pinto. Flow in the nose region and annular film around a taylor bubble rising through vertical columns of stagnant and flowing newtonian liquids. 61(2):845–857, 2006-01.

[70] S. Nogueira, M.L. Riethmuller, J.B.L.M. Campos, and A.M.F.R. Pinto. Flow patterns in the wake of a taylor bubble rising through vertical columns of stagnant and flowing newtonian liquids: An experimental study. 61(22):7199–7212, 2006-11.

[71] I. A. Bolotnov, K. E. Jansen, D. A. Drew, A. A. Oberai, R. T. Lahey, and M. Z. Podowski. Detached direct numerical simulations of turbulent two-phase bubbly channel flow. 37(6):647–659, 2011-07.

[72] S. Nagrath, K. E. Jansen, and R. T. Lahey. Computation of incompressible bubble dynamics with a stabilized finite element level set method. 194(42):4565–4587, 2005-10.

[73] A. Carlson, P. Kudinov, and C. Narayanan. Prediction of two-phase flow in small tubes: A systematic comparison of state-of-the-art cmfd codes. 01 2008.

[74] Ascomp: Transat cfd suite. http://ascomp.ch/products/transat-suite/.

[75] R. Rzehak and S. Kriebitzsch. Multiphase CFD-simulation of bubbly pipe flow: A code comparison. International Journal of Multiphase Flow, 68:135–152, 2015-01.

[76] V.H. Bhusare, M.K. Dhiman, D.V. Kalaga, S. Roy, and J.B. Joshi. CFD simulations of a bubble column with and without internals by using OpenFOAM. Chemical Engineering Journal, 317:157–174, 2017.

[77] S. Khodaparast, M. Magnini, N. Borhani, and J. R. Thome. Dynamics of isolated confined air bubbles in liquid flows through circular microchannels: an experimental and numerical study. Microfluidics and Nanofluidics, 19(1):209–234, July 2015.

[78] D. T. Dumitrescu. Strömung an einer luftblase im senkrechten rohr. 23(3):139–149, 1943.

[79] R. M. Davies and G. I. Taylor. The mechanics of large bubbles rising through extended liquids and through liquids in tubes. Proceedings of the Royal Society of London. Series A. Mathematical and Physical Sciences, 200(1062):375–390, 1950.

[80] K. H. Bendiksen. On the motion of long bubbles in vertical tubes. 11(6):797–812, 1985-11.

[81] S. Benattalah, F. Aloui, and M. Souhar. Experimental analysis on the counter-current dumitrescu-taylor bubble flow in a smooth vertical conduct of small diameter. 4(4):14.

[82] N.V. Ndinisa, D.E. Wiley, and D.F. Fletcher. Computational fluid dynamics simulations of taylor bubbles in tubular membranes. 83(1):40–49, 2005-01.

[83] Alan A., B. B. Author, and C. Author. Title of article. Title of Journal, 10(2):49–53, 2005.

[84] J. Hua, J. F. Stene, and P. Lin. Numerical simulation of 3d bubbles rising in viscous liquids using a front tracking method. 227(6):3358 – 3382, 2008.

[85] A. Tomiyama, Y. Nakahara, Y. Adachi, and S. Hosokowa. Shapes and rising velocities of single bubbles rising through an inner subchannel. 40(3):136–142, 2003.

[86] E.T. White and R.H. Beardmore. The velocity of rise of single cylindrical air bubbles through liquids contained in vertical tubes. 17(5):351–361, 1962.

[87] Y. Morinishi, O. V. Vasilyev, and T. Ogi. Fully conservative finite difference scheme in cylindrical coordinates for incompressible flow simulations. J. Comput. Phys., 197(2):686710, July 2004.

[88] C.C. Maneri and N. Zuber. An experimental study of plane bubbles rising at inclination. 1(5):623–645, 1974-11.

[89] K. Niranjan, M. A. Hashim, A. B. Pandit, and J. F. Davidson. Liquid-phase controlled mass transfer from a gas slug. 43(6):1247–1252, 1988-01-01.

[90] W. Chen, M. Twu, and Chunhui Pan. Liquid two-phase flow in micro-channels. International Journal of Multiphase Flow - INT J MULTIPHASE FLOW, 28:1235–1247, 07 2002.

[91] Basilisk. `http://basilisk.fr/`.

[92] Y. Miyake T. Miyauchi N. Kasagi, K. Horiuti and Y. Nagano. Establishment of the Direct Numerical Simulation Data Bases of Turbulent Transport Phenomena. 1993.

[93] E.M.A. Frederix, E. Komen, I. Tiselj, and B. Miku. Les of turbulent co-current taylor bubble flow. Flow, Turbulence and Combustion, 03 2020.

[94] Gerris. `http://gfs.sourceforge.net/wiki/index.php/Main_Page`.

[95] The tree grid structure in basilisk. `http://basilisk.fr/sandbox/Antoonvh/The_Tree_Grid_Structure_in_Basilsik`.

[96] Gabriel Weymouth and Dick Yue. Conservative volume-of-fluid method for free-surface simulations on cartesian-grids. J. Comput. Physics, 229:2853–2865, 04 2010.

[97] J.M. López-Herrera, A.M. Gañán-Calvo, S. Popinet, and M.A. Herrada. Electrokinetic effects in the breakup of electrified jets: A volume-of-fluid numerical study. International Journal of Multiphase Flow, 71:14 – 22, 2015.

[98] Basilisk interface reconstruction from volume fractions. `http://basilisk.fr/src/geometry.h#rectangle_fraction`.

[99] Basilisk geometry of rectangle fraction. `http://basilisk.fr/src/geometry.h#rectangle_fraction`.

[100] Basilisk vof. `http://basilisk.fr/src/vof.h`.

[101] Rajat Mittal and Gianluca Iaccarino. Immersed boundary methods. Annual Review of Fluid Mechanics, 37(1):239–261, 2005.

[102] E.M.J. Komen, E.M.A. Frederix, T.H.J. Coppen, V. DAlessandro, and J.G.M. Kuerten. Analysis of the numerical dissipation rate of different rungekutta and velocity interpolation methods in an unstructured collocated finite volume method in openfoamő. Computer Physics Communications, 253:107145, 2020.

[103] John B Bell, Phillip Colella, and Harland M Glaz. A second-order projection method for the incompressible navier-stokes equations. Journal of Computational Physics, 85(2):257 – 283, 1989.

[104] Featflow. http://www.featflow.de/en/benchmarks/cfdbenchmarking/bubble/bubble_reference.html.

[105] R. Clift, J.R. Grace, and M.E. Weber. Bubbles, Drops and Particles. Academic Press/AP, 1978.

[106] Basilisk surface tension. http://basilisk.fr/src/tension.h.

[107] Basilisk curvature. http://basilisk.fr/src/curvature.h#curvature.

[108] R. Brown. The mechanics of large gas bubbles in tubes /. Can. J. Chem. Eng., 43, 01 1965.

[109] G.B. Wallis. One-dimensional two-phase flow. 1969.

[110] S.B Pope. Turbulent flows. 2000.

[111] R. J. LeVeque. High-Resolution Methods, page 100128. Cambridge Texts in Applied Mathematics. Cambridge University Press, 2002.

[112] U. M. Ascher, S. J. Ruuth, and R. J. Spiteri. Implicit-explicit runge-kutta methods for time-dependent partial differential equations. Applied Numerical Mathematics, 25(2):151 – 167, 1997. Special Issue on Time Integration.